Atomic Shell Structure in a Ring Polymer Formulation of Orbital-Free Density Functional Theory

by

Phil LeMaitre

A thesis
presented to the University of Waterloo
in fulfillment of the
thesis requirement for the degree of
Master of Science
in
Physics

Waterloo, Ontario, Canada, 2022

Author's Declaration

I hereby declare that I am the sole author of this thesis. This is a true copy of the thesis, including any required final revisions, as accepted by my examiners.

I understand that my thesis may be made electronically available to the public.

Abstract

An alternative approach to orbital-free density functional theory based on self-consistent field theory for ring polymers is proposed and applied to isolated atoms on the periodic table in their ground-state. Using a spherical-averaging approximation that groups electrons into periodic table rows, quantitatively accurate atomic binding energies and electronic density profiles are predicted for the first 86 elements as compared to the Hartree-Fock model. The agreement with the binding energies predicted by Hartree-Fock theory is within 10% for the first 86 elements, and within 3% for the first 34 elements. The comparison of electronic density profiles with Hartree-Fock theory for the first 36 elements highlights the shortcomings of the approximation to the Pauli-exclusion field (used to enforce the Pauli-exclusion principle) used in this work in the form of larger than normal peak-to-peak separation, revealing some characteristics that the exact Pauli-exclusion field should have. The density profiles, especially helium and lithium, also provide some legitimacy for the novel electron self-interaction correction introduced in this work. The emergence of atomic shell structure from the postulated pair structure of the model and the spontaneous emergence of spherical symmetry-breaking are also predicted by the model. However, due to the approximation made on the Pauli-exclusion field, the predicted shell structure starts to deviate significantly past the element neon and the symmetry-breaking is predicted to occur at carbon instead of boron. The symmetry-breaking effect is also found to have minimal impact on the binding energies, which suggests that the spherical-averaging approximation is physically reasonable when investigating bulk properties of atomic systems. The pair density contour plots display behaviour similar to polymer macro-phase separation, but still produce the same total electronic density profile that is predicted by quantum mechanics. As well, the framework for general non-orthogonal basis sets within the model is derived and the specific implementation of Gaussian basis sets demonstrate better resolution with significantly less numbers of basis functions than previous iterations; they also do not suffer from finite-size effects. The Gaussians do however introduce an auxiliary problem of choosing the proper basis set exponents to span the space, which can prevent convergence to the infinite basis set limit. Finally, some future extensions for the model are discussed, where the implementation of these extensions is detailed and brief commentary on their implications is given.

Acknowledgements

I am indebted to so many wonderful individuals for stimulating both my intellectual and personal growth, and for guiding me through my research journey. First and foremost, I have to thank my supervisor Dr. Russell Thompson for giving me the opportunity to conduct research with them and for always taking the time to help me through any problems I came to them with. I also really enjoyed our conversations on the foundations of quantum mechanics.

I want to also thank my advisory committee members Dr. Mark Matsen and Dr. Jeff Chen for critically evaluating my research progress and potential, as well as asking interesting questions that allowed me to dig deeper into certain topics.

Last but certainly not least, I want to acknowledge all the love and continuous support I received from my friends, my family, and especially from my partner Sarah Kimber; I couldn't have made it through my master's degree without them. I look back with particular fondness at the philosophical conversations between my friends and I at the pub, which have been enormously valuable in expanding my world-view and developing my intuition; I think I have also become a better person for them. Equally as important to me, are the many adventures and laughs I have shared with Sarah.

Table of Contents

List of Tables viii

List of Figures ix

1 Introduction 1

1.1 Motivation 1

1.2 Objectives 3

1.3 Overview 3

2 Background 5

2.1 Density Functional Theory 6

2.1.1 Hohenberg-Kohn-Mermin Theorems 7

2.1.2 Kohn-Sham Density Functional Theory 10

2.1.3 Orbital-Free Density Functional Theory 11

2.2 Polymer Self-Consistent Field Theory 13

2.3 The Quantum-Classical Correspondence 15

3 A Polymeric Self-Consistent Field Approach to Quantum Density Functional Theory 17

3.1 Derivation of SCFT Equations 18

3.2 Spectral Method 24

3.3 Potentials and Fields 29

3.3.1 Coulombic Fields 30

3.3.2 Pauli-Exclusion Field 31

3.3.3 Self-Interaction Correction 35

3.4 Free Energy and Spectral SCFT Equations 37

4 Atomic Shell Structure 40

4.1 Computational Methods 41

4.2 Spherically-Averaged Atomic Electron Density 47

4.3 Full Angular Atomic Electron Density 54

4.4 Limitations 74

5 Conclusions and Future Work 76

References 79

APPENDICES 86

A Basis Function-Specific Quantities 87

A.1 Overlap Matrix 88

A.2 Laplace Matrix 89

A.2.1 Laplacian of the Gaussian Basis Functions 90
A.2.2 Components of the Laplace Matrix 90
A.3 Gamma Tensor 91
A.3.1 Integral of Three Real Spherical Harmonics 91

B Path Integral Solution to the Modified Diffusion Equation **94**

List of Tables

4.3 Spherically-Averaged Atomic Binding Energies for H-Rn 50

4.4 Spherically-Averaged Pair Atomic Binding Energies for H-Ne 64

4.5 Full Angular Atomic Binding Energies for H-Ne 64

4.6 Electron Number Density Constraints 73

4.7 Kinetic Energy Density Constraints 74

List of Figures

3.1 Polymer Excluded-Volume Visual 32

4.1 Flowchart of Self-Consistent Algorithm 45

4.2 Krypton Free Energy Convergence with Basis Set Size 46

4.3 Hartree-Fock Percent Deviation Plot 51

4.4 Spherically-Averaged Hydrogen Density Plot 52

4.5 Spherically-Averaged Helium Density Plot 53

4.6 Spherically-Averaged Density Plots for He-C 55

4.7 Spherically-Averaged Density Plots for N-Mg 56

4.8 Spherically-Averaged Density Plots for Al-Ar 57

4.9 Spherically-Averaged Density Plots for K-Cr 58

4.10 Spherically-Averaged Density Plots for Mn-Z 59

4.11 Spherically-Averaged Density Plots for Ga-Kr 60

4.12 Spherically-Averaged Density Plots for Rb-Mo 61

4.13 Spherically-Averaged Density Plots for Tc-Cd 62

4.14 Spherically-Averaged Density Plots for In-Xe 63

4.15 Boron Angular Pair Density Contour Plots for Fixed Values of θ 66

4.16 Carbon Angular Pair Density Contour Plots for Fixed Values of θ 67

4.17 Nitrogen Angular Pair Density Contour Plots for Fixed Values of θ 68

4.18 Oxygen Angular Pair Density Contour Plots for Fixed Values of θ 69

4.19 Fluorine Angular Pair Density Contour Plots for Fixed Values of θ 70

4.20 Neon Angular Pair Density Contour Plots for Fixed Values of θ 71

Chapter 1

Introduction

1.1 Motivation

Two distinctive hallmarks of atomic systems that emerge from the quantum theory are the presence of highly inhomogeneous shell structure and the spontaneous breaking of spherical symmetry, which the Pauli-exclusion principle is partially responsible for. It is these two attributes that play a fundamental role in determining atomic size and facilitating chemical bonding, the latter of which is the wellspring of many biological and chemical processes; the most important example being the formation of molecules. For instance, chemical bonding holds DNA molecules together; it helps to determine the structure of crystal lattices in solid-state materials, proteins, chromosomes, and cell shapes [2]; and it helps determine chemical reaction rates [20]. It is safe to say that an understanding of the mechanism behind the above mentioned characteristics of atomic systems is of crucial import, and that any theory of the atom ought to reproduce these qualities if it is to be taken seriously.

One field that has become particularly prolific in the study of atomic systems with the advent of modern computing, is that of density functional theory (DFT), which is regarded by many scientists as the most robust theoretical framework that captures the properties of atomic systems. DFT translates the problem of solving the Schrödinger equation for the many-body ground-state wavefunction, to the problem of finding the ground-state electron density, which describes the distribution of all the electrons in the atomic system. The work of Hohenberg and Kohn [28] originally proved that the electron density was completely equivalent to the many-body wavefunction, and that the procedure just described is an exact mapping of the problem. In

practice however, the Hohenberg-Kohn theorems are quite opaque on how the electron density should be calculated, and one must resort to approximations if progress is to be made. The most accurate approximation scheme currently in use is called Kohn-Sham DFT (KS-DFT), which breaks up the kinetic energy of the atomic system into an interacting and non-interacting part, and the non-interacting part is then used to solve an eigenvalue problem whose eigenfunctions determine the electron density [41, 61]. The downside to this is that solving the eigenvalue problem for every particle in the system becomes very computationally expensive when the system size becomes large, and the interacting portion of the kinetic energy now has to be approximated. An alternative to KS-DFT is orbital-free DFT (OF-DFT), which deals only with the raw electron density [35]. OF-DFT breaks up the kinetic energy in the same way as KS-DFT, but is formulated so that only one eigenvalue problem needs to be solved, which means OF-DFT is much more computationally tractable for larger systems; the downside being that both the interacting and non-interacting kinetic energies must now be approximated, and the Pauli-exclusion principle added in manually. Due to the scaling of OF-DFT there has been considerable research effort devoted to finding increasingly accurate kinetic energy expressions so that accurate simulations of large atomic systems can be done efficiently [35].

Recently, there has been renewed interest in finding classical representations for quantum theory [63, 7] and in particular, Thompson [78] was able to demonstrate an equivalence between self-consistent field theory (SCFT) for ring polymers and finite temperature DFT using the "quantum-classical isomorphism" developed by references [12, 11, 17]. Thompson's approach has many appealing qualities that will be teased out in the remainder of this thesis and represents a valuable opportunity to develop an alternative approach to OF-DFT that could potentially offer increased computational efficiency, along with improved expressions for the kinetic energy functional. In fact, Thompson's approach has already been shown to reproduce quantitatively accurate properties of small atomic systems [78, 79] and diatomic molecules [72]. However, the computational framework originally used by Thompson was too limiting to probe the characteristic properties of atomic systems mentioned at the beginning of this section. Thus, it is the aim of this work to build a new computational foundation based on non-orthogonal Gaussian basis sets to investigate said properties, and bring Thompson's theory one step closer to being considered as a competitive alternative to perform OF-DFT calculations with. Thompson's approach also has foundational significance to quantum theory, as the classical background where the theory lives represents a unique opportunity to test whether a classical theory can reproduce the predictions of quantum theory, but more specifically, whether the postulates of Thompson's theory lead to equivalent results as those of other interpretations of quantum theory.

1.2 Objectives

The theory presented in this work offers two main advantages over traditional DFTs: 1) the introduction of an extra-dimensional parameter space interpreted through polymer SCFT both allows for, and makes more accessible, the construction of higher accuracy exchange-correlation functionals, since the behaviour of polymer threads provides an intuitive rubric to incorporate interactions into the system (e.g. electron repulsion due to the Pauli-exclusion principle) while the parameter space allows one to explicitly account for them in calculations; and 2) establishes a link with quantum DFT and classical ring polymer SCFT, allowing for the predictions of the model to be approached with classical intuition. The ring polymer architecture also invites the use of spectral methods to significantly reduce the computational burden of solving the governing equations, potentially offering an advantage in computational speed as well.

The primary objective of this thesis is to construct an alternative DFT framework from polymer SCFT that is capable of accurately simulating quantum systems. More specifically, to analyse the characteristics and shell structure of isolated atomic systems in their ground state, and to predict the spontaneous emergence of spherical symmetry-breaking in these systems.

The secondary objectives of the research involve incorporating new Gaussian basis sets into the computational implementation of the model and evaluating their robustness, while at the same time developing the computational framework for non-orthogonal basis sets within the model. We also aim to test the accuracy of a novel electron self-interaction correction introduced to the model with the predictions of Hartree-Fock theory, as we claim that the combination with a previously introduced mechanism to incorporate the Pauli-exclusion principle is equivalent to it.

1.3 Overview

The thesis is divided into five chapters, each of which carefully motivates the succeeding section and establishes the mathematical tools necessary to understand the content of that section. Chapter 2 introduces the ideas used in the model and provides a mathematical and conceptual background. DFT is first introduced in section 2.1, discussing the Hohenberg-Kohn-Mermin theorems that underlie the theory in subsection 2.1.1, then the two main flavours of DFT are presented; those being KS-DFT (subsection 2.1.2) and OF-DFT (subsection 2.1.3). Polymer SCFT is introduced in section 2.2, where the procedure to find the partition function and free energy for a Gaussian distributed chain is sketched out. Lastly in section 2.3, the quantum-classical correspondence is elucidated, providing the bridge between the seemingly disjointed frameworks presented in this

chapter.

Chapter 3 is principally where the theory behind the model used in this work is derived. The actual derivation of the model equations from first principles is initially presented in section 3.1. Section 3.2 then introduces the spectral method for use in the computational implementation of the model and the model equations from section 3.1 are recast into their spectral form. The fields that comprise the model are outlined in section 3.3 along with their spectral forms, where subsection 3.3.1 discusses the Coulombic fields; subsection 3.3.2 discusses the field arising from the Pauli-exclusion principle; and subsection 3.3.3 discusses the electron self-interaction correction. The free energy expression with all fields input is then derived along with its corresponding spectral form in section 3.4, and the SCFT equations are summarized for convenience.

Chapter 4 explores some of the consequences of the model laid out in the previous chapter for single atomic systems, and describes the computer implementation of the model. Section 4.1 begins with a discussion of how the Gaussian basis functions were chosen and then launches into an illustration of the self-consistent algorithm used to solve the model equations, describing all sources of error that may be present as well. The atomic binding energies and density profiles from the spherically-averaged atomic electron densities are next presented in section 4.2, and then the full angular case is presented in section 4.3. Fruitful comparison with Hartree-Fock theory is discussed throughout both sections. Finally, the limitations and some future work is discussed in section 4.4.

Chapter 5 summarizes the results from modelling atomic systems with the current theory and expands the discussion of future directions initiated in section 4.4.

Chapter 2

Background

The theory of probability has been at the forefront of the paradigm shift in how we think about physical theories. A most vivid demonstration of this statement can be extracted from the theory governing the interactions between microscopic entities, otherwise known as statistical physics. In statistical physics, the objective is typically to explain the macroscopic features of a system from knowledge of how its microscopic constituents interact with each other. The modern theory of heat is a remarkably successful example of how interactions between large assemblages of atoms give rise to such notions as temperature or pressure, and can even explain exotic phenomena ranging from turbulence to superconductivity [36].

The physical picture that emerges from statistical physics is encapsulated entirely in the partition function, which is something like a weighted sum of the possible configurations available to the system. The intuition behind the importance of the partition function can be gleaned from its role as a normalizing factor for the probability distribution of the system, meaning that it encodes precisely how the different configurations available to the system would be distributed throughout it (hence the name partition) [36]. This function clearly depends on the nature of the system and its constituents, along with any constraints that may be present. There are three prototypical scenarios that are usually considered by physicists: fixed total energy with entropy S as the thermodynamic potential (the microcanonical ensemble); fixed temperature and energy being exchanged with the environment, and Helmholtz free energy F as the thermodynamic potential (the canonical ensemble); fixed temperature with energy and particles being exchanged with the environment, and the grand potential Ω as the thermodynamic potential (the grand canonical ensemble). Accounts of these scenarios are well documented and can be found in e.g. references [55, 36].

The partition function not only serves as the starting point for the derivation of the theory presented in this thesis, it also acts as a bridge between the quantum and classical realms through the quantum-classical correspondence. It is this latter role of the partition function that connects the ideas and machinery of classical probability theory with that of quantum probability theory, which we exploit extensively to provide an intuition for understanding the objects appearing in the theory. The connection just described is much more vividly illustrated when it arises naturally from the material that it conjoins, thus it is the purpose of this chapter to introduce said material, which will be done as follows. A tour through DFT starting with the Hohenberg-Kohn-Mermin theorems, then on to the Kohn-Sham and orbital-free formulations, starts off this chapter. Following that, a short introduction to polymer SCFT is given, as it will be used in chapter 3 when the derivation of the present theory is given. Lastly, the quantum-classical correspondence is discussed, placing the background material into context and motivating the basic premise of the model.

2.1 Density Functional Theory

It was quickly realized by the founders of quantum mechanics that the evolution equations for the wavefunction were too intractable to produce accurate predictions for large many-body systems. This view was most notably espoused by Dirac, who was quoted to have said [33]

> "The general theory of quantum mechanics is now almost complete, ... The underlying physical laws necessary for the mathematical theory of a large part of physics and the whole of chemistry are thus completely known, and the difficulty is only that the exact application of these laws leads to equations much too complicated to be soluble. It therefore becomes desirable that approximate practical methods of applying quantum mechanics should be developed, which can lead to an explanation of the main features of complex atomic systems without too much computation."

Opinions such as Dirac's led to a flurry of research developing alternative methods and approximation schemes that would allow the probing of the general features of atomic and molecular systems, and eventually large solid-state systems. One of the most successful of these alternative methods for calculating the wave function is called Hartree-Fock theory [74, 33]. Hartree-Fock theory is a "self-consistent" method that determines the wavefunction from the fields experienced by the particles in the system, meaning it starts with some initial guess for the fields and computes new ones that are then used as the next guess until the difference between input and

output falls below some threshold [74, 33]. The updates for the fields are produced from the solution of an eigenvalue equation for each particle in the system, with suitable assumptions, whose eigenfunctions are referred to as orbitals. A Slater determinant is then formed from the final orbitals to enforce the Pauli-exclusion principle, yielding the wave function. Not only does it readily allow particle statistics to be accounted for, Hartree-Fock theory also exactly accounts for particle exchange and self-interaction effects. These appealing aspects made Hartree-Fock theory the most dominant and convenient method for electronic structure calculations for many decades, but there is always a price to pay for convenience: the complete neglect of electronic correlations. Ignoring correlations is acceptable for sufficiently small systems, but as the system size increases suddenly the contribution due to correlations becomes significant and one should look elsewhere if the wavefunction is to be computed accurately [74, 33].

One of the earliest attempts to overcome the wavefunction-based picture of quantum theory was a model developed by Thomas and Fermi [61, 33], which used the electronic density as the basic variable. In the Thomas-Fermi model, the electrons are distributed uniformly throughout all of phase space and interact through an effective potential that is in turn determined by the electron density and nuclear charge. These assumptions lead to an exceptionally simple description of the atom and expression for the kinetic energy, known as the local density approximation [61, 33]. The simplicity of the description, however, failed to predict atomic shell structure or molecular bonding [75]. This result is unsurprising to the modern physicist as it is well-known that electrons in atomic systems have a highly inhomogeneous distribution and they certainly do not fill all of phase space [61, 33]. Nevertheless, the Thomas-Fermi model introduced a new way of thinking about quantum mechanics, and would serve as the forerunner to one of the most successful enterprises in all of physics: DFT.

Density functional theory rigorously develops the ideas of the Thomas-Fermi model into a general framework that puts the electron density on the same footing as the wavefunction. The theory has been massively successful in simulating atomic and molecular systems, as well as large solid-state and even biological systems to within chemical accuracy [33]. The popularity of DFT would not have been possible without the foundation established by the Hohenberg-Kohn-Mermin theorems, which we begin this section with.

2.1.1 Hohenberg-Kohn-Mermin Theorems

Density functional theory as it is known today, was first conceived of in the seminal works of Hohenberg and Kohn [28], where they proved that the electron density $n(\boldsymbol{r})$ was in one-to-one correspondence with the external potential $v(\boldsymbol{r})$ and by virtue of the external potential fixing the

Hamiltonian $\hat{H}$, that the ground state many-body wavefunction Ψ was also unique to a given $n(\boldsymbol{r})$. Shortly after Hohenberg and Kohn, Mermin [56] generalized the result to the finite-temperature setting, which we will attempt to give an account of in this section as it is closer in spirit to the context of the thesis. The paper of Mermin [56] is closely followed in the analysis and it will be assumed for simplicity and clarity, that the ground state configuration is non-degenerate, possesses no spin, and is static; for a more complete treatment including spin, degeneracy, and time-dependence see references [82, 46, 66] respectively.

Suppose we have a system of spinless particles interacting through a Coulomb potential $1/|\boldsymbol{r}|$ and an external potential $v(\boldsymbol{r})$, enclosed in a box that is in contact with a thermal reservoir at temperature T, such that the system can exchange particles and energy with the reservoir (grand canonical ensemble). Let the state of the system be denoted with the density operator $\hat{\rho}$. The Hamiltonian of the system is defined to be

$$\hat{H} = \hat{K} + \hat{V} + \hat{U}\,, \tag{2.1}$$

where $\hat{K}$ corresponds to the kinetic energy operator, $\hat{V}$ to the external potential energy operator associated with $v(\boldsymbol{r})$, and $\hat{U}$ to the Coulomb repulsion energy operator between particles.

The goal is to show that there exists a functional $F[n]$ independent of $v(\boldsymbol{r})$, such that

$$\Omega \equiv \min_{n} \left\{ \int \mathrm{d}\boldsymbol{r}\, v(\boldsymbol{r}) n(\boldsymbol{r}) + F[n] \right\} \tag{2.2}$$

is the grand potential associated with $v(\boldsymbol{r})$ when $n(\boldsymbol{r})$ is the equilibrium density in the presence of $v(\boldsymbol{r})$. To start with, the grand potential functional can be expressed as

$$\Omega[\hat{\rho}] = \mathrm{Tr}\left[\hat{\rho}\left(\hat{H} - \mu\hat{N} + \frac{1}{\beta}\ln(\hat{\rho})\right)\right] \tag{2.3}$$

where $\beta = 1/k_B T$, μ is the chemical potential, $\hat{N}$ is the particle number operator that yields the number of particles N when applied to the state of the system, and the last term corresponds to the entropy. The equilibrium density operator in the grand canonical ensemble is given by the well-known expression

$$\hat{\rho}_0 = \frac{e^{-\beta(\hat{H}-\mu\hat{N})}}{\mathrm{Tr}(e^{-\beta(\hat{H}-\mu\hat{N})})}\,, \tag{2.4}$$

and it has the minimal property[1] such that

$$\Omega[\hat{\rho}] > \Omega[\hat{\rho}_0] \quad \text{for} \quad \hat{\rho} \neq \hat{\rho}_0\,, \tag{2.5}$$

[1] see the appendix of Mermin's paper [56] for a proof of this property.

where $\Omega[\hat{\rho}_0]$ denotes the grand potential

$$\Omega = -\frac{1}{\beta} \ln \left[\mathrm{Tr} \left(e^{-\beta(\hat{H}-\mu\hat{N})} \right) \right] . \tag{2.6}$$

The equilibrium density is then given by

$$n(\boldsymbol{r}) = N \int \cdots \int \mathrm{d}\boldsymbol{r}_2 \cdots \mathrm{d}\boldsymbol{r}_N \langle \boldsymbol{r}, \boldsymbol{r}_2, \ldots, \boldsymbol{r}_N | \hat{\rho}_0 | \boldsymbol{r}, \boldsymbol{r}_2, \ldots, \boldsymbol{r}_N \rangle , \tag{2.7}$$

which is clearly a functional of $v(\boldsymbol{r})$ through the density operator $\hat{\rho}_0$. Now is the reverse claim true, that $v(\boldsymbol{r})$ is a functional of $n(\boldsymbol{r})$? The answer, as Mermin shows, is yes to within a trivial additive constant. To show that $v(\boldsymbol{r})$ is a unique functional of $n(\boldsymbol{r})$ (within an additive constant), suppose there were another potential $v'(\boldsymbol{r})$ that gave rise to the same density $n(\boldsymbol{r})$; with Hamiltonian $\hat{H}'$, density operator $\hat{\rho}_0'$, and grand potential Ω'. By definition $v(\boldsymbol{r}) \neq v'(\boldsymbol{r})$, implying that $\hat{\rho}_0 \neq \hat{\rho}_0'$ because even if $v(\boldsymbol{r})$ only differs from $v'(\boldsymbol{r})$ by a constant, the constant term would vanish from both equilibrium density operators but the chemical potentials would still prevent agreement between the two expressions. By the minimal property of the equilibrium density operator eqn. 2.5 we have

$$\begin{aligned} \Omega'[\hat{\rho}_0'] = \mathrm{Tr} \left[\hat{\rho}_0' \left(\hat{H}' - \mu\hat{N} + \frac{1}{\beta} \ln \left(\hat{\rho}_0' \right) \right) \right] &< \Omega'[\hat{\rho}_0] = \mathrm{Tr} \left[\hat{\rho}_0 \left(\hat{H}' - \mu\hat{N} + \frac{1}{\beta} \ln \left(\hat{\rho}_0 \right) \right) \right] \\ &= \Omega[\hat{\rho}_0] + \mathrm{Tr} \left[\hat{\rho}_0 \left(\hat{V}' - \hat{V} \right) \right] . \end{aligned} \tag{2.8}$$

Likewise eqn. 2.8 functions just as well if the primed and unprimed labels are swapped:

$$\Omega[\hat{\rho}_0] < \Omega'[\hat{\rho}_0'] + \mathrm{Tr} \left[\hat{\rho}_0 \left(\hat{V} - \hat{V}' \right) \right] , \tag{2.9}$$

which when added together with eqn. 2.8 imply that

$$\Omega[\hat{\rho}_0] + \Omega'[\hat{\rho}_0'] < \Omega'[\hat{\rho}_0'] + \Omega[\hat{\rho}_0] , \tag{2.10}$$

and thus we have arrived at a contradiction, meaning that $v(\boldsymbol{r})$ must be the unique potential that gives rise to the density $n(\boldsymbol{r})$. Now because the density $n(\boldsymbol{r})$ uniquely determines $v(\boldsymbol{r})$, which then also fully determines $\hat{\rho}_0$, the equilibrium density operator must be a functional of $n(\boldsymbol{r})$. Equation. 2.3 can then be rewritten as

$$\begin{aligned} \Omega[n] &= \mathrm{Tr} \left[\hat{\rho}[n] \left(\hat{H} - \mu\hat{N} + \frac{1}{\beta} \ln \left(\hat{\rho}[n] \right) \right) \right] \\ &= \mathrm{Tr} \left[\hat{\rho}[n] \left(\hat{K} + \hat{U} + \frac{1}{\beta} \ln \left(\hat{\rho}[n] \right) \right) \right] + \int \mathrm{d}\boldsymbol{r} \, (v(\boldsymbol{r}) - \mu) n(\boldsymbol{r}) \end{aligned} \tag{2.11}$$

and we can identify the universal functional $F[n]$ that depends only on the density $n(\boldsymbol{r})$ as

$$F[n] = \mathrm{Tr}\left[\hat{\rho}[n]\left(\hat{K} + \hat{U} + \frac{1}{\beta}\ln\left(\hat{\rho}[n]\right)\right)\right] = K[n] + U[n] - \frac{1}{\beta}S[n]\,, \tag{2.12}$$

where $S[n]$ is the entropy functional. The functional eqn. 2.11 is equal to the grand potential eqn. 2.2 when $n(\boldsymbol{r})$ is the proper equilibrium density corresponding to the potential $v(\boldsymbol{r})$, and the minimal property is translated to

$$\Omega[n'] > \Omega[n] \quad \text{for} \quad n' \neq n\,, \tag{2.13}$$

thus defining a variational principle [56]. The procedure to find the correct $n(\boldsymbol{r})$ then amounts to solving

$$\frac{\delta}{\delta n(\boldsymbol{r})}\left(\Omega[n] + \mu N\right) = 0\,, \tag{2.14}$$

where the second term accounts for the constraint of constant average particle number.

2.1.2 Kohn-Sham Density Functional Theory

The Hohenberg-Kohn-Mermin theorems tell us that the unique ground state electron density exists, but they have relatively little wisdom on how one might go about finding it. The idea of Kohn and Sham [41] was to decompose the kinetic energy functional $K[n]$ into an interacting $K_{xc}[n]$ and "non-interacting" $K_s[n]$ part:

$$\Omega[n] = K_s[n] + K_{xc}[n] + U[n] - \mu N - \frac{1}{\beta}S[n] + \int \mathrm{d}\boldsymbol{r}\, v(\boldsymbol{r})n(\boldsymbol{r})\,, \tag{2.15}$$

where $K_{xc}[n]$ is typically called the exchange-correlation functional, and it encodes the energy due to particle exchange and correlation effects. Applying the variational principle to eqn. 2.15 and functionally differentiating both sides with respect to $n(\boldsymbol{r})$ yields

$$\frac{\delta\Omega[n]}{\delta n(\boldsymbol{r})} = \mu = \frac{\delta K_s[n]}{\delta n(\boldsymbol{r})} + \frac{\delta K_{xc}[n]}{\delta n(\boldsymbol{r})} + \frac{\delta U[n]}{\delta n(\boldsymbol{r})} - \frac{1}{\beta}\frac{\delta S[n]}{\delta n(\boldsymbol{r})} + v(\boldsymbol{r})\,, \tag{2.16}$$

where μ is the Lagrange multiplier associated with constant average particle number. Equation 2.16 has the form of a system interacting through a central potential (i.e. no particle-particle interactions) if we define

$$v_{\mathrm{eff}}(\boldsymbol{r}) = \frac{\delta K_{xc}[n]}{\delta n(\boldsymbol{r})} + \frac{\delta U[n]}{\delta n(\boldsymbol{r})} - \frac{1}{\beta}\frac{\delta S[n]}{\delta n(\boldsymbol{r})} + v(\boldsymbol{r})\,, \tag{2.17}$$

transforming eqn. 2.16 into

$$\mu = \frac{\delta K_s[n]}{\delta n(\boldsymbol{r})} + v_{\text{eff}}(\boldsymbol{r})\,. \tag{2.18}$$

The next idea of Kohn and Sham was to solve eqn. 2.18 by solving the auxiliary eigenvalue equation for the eigenfunctions $\phi_i(\boldsymbol{r})$:

$$\left[\frac{\delta K_s[n]}{\delta n(\boldsymbol{r})} + v_{\text{eff}}(\boldsymbol{r})\right]\phi_i(\boldsymbol{r}) = \varepsilon_i\phi_i(\boldsymbol{r})\,, \tag{2.19}$$

which then leads to an expression for the density $n(\boldsymbol{r})$:

$$n(\boldsymbol{r}) = \sum_i f(\varepsilon_i - \mu)|\phi_i(\boldsymbol{r})|^2\,, \tag{2.20}$$

where $f(\varepsilon_i - \mu)$ are the occupation numbers (e.g. the Fermi-Dirac or Bose-Einstein distributions for Fermions and Bosons, respectively). It is customary to refer to the eigenfunctions $\phi_i(\boldsymbol{r})$ as orbitals due to the resemblance with Hartree-Fock theory, and they carry with them the interpretation of being the solutions to a Schrödinger equation for a fictitious system of non-interacting particles whose density happens to correspond to the density of the original interacting system [41, 33, 61].

The exchange-correlation functional $K_{xc}[n]$ is exact in principle, but nearly impossible to find a closed-form expression for due in part to the non-local [61] and discontinuous [23] nature of the exchange-correlation potential. Much of DFT research involves finding increasingly accurate exchange-correlation functionals, with the hope of reaching the exact form one day [61, 33, 35]. KS-DFT represents a brilliant scheme to develop useful approximations for the exact kinetic energy functional $K[n]$, since the orbital eigenvalue equation 2.19 is just as readily solved as the Hartree-Fock version is [33, 61]. However, the need to solve an eigenvalue equation for each particle in the N-particle system scales like $O(N^3)$, which becomes extremely cumbersome for even moderately sized solid-state systems [35, 13, 85]. OF-DFT is an attempt to remedy this situation and will be discussed in the next subsection 2.1.3.

2.1.3 Orbital-Free Density Functional Theory

The original model of Thomas and Fermi used the electron density to describe the properties of a neutral atom, without introducing any fictitious systems as in KS-DFT. The economy of this approach is that there is only one equation for the density $n(\boldsymbol{r})$ that must be solved as opposed

to N equations for each orbital of the Kohn-Sham equation 2.19 [61, 33]. This represents one of the limitations of extending KS-DFT to more complicated physical systems, as the $\mathcal{O}(N^3)$ steps required by typical computer implementations scales very poorly and becomes extremely computationally expensive for larger systems ($> 10^2$ particles)[2] [85, 13, 35]. Contrast this situation with the $\mathcal{O}(M \log(M))$ steps (M represents the number of basis functions spanning the space) [85] required by the orbital-free approach. KS-DFT is clearly unsuitable for studying large solid-state systems, as they appear in materials research [84] and biological systems [33], which is one of the primary motivations of pursuing the OF-DFT approach.

OF-DFT has distinguished itself with the promise of better computational scaling among other attributes, but introduces a serious problem that has been the sole focus of many researchers and has prevented its widespread acceptance: The non-interacting kinetic energy must now be approximated in the absence of orbitals or the exact density [35]. The non-interacting kinetic energy is typically of comparable magnitude to the total energy, making the approximation of this term potentially very costly. KS-DFT on the other-hand, can calculate the non-interacting kinetic energy exactly, which is partly the reason why it is the most popular framework for DFT [33, 61].

As the name suggests, OF-DFT is an attempt to return to the ideas of Thomas and Fermi by dealing only with the raw electron density $n(\boldsymbol{r})$. OF-DFT typically starts off with the Kohn-Sham equation and even employs the same decomposition of the kinetic energy functional as in KS-DFT, except that instead of using multiple orbitals $\phi_i(\boldsymbol{r})$, the square root of the density is used as a sort of pseudo-orbital [50, 13, 35]:

$$\left[\frac{\delta K_s[n]}{\delta n(\boldsymbol{r})} + v_P(\boldsymbol{r}) + v_{KS}(\boldsymbol{r})\right]\sqrt{n(\boldsymbol{r})} = \mu\sqrt{n(\boldsymbol{r})}\,, \tag{2.21}$$

where $v_{KS}(\boldsymbol{r})$ is the effective potential from KS-DFT and $v_P(\boldsymbol{r})$ is a potential to explicitly account for the Pauli-exclusion principle, since the lack of orbitals makes endowing the density with the appropriate particle statistics a more obscure process [47, 35]. One thing to note is that the square-root of the density in eqn. 2.21 is normalized to the particle number N, as opposed to traditional orbitals being normalized to unity [35].

In the OF-DFT literature, the starting point for constructing approximate expressions for the non-interacting kinetic energy $K_s[n]$ is usually through the Thomas-Fermi and von Weizsacker functionals respectively [35]:

$$K_{TF}[n] = \frac{3}{10}(3\pi^2)^{\frac{2}{3}}\int \mathrm{d}\boldsymbol{r}\, n^{\frac{5}{3}}(\boldsymbol{r}) \quad \text{and} \quad K_{vW}[n] = \frac{1}{8}\int \mathrm{d}\boldsymbol{r}\, \frac{|\nabla n(\boldsymbol{r})|^2}{n(\boldsymbol{r})}\,. \tag{2.22}$$

[2] Linear scaling algorithms for KS-DFT do exist, but they typically only become linear for sufficiently large systems and often with a large numerical prefactor that grows with the number of subdomains [85].

The von Weizsacker functional is exact for one and two electron systems, while the Thomas-Fermi functional is one of the simplest orbital-free expressions one can implement and performs quite well [61, 33], although fails to predict atomic shell structure or molecular bonding [75].

2.2 Polymer Self-Consistent Field Theory

The model constructed in this thesis will turn out to rely heavily on the mathematics of polymer SCFT, so we devote this section to building up the physical picture associated with polymers and sketching out the relevant mathematical tools. The material presented here closely follows references [52, 54, 51].

Polymer SCFT is an approach to describing long chains of molecules by coarse-graining out their individual structure and using a field to describe the bulk properties of the chain. In the absence of interactions, the basic idea is that for sufficiently large chains, the quantum-mechanical details have a relatively small impact on the macroscopic chain behaviour and they can effectively be ignored. This can be seen as a consequence of the central limit theorem in probability theory, since each molecule is governed by a probability distribution determined by solving its Schrödinger equation, the limit as the number of molecules goes toward infinity will tend to a Gaussian distribution [52]. Mathematically, this looks like

$$\lim_{n\to\infty} p_n(\boldsymbol{r}) = \left(\frac{3}{2\pi a^2}\right)^{\frac{3}{2}} \exp\left(-\frac{3r^2}{2a^2}\right), \tag{2.23}$$

where n is the number of molecules comprising the chain, $p_n(\boldsymbol{r})$ is the probability distribution of each molecules' position, and a is the statistical length of each segment of the chain. The fact that the molecules could all have different distributions whose details are washed away in the limit, leads to a notion of universality in polymer systems, where bulk properties of the polymer do not depend on the individual fine details of the molecules. In practice, Gaussian behaviour can usually be well-approximated with only a few dozen molecules per chain [52].

Now suppose that a collection of ℓ chains interact via an external field $\phi(\boldsymbol{r}_1, \ldots, \boldsymbol{r}_\ell)$ that does not fluctuate too rapidly, and is such that each of the N chain constituents for an individual chain are still approximately Gaussian-distributed over some neighbourhood. Denote the position of each chain segment through the parametrization $\boldsymbol{r}_i(s)$, where the parameter s runs along the extent of the chain and the index i refers to a specific chain out of a total of ℓ chains. The distribution

functional of the chain position from $\boldsymbol{r}_i(s_1)$ to $\boldsymbol{r}_i(s_2)$ is given by

$$P[\boldsymbol{r}_i](s_1, s_2) = \frac{1}{Z} \exp\left[-\beta \int_{s_1}^{s_2} \mathrm{d}s \left(\frac{3}{2a^2 N} \left| \frac{\mathrm{d}\boldsymbol{r}_i(s)}{\mathrm{d}s} \right|^2 + \phi(\boldsymbol{r}_1(s), \ldots, \boldsymbol{r}_\ell(s)) \right)\right], \tag{2.24}$$

where Z is a normalization constant and β is the reciprocal thermal energy $k_B T$. Notice that the quantity in the exponential has the same form as the action in classical mechanics, except that the dynamics described here are with respect to the chain parameter s, so the argument of the exponential can be associated with an energy for the interval $[s_1, s_2]$. We can then see that the first term of eqn. 2.24 is a kinetic energy related to the Gaussian probability mentioned earlier, while the second is a potential energy related to interactions with the field ϕ.

The normalization constant in eqn. 2.24 is actually the familiar partition function and encodes all of the thermodynamic properties of the system. To express it, first note that the distribution functional eqn. 2.24 is the kernel of a process that propagates the system at positions $\boldsymbol{r}_i(s_1)$ to positions $\boldsymbol{r}_i(s_2)$. And since there are a continuum of paths between the two sets of positions, parametrized by the parameter s, an infinite number of integrations are needed in order to describe propagation along all possible paths, where the paths actually represent possible configurations that the chains could have. The integration of the distribution functional eqn. 2.24 along all these configurations from $\boldsymbol{r}_i(s_1)$ to $\boldsymbol{r}_i(s_2)$ is called the propagator and it is expressed through the path integral [54] as

$$G(\boldsymbol{r}_i(s_1), \boldsymbol{r}_i(s_2)) = \prod_i^{\ell} \int_{\boldsymbol{r}_i(s_1)}^{\boldsymbol{r}_i(s_2)} \mathcal{D}[\boldsymbol{r}_i(s)] e^{-\beta \int_{s_1}^{s_2} \mathrm{d}s \left(\frac{3}{2a^2 N} \left| \frac{\mathrm{d}\boldsymbol{r}_i(s)}{\mathrm{d}s} \right|^2 + \phi(\boldsymbol{r}_1(s), \ldots, \boldsymbol{r}_\ell(s)) \right)}, \tag{2.25}$$

where $\mathcal{D}[\boldsymbol{r}_i(s)] = \lim_{M \to \infty,\, \epsilon \to 0} \mathcal{A}(M, \epsilon) \prod_i^M \mathrm{d}\boldsymbol{r}_i$ denotes the integration measure; with discretization ϵ and formally infinite normalization constant $\mathcal{A}(M, \epsilon)$. Since phase space consists of position and momentum coordinates, but no momentum coordinates have appeared so far, the normalization constant $\mathcal{A}$ is the result of integrating away the degrees of freedom from the momenta. We shall not be concerned with the value of $\mathcal{A}$, as it typically drops out in the quantities of interest in polymer SCFT [52].

It is at this point that we specialize to polymer chains which start and end at the same set of positions $\boldsymbol{r}_i(s_1) = \boldsymbol{r}_i(s_2) \equiv \boldsymbol{r}_i$, otherwise known as ring polymers, in anticipation of things to come [31]. The partition function for a system of ring polymers is then obtained by integrating over all positions $\boldsymbol{r}_i$:

$$Z = \int \mathrm{d}\boldsymbol{r}_1 \cdots \mathrm{d}\boldsymbol{r}_\ell \, G(\boldsymbol{r}_1(s_1), \ldots, \boldsymbol{r}_\ell(s_1); \boldsymbol{r}_1(s_2), \ldots, \boldsymbol{r}_\ell(s_2)) \,. \tag{2.26}$$

Equation 2.26 is a formidable expression that is tough to evaluate in its current form. What is usually done in SCFT instead, is to convert the interaction of the ℓ chains with the field ϕ into an interaction of a single non-interacting chain with a field $\Phi(\boldsymbol{r})$. This can be accomplished by inserting the Dirac delta functional identity $1 = \int \mathcal{D}[\Phi]\delta[\Phi - \phi]$ into eqn. 2.25 and then expressing the Dirac delta functional in its Fourier representation [54, 19]. The Fourier representation allows for the exponential in eqn. 2.25 to be factored into a product of ℓ single-particle propagators $q(\boldsymbol{r}, \boldsymbol{r}, s)$, which can then each be integrated over their position to define ℓ single-particle partition functions Q. As shown in appendix B (with a different diffusion constant), each single-particle propagator satisfies a diffusion equation

$$\frac{\partial q(\boldsymbol{r}, \boldsymbol{r}', s)}{\partial s} = \left(\frac{a^2 N}{6}\nabla^2 - \Phi(\boldsymbol{r})\right) q(\boldsymbol{r}, \boldsymbol{r}', s)\,, \tag{2.27}$$

with the initial condition $q(\boldsymbol{r}, \boldsymbol{r}', 0) = \delta(\boldsymbol{r} - \boldsymbol{r}')$, which allows for the single-particle partition functions to be evaluated exactly. The procedure just described will be shown with more explicit detail in chapter 3; references [52, 51, 54, 19, 31] can be consulted for more information.

2.3 The Quantum-Classical Correspondence

The pioneering work of Feynman [18] in developing the path integral formulation of quantum theory led to the development of one of the most useful objects (notoriously difficult to deal with analytically) in the study of quantum theory, the field of stochastic processes, and polymer field theory: the path integral. It was this object that originally led Feynman to deduce the similarity between quantum mechanics and the statistical mechanics of ring-like molecules, which was facilitated through the transformation of the time variable $t = -i\hbar\beta$ to the imaginary time parameter $\hbar\beta$ [17]. Such a transformation is well-known to field theorists, and it is generally called the Wick rotation. The Wick rotation essentially allows one to transform a dynamics problem into a statics problem in one higher dimension, where temporal variables are typically exchanged for spatial variables [44].

Part of the intuition behind why the Wick rotation takes quantum mechanics to the statistical mechanics of ring-like molecules stems from the nature of the trace operator in the partition function, which is a sum of the Boltzmann factors over configurations starting and ending at the same position. This cyclic aspect is crucial to the interpretation, especially after having transferred to the path integral picture, because the path integral allows one to see that the trajectories followed through the imaginary time configuration parameter space each correspond to the different possible arrangements of quantum particles comprising a system of quantum

particles [17, 12]; where the correspondence with the mathematics of polyatomic fluids noted by Chandler [12] lends itself to label each of the quantum particles in the system as atoms making up a molecule. The probabilistic uncertainty in the position and momenta of the quantum system are then manifested as the collection of system arrangements associated to a given configuration. The connection to polymer SCFT is then made clear with the help of the previous section and the insights of Matsen [52]. The periodicity of the imaginary time parameter also happens to be a part of one of the conditions to be a Kubo-Martin-Schwinger (KMS) state, which is a general notion of being in a thermal state [24].

Although the mathematics is essentially identical between the quantum-mechanical and polymeric systems, the interpretation of the fundamental constituents and the mechanisms that govern their behaviour has changed dramatically. In the quantum-mechanical case the time evolution of the system could trace out many different paths, forming a distribution of them that expresses the uncertainty in which path will be followed. In the statistical-mechanical case the system could explore many different energy configurations, forming a distribution of them where thermal fluctuations represent the uncertainty in which configuration will be chosen.

The work of Chandler [12] is greatly responsible for the modern development of the quantum-classical correspondence, which they originally titled the "quantum-classical isomorphism", into a useful framework for quantum simulations. Some methodologies that have been built around this correspondence include ring polymer molecular dynamics [67], Feynman path centroid dynamics [65], centroid molecular dynamics [86], and path-integral Monte Carlo [11]. As was mentioned in chapter 1, Thompson [78] has extended the framework of the quantum-classical correspondence to bridge finite-temperature quantum DFT with ring polymer SCFT, allowing for potential application of the previous simulation methods to DFT.

Chapter 3

A Polymeric Self-Consistent Field Approach to Quantum Density Functional Theory

The observations of Feynman [17], Chandler [12], and others that quantum theory could be mapped to the classical statistical mechanics of ring polymers through the transformation $t = -i\hbar\beta$, represents a very interesting opportunity to explore quantum theory using the machinery and physical intuition from polymer SCFT. As shown in section 3.1, the free energy eqn. 3.18 one arrives at in polymer SCFT after approximating the partition function eqn. 3.17 with the extremum of the integrand very closely resembles the free energy expression derived from the Hohenberg-Kohn-Mermin theorems (in the canonical ensemble of course). In particular, the free energy resembles the OF-DFT expression for the free energy because orbitals are not typically used in polymer SCFT; the reason being that KS-DFT does not scale nicely for large numbers of particles, which is characteristic of polymer systems. This suggests an equivalence between polymer SCFT and quantum DFT, where polymer SCFT plays the role of the classical counterpart in the quantum-classical correspondence. Indeed, such a relationship has already been exposed by Thompson [78], who has successfully applied their framework to simple atomic systems in their ground-state and to diatomic molecules [72].

Alternative approaches to DFT have been greatly explored over the years, in an effort to both increase the accuracy of the results and diversify the range of complex systems available to be studied. OF-DFT represents the latest attempt to accomplish this goal [35], and the framework of Thompson capitalizes on it by shifting the background to the classical regime, where concepts

seem more physically intuitive to us. Thompson's framework represents not only a useful computational tool to do practical calculations with, but also provides a readily understandable interpretation for the objects appearing in the theory.

In the following few sections, the theory behind the model will be expounded and the model equations derived from first principles. A new derivation of the SCFT equations different from the approach taken by Thompson [78] is first presented in section 3.1. The spectral method used to transform the SCFT equations into a computer ready implementation is then introduced in section 3.2 along with the Gaussian basis set that is used in this work. The SCFT equations are then converted into their spectral form after having modified them to accommodate the non-orthogonal nature of the Gaussians. In section 3.3, the fields at play in the model are introduced and discussed at length. Finally in section 3.4, the full spectral form of the free energy expression is presented and the spectral SCFT equations summarized for convenience.

3.1 Derivation of SCFT Equations

This derivation combines some elements of [78] and [54], but has otherwise been done independently. As in [78], the Hohenberg-Kohn-Mermin theorems are not used initially to better demonstrate the equivalence of SCFT with DFT; it is only after the fact that they are invoked to further the connection to the rest of quantum theory. For simplicity and clarity we work in the canonical ensemble, where the N-body partition function is expressed as

$$Q_N = \mathrm{Tr}(e^{-\beta\mathcal{H}}) \,, \tag{3.1}$$

assuming $e^{-\beta\mathcal{H}}$ is trace-class and representable through a power series. The parameter β is the Lagrange multiplier that ensures the expectation value of the free energy remains constant and $\mathcal{H}$ is the Hamiltonian of the system. In this work we are interested in single atomic systems, so the Hamiltonian will take the standard form as seen in the many-body Schrödinger equation for atomic systems under the Born-Oppenheimer approximation [70], with the potential operator simply denoted by $\hat{U}$.

The trace operator has the property that it is invariant with respect to the choice of basis used to represent the operator $e^{-\beta\mathcal{H}}$, therefore we are free to pick the configuration space representation composed of the N-body configurations $\{\boldsymbol{r}_i\}_{i=1}^{N}$, where $\mathcal{H}$ is diagonal. Before proceeding, we will make use of the resolution of the identity operator in this basis, which is given by the expression

$$I = \prod_{i}^{N} \int \mathrm{d}\boldsymbol{r}_i \, |\boldsymbol{r}_i\rangle\langle\boldsymbol{r}_i| \,. \tag{3.2}$$

After inserting eqn. 3.2 into the trace operator in eqn. 3.1, the outer product becomes an inner product and eqn. 3.1 becomes

$$Q_N(\beta) = \prod_i^N \int \mathrm{d}\boldsymbol{r}_i \, \langle \boldsymbol{r}_i | e^{-\beta \mathcal{H}} | \boldsymbol{r}_i \rangle \, . \tag{3.3}$$

To properly enforce indistinguishability among quantum particles, the above expression should be modified by adding a $1/N!$ term, which accounts for the non-uniqueness of the $N!$ possible permutations of an arrangement of N identical bodies. The enforcement of particle statistics further warrants replacing the right ket with the permutation operator $\hat{P}$ acting on it $|\hat{P}\boldsymbol{r}_i\rangle$ and then summing over all possible permutations P, multiplied by a term $(\pm 1)^P$, where the $(+)$ corresponds to Bosons and the $(-)$ to Fermions [36, 39]. Later in this derivation, we will find a way to enforce these conditions in a different manner, which is possibly more physically motivated and intuitive; for now we proceed without the extra notational baggage.

In the N-body position basis, the Hamiltonian can be expressed as

$$H(\boldsymbol{r}_1, \ldots, \boldsymbol{r}_N) = -\sum_i^N \frac{\hbar^2}{2m} \nabla_i^2 + U(\boldsymbol{r}_1, \ldots, \boldsymbol{r}_N) \, . \tag{3.4}$$

If we now define an electron density operator in the position representation as

$$\hat{n}(\boldsymbol{r}) = \sum_i^N \delta(\boldsymbol{r} - \boldsymbol{r}_i) \, , \tag{3.5}$$

then the configuration Hamiltonian eqn. 3.4 can be expressed as a functional of $\hat{n}(\boldsymbol{r})$:

$$H[\hat{n}] = -\sum_i \frac{\hbar^2}{2m} \nabla_i^2 + U[\hat{n}](\boldsymbol{r}_1, \ldots, \boldsymbol{r}_N) \, . \tag{3.6}$$

After substituting eqn. 3.6 into Q_N, the expectation value in eqn. 3.3, as shown in appendix B, can be expressed as a path integral:

$$G(\boldsymbol{r}_i, \boldsymbol{r}_i, \beta) \equiv \langle \boldsymbol{r}_i | e^{-\beta \mathcal{H}[\hat{n}]} | \boldsymbol{r}_i \rangle = \int_{\boldsymbol{r}_i}^{\boldsymbol{r}_i} \mathcal{D}[\boldsymbol{r}_i(\tau)] e^{-\int_0^\beta \mathrm{d}\tau \left[\sum_j \frac{m}{2\hbar^2} \left| \frac{\mathrm{d}\boldsymbol{r}_j(\tau)}{\mathrm{d}\tau} \right|^2 + U[\hat{n}](\boldsymbol{r}_1(\tau), \ldots, \boldsymbol{r}_N(\tau)) \right]} \, , \tag{3.7}$$

where $\mathcal{D}[\boldsymbol{r}_i(\tau)] = \lim_{N \to \infty, \epsilon \to 0} \mathcal{A}(N, \epsilon) \prod_i^N \mathrm{d}\boldsymbol{r}_i$ denotes the integration measure; with discretization ϵ and formally infinite normalization constant $\mathcal{A}(N, \epsilon)$ [18]. The path integral eqn. 3.7 (also shown in appendix B) is fully equivalent to the diffusion equation

$$\frac{\partial G(\{\boldsymbol{r}\}, \{\boldsymbol{r}'\}, s)}{\partial s} = -\mathcal{H} G(\{\boldsymbol{r}\}, \{\boldsymbol{r}'\}, s) \tag{3.8}$$

with the initial condition $G(\{\boldsymbol{r}\},\{\boldsymbol{r}'\},s) = \prod_i^N \delta(\boldsymbol{r}_i - \boldsymbol{r}'_i)$. The function G can be seen as a propagator which evolves the N-body system configuration through the s parameter space from the configuration of the system at $\{\boldsymbol{r}\}$ to $\{\boldsymbol{r}'\}$. In the case of eqn. 3.7, the trajectory followed by the system can be readily interpreted as a random walk along a polymer chain, which starts off in the classical localized state represented by the Dirac delta function, and ends up at the same starting position in the probabilistic configuration characterized by the β parameter. Thus far we have not assigned an interpretation to the parameter β beyond its designation as the Lagrange multiplier that fixes the expectation value of the free energy. As the quantum-classical correspondence shows, the parameter $\hbar\beta$ is something akin to an imaginary time, and because the trajectory starts and ends at the same configuration, $\hbar\beta$ serves as an imaginary period of the propagator G. As is well known in condensed matter theory, the imaginary period of the many-body propagator is proportional to the reciprocal thermal energy $k_B T$ (where k_B is Boltzmann's constant and T is the temperature) of the system $\beta = 1/k_B T$ [44], which is a part of the KMS condition that defines a notion of thermality for the system [24]. Henceforth, in order to connect with empirical results, the parameter β will correspond to the reciprocal thermal energy of the system.

The exponential in the path integral eqn. 3.7 is a functional of the density operator $\hat{n}$ and as such, we can re-express the part corresponding to $U[\hat{n}]$ in terms of another function $\mathcal{N}$ through the functional identity

$$\int \mathcal{D}[\mathcal{N}]\delta[\mathcal{N} - \hat{n}]M[\mathcal{N}] = M[\hat{n}]\,, \tag{3.9}$$

where M is an arbitrary functional [19, 54]. The functional Dirac delta may be expressed through the functional Fourier transform as

$$\delta[\mathcal{N} - \hat{n}] = \int_{-i\infty}^{i\infty} \mathcal{D}[W] e^{\beta \int \mathrm{d}\boldsymbol{r}' W(\boldsymbol{r}')(\mathcal{N}(\boldsymbol{r}') - \hat{n}(\boldsymbol{r}'))}\,. \tag{3.10}$$

The resulting expression for the partition function eqn. 3.3 then takes the form

$$\begin{aligned} Q_N(\beta) = \int \int \mathcal{D}[\mathcal{N}]\mathcal{D}[W] \prod_i^N \int \mathrm{d}\boldsymbol{r}_i \\ \times \int_{\boldsymbol{r}_i}^{\boldsymbol{r}_i} \mathcal{D}[\boldsymbol{r}_i(\tau)] e^{-\int_0^\beta \mathrm{d}\tau \left[\sum_j \frac{m}{2\hbar^2}\left|\frac{\mathrm{d}\boldsymbol{r}_j(\tau)}{\mathrm{d}\tau}\right|^2 + U[\mathcal{N}] - \int \mathrm{d}\boldsymbol{r}' W(\boldsymbol{r}')(\mathcal{N}(\boldsymbol{r}') - \hat{n}(\boldsymbol{r}'))\right]}\,. \end{aligned} \tag{3.11}$$

The potential $U[\mathcal{N}]$ is now coordinate independent and the integral of it with respect to τ simply evaluates to $\beta U[\mathcal{N}]$. The coordinate dependencies are now exclusively contained in the $\hat{n}$ term from the integral representation of the Dirac delta eqn. 3.10, which we can use to rewrite the Fourier kernel in eqn. 3.10 as

$$e^{\beta \int \mathrm{d}\boldsymbol{r}' W(\boldsymbol{r}')(\mathcal{N}(\boldsymbol{r}') - \hat{n}(\boldsymbol{r}'))} = e^{\beta \int \mathrm{d}\boldsymbol{r}' W(\boldsymbol{r}')\mathcal{N}(\boldsymbol{r}')} e^{-\sum_i \beta \int \mathrm{d}\boldsymbol{r}' W(\boldsymbol{r}')\delta(\boldsymbol{r}' - \boldsymbol{r}'_i)}$$

$$= e^{\beta \int \mathrm{d}\boldsymbol{r}' W(\boldsymbol{r}') \mathcal{N}(\boldsymbol{r}')} e^{-\sum_i \beta W(\boldsymbol{r}_i')} \,. \tag{3.12}$$

Equation 3.12 can be substituted back into eqn. 3.11, noting that the field W in the argument of the second exponential factor is actually dependent on $\{\boldsymbol{r}_i(\tau)\}_{i=1}^N$ when appearing in eqn. 3.11 and that the argument of the first exponential factor is coordinate independent, to yield

$$\begin{aligned} Q_N(\beta) = \int \int \mathcal{D}[\mathcal{N}]\mathcal{D}[W] e^{-\beta U[\mathcal{N}] + \beta \int \mathrm{d}\boldsymbol{r}' W(\boldsymbol{r}')(\mathcal{N}(\boldsymbol{r}')} \\ \times \prod_i^N \int \mathrm{d}\boldsymbol{r}_i \int_{\boldsymbol{r}_i}^{\boldsymbol{r}_i} \mathcal{D}[\boldsymbol{r}_i(\tau)] e^{-\int_0^\beta \mathrm{d}\tau \sum_j \left[\frac{m}{2\hbar^2} \left| \frac{\mathrm{d}\boldsymbol{r}_j(\tau)}{\mathrm{d}\tau} \right|^2 + W(\boldsymbol{r}_j(\tau)) \right]} \,. \end{aligned} \tag{3.13}$$

The argument of the exponential in the configuration path integral is now completely separable into N one-body terms, producing a product of N separable path integrals. The configuration integrals can then be evaluated one at a time with the result being N identical terms. Thus, we define a one-body partition function as

$$Q[W](\beta) = \mathcal{A} \int \mathrm{d}\boldsymbol{r} \int_{\boldsymbol{r}}^{\boldsymbol{r}} \mathcal{D}[\boldsymbol{r}(\tau)] e^{-\int_0^\beta \mathrm{d}\tau \left[\frac{m}{2\hbar^2} \left| \frac{\mathrm{d}\boldsymbol{r}(\tau)}{\mathrm{d}\tau} \right|^2 + W(\boldsymbol{r}(\tau)) \right]} \,, \tag{3.14}$$

where $\mathcal{A}$ is a normalization constant and we recognize from the similarity to eqn. 3.7 that the path integral defined above constitutes a one-body propagator [54], which we denote as

$$q(\boldsymbol{r}, \boldsymbol{r}', s) = \mathcal{A} \int_{\boldsymbol{r}'}^{\boldsymbol{r}} \mathcal{D}[\boldsymbol{r}(\tau)] e^{-\int_0^s \mathrm{d}\tau \left[\frac{m}{2\hbar^2} \left| \frac{\mathrm{d}\boldsymbol{r}(\tau)}{\mathrm{d}\tau} \right|^2 + W(\boldsymbol{r}(\tau)) \right]} \,. \tag{3.15}$$

$q(\boldsymbol{r}, \boldsymbol{r}', s)$ then equivalently satisfies the following diffusion equation

$$\frac{\partial q(\boldsymbol{r}, \boldsymbol{r}', s)}{\partial s} = -H_{\text{eff}} q(\boldsymbol{r}, \boldsymbol{r}', s) = \frac{\hbar^2}{2m} \nabla^2 q(\boldsymbol{r}, \boldsymbol{r}', s) - W(\boldsymbol{r}) q(\boldsymbol{r}, \boldsymbol{r}', s) \,, \tag{3.16}$$

with initial condition $q(\boldsymbol{r}, \boldsymbol{r}', 0) = \delta(\boldsymbol{r} - \boldsymbol{r}')$. It is worth pointing out that the Hamiltonian H_{eff} above is the same Hamiltonian appearing in KS-DFT which describes the non-interacting electron density; a demonstration of the equivalence between this model and KS-DFT can be found in appendix B of Thompson [78]. The one-body partition function eqn. 3.14 can then be expressed as $Q = \int \mathrm{d}\boldsymbol{r} q(\boldsymbol{r}, \boldsymbol{r}, \beta)$ and by solving the diffusion equation eqn. 3.16, Q can then be evaluated exactly. The N-body partition function can finally be expressed as

$$Q_N(\beta) = \int \int \mathcal{D}[\mathcal{N}]\mathcal{D}[W] \, e^{-\beta F[\mathcal{N}, W]} \,, \tag{3.17}$$

where

$$-\beta F[\mathcal{N}, W] = N \ln(Q[W](\beta)) - \beta U[\mathcal{N}] + \beta \int \mathrm{d}\boldsymbol{r}' W(\boldsymbol{r}')\mathcal{N}(\boldsymbol{r}') \,. \tag{3.18}$$

Although it is possible to analytically evaluate the functional eqn. 3.18, we are not so fortunate with eqn. 3.17, whose path integrals are too unwieldy to perform exact calculations with to get the free energy [54]. However, eqn. 3.18 plays the same role that the action does in the real-time quantum mechanical path integral, so a solution can be sought which minimizes $F[\mathcal{N}, W]$ by setting its first variation to zero and then approximating the integrand with the extremum of F. The free energy can then be calculated from $F[n, w]$, where n and w are the mean-fields for which the functional F has a saddle point. This procedure is common practice in SCFT [52, 54, 31], but notice that this is exactly what the Hohenberg-Kohn-Mermin theorems tell us, albeit in a slightly modified form. The theorems state that the ground state electron density $n(\boldsymbol{r}, \beta)$ is unique for a given external potential $w(\boldsymbol{r}, \beta)$ and vice-versa, meaning that the external potential can be taken to be a functional of the electron density, and a second variational principle with respect to the external potential can be interpreted as a self-consistent method for finding the electron density. In other words, the free energy functional F is extremized by the equilibrium electron density $n(\boldsymbol{r}, \beta)$ *and* its corresponding potential $w(\boldsymbol{r}, \beta)$. We can further justify the preservation of exactness in the model from varying eqn. 3.18, since any neglected higher-order contributions can be packaged into the unknown functional U, whose approximations occupy a large portion of current DFT research [33, 84, 35].

Proceeding from the variational principle outlined above, The mean-field density $n(\boldsymbol{r}, \beta)$ and field $w(\boldsymbol{r}, \beta)$ are obtained through

$$\frac{\delta F[n, w]}{\delta n(\boldsymbol{r}, \beta)} = 0 \quad \text{and} \quad \frac{\delta F[n, w]}{\delta w(\boldsymbol{r}, \beta)} = 0 \,, \tag{3.19}$$

to which we arrive at the expressions

$$\int \mathrm{d}\boldsymbol{r}' w(\boldsymbol{r}', \beta) \frac{\delta n(\boldsymbol{r}', \beta)}{\delta n(\boldsymbol{r}, \beta)} = \int \mathrm{d}\boldsymbol{r}' w(\boldsymbol{r}', \beta) \delta(\boldsymbol{r} - \boldsymbol{r}') = w(\boldsymbol{r}, \beta) = \frac{\delta U[n]}{\delta n(\boldsymbol{r}, \beta)} \tag{3.20}$$

$$\int \mathrm{d}\boldsymbol{r}' n(\boldsymbol{r}', \beta) \frac{\delta w(\boldsymbol{r}', \beta)}{\delta w(\boldsymbol{r}, \beta)} = \int \mathrm{d}\boldsymbol{r}' n(\boldsymbol{r}', \beta) \delta(\boldsymbol{r} - \boldsymbol{r}') = n(\boldsymbol{r}, \beta) = -\frac{N}{\beta Q[w]} \frac{\delta Q[w]}{\delta w(\boldsymbol{r}, \beta)} \,. \tag{3.21}$$

The functional derivative $\delta Q[w]/\delta w(\boldsymbol{r}, \beta)$ can be evaluated easily from the path integral representation of q (eqn. 3.15) since the field w only appears linearly in the argument of the exponential, so applying the functional derivative only brings down a term $-\int_0^\beta \mathrm{d}\tau = -\beta$[1] and

[1]This is only the case if we assume w is not s dependent, which will turn out to be an approximation when the field sources are discussed in section 3.3.

the mean-field density $n(\boldsymbol{r},\beta)$ is therefore expressed as

$$n(\boldsymbol{r},\beta) = \frac{N}{Q[w](\beta)} q(\boldsymbol{r},\boldsymbol{r},\beta)\,. \tag{3.22}$$

Returning now to the issue of particle statistics: the model so far expounded has not provided any clue on how to handle the radically differing behaviours of quantum particles, i.e. Bosons and Fermions. The first step in dealing with this issue for Fermions comes from the strategy proposed by Thompson [79], which is to postulate that each higher-dimensional ring polymer (described by eqn. 3.15) actually denotes a "pair" (0, 1 or 2) of quantum particles. If we label pairs with Greek indices, then the SCFT equations detailed in this section are modified in the following way.

$$\frac{\partial q_\mu(\boldsymbol{r},\boldsymbol{r}',s)}{\partial s} = \frac{\hbar^2}{2m}\nabla^2 q_\mu(\boldsymbol{r},\boldsymbol{r}',s) - w_\mu(\boldsymbol{r}) q_\mu(\boldsymbol{r},\boldsymbol{r}',s) \tag{3.23}$$

$$Q_\mu[w](\beta) = \int \mathrm{d}\boldsymbol{r}\, q_\mu(\boldsymbol{r},\boldsymbol{r},\beta) \tag{3.24}$$

$$n_\mu(\boldsymbol{r},\beta) = \frac{N_\mu}{Q_\mu[w](\beta)} q_\mu(\boldsymbol{r},\boldsymbol{r},\beta) \tag{3.25}$$

$$w_\mu(\boldsymbol{r},\beta) = \frac{\delta U[n_\mu]}{\delta n_\mu(\boldsymbol{r},\beta)}\,, \tag{3.26}$$

where the standard electron density $n(\boldsymbol{r},\beta)$, electron number N, and field $w(\boldsymbol{r},\beta)$ are built up from the relations

$$\sum_\mu n_\mu(\boldsymbol{r},\beta) = n(\boldsymbol{r},\beta)\,, \qquad \sum_\mu N_\mu = N\,, \qquad \sum_\mu w_\mu(\boldsymbol{r},\beta) = w(\boldsymbol{r},\beta)\,. \tag{3.27}$$

The free energy functional $F[n,w]$ (eqn. 3.18) also acquires these modifications in the form

$$F[n,w] = -\sum_\mu \frac{N_\mu}{\beta} \ln(Q_\mu[w](\beta)) + U[n] - \sum_\mu \int \mathrm{d}\boldsymbol{r} w_\mu(\boldsymbol{r},\beta) n_\mu(\boldsymbol{r},\beta)\,. \tag{3.28}$$

The above equations are actually still valid for Bosons, provided we do not restrict the number of particles comprising each "pair". The second step in our strategy to deal with particle statistics will be discussed when the fields in the model are introduced in section 3.3.

The introduction of "pairs" into the model marks a departure from traditional DFT by taking the μ^{th} pair electron density $n_\mu(\boldsymbol{r},\beta)$, electron number N_μ, and field $w_\mu(\boldsymbol{r},\beta)$ as the primitive

quantities. Our approach is not completely novel, although entirely independent, as there exists a variant of DFT called partition DFT [60], in which the authors posit that the electron density is built up from "atomic fragments" that play the same role as pairs do in our formalism. However, there are a number of fundamental differences between our formalism and partition DFT that can be exposed through a cursory reading of references [60, 79].

To solve the set of equations 3.23-3.26, we will make use of the spectral theorem from functional analysis [42] to decompose each function in terms of a linear combination of basis functions, which is detailed in the following section.

3.2 Spectral Method

Although expanding functions in terms of a set of basis functions has been a useful technique in solving problems since the early days of Hartree-Fock theory [74, 25, 64], the use of this method in the context of polymer SCFT and its computational advantages was most lucidly expounded by Matsen [54, 52], whom we follow throughout this section; wisdom from the vast literature on basis function methods in Hartree-Fock theory [27, 30, 74] is also imported.

Using traditional real-space numerical methods, the diffusion equation (eqn. 3.16) would have to be solved for all positions $\boldsymbol{r}'$ for each self-consistent iteration, which requires an enormous number of operations to complete and is therefore not computationally efficient [78, 54, 52]. Early researchers in atomic physics and quantum chemistry realized this limitation (for the Schrödinger equation) as computers started to become more powerful, and accurately simulating small quantum systems was suddenly on the horizon. In particular, Boys [9] advocated for expressing electronic wave functions in terms of linear combinations of Gaussian functions, while Mulliken and Lennard-Jones [58, 45] developed the 'linear combination of atomic orbitals' method to express molecular wavefunctions in terms of atomic ones. By decomposing each function in terms of a set of basis functions, the position dependence of each function could be integrated out and the resulting equations became matrix equations for the unknown expansion coefficients. The problem encountered earlier with real-space methods is then made to vanish and is replaced with solving a matrix equation once per self-consistent iteration [54, 78].

In what is called the spectral method, all position-dependent functions are expanded in terms of a complete set of basis functions $\{f_i(\boldsymbol{r})\}_{i=1}^{\infty}$. For a general function of one spatial variable $g(\boldsymbol{r})$,

we can express it as

$$g(\boldsymbol{r}) = \sum_i g_i f_i(\boldsymbol{r}) \,, \tag{3.29}$$

where g_i are the spectral expansion coefficients; for a general function of two spatial variables $h(\boldsymbol{r}, \boldsymbol{r}')$ this looks like

$$h(\boldsymbol{r}, \boldsymbol{r}') = \sum_{ij} h_{ij} f_i(\boldsymbol{r}) f_j(\boldsymbol{r}') \,, \tag{3.30}$$

where h_{ij} are the spectral expansion coefficients.

We begin by defining the components of the three quantities that will appear throughout the derivation, namely the overlap matrix

$$S_{ij} = \int \mathrm{d}\boldsymbol{r}\; f_i(\boldsymbol{r}) f_j(\boldsymbol{r}) \,, \tag{3.31}$$

the Laplace matrix

$$L_{ij} = \int \mathrm{d}\boldsymbol{r}\; f_i(\boldsymbol{r}) \nabla^2 f_j(\boldsymbol{r}) \,, \tag{3.32}$$

and the Gamma tensor

$$\Gamma_{ijk} = \int \mathrm{d}\boldsymbol{r}\; f_i(\boldsymbol{r}) f_j(\boldsymbol{r}) f_k(\boldsymbol{r}) \,. \tag{3.33}$$

The single-particle partition function for the μ^{th} pair, using eqn. 3.30, can be expressed as

$$Q_\mu(\beta) = \int \mathrm{d}\boldsymbol{r}\; q_\mu(\boldsymbol{r}, \boldsymbol{r}, \beta) = \sum_{ij} \left[q_\mu(\beta)\right]_{ij} \int \mathrm{d}\boldsymbol{r}\; f_i(\boldsymbol{r}) f_j(\boldsymbol{r}) = \sum_{ij} S_{ji} \left[q_\mu(\beta)\right]_{ij} \,. \tag{3.34}$$

The expression for the electron pair density $n_\mu(\boldsymbol{r}, \beta)$ eqn. 3.25 can be spectrally expanded as

$$n_\mu(\boldsymbol{r}, \beta) = \sum_i \left[n_\mu(\beta)\right]_i f_i(\boldsymbol{r}) = \frac{N_\mu}{Q_\mu[w](\beta)} \sum_{ij} \left[q_\mu(\beta)\right]_{ij} f_i(\boldsymbol{r}) f_j(\boldsymbol{r}) \,, \tag{3.35}$$

and after multiplying both sides with $f_k(\boldsymbol{r})$ and then integrating both sides with respect to $\boldsymbol{r}$ we arrive at

$$\sum_i S_{ki} \left[n_\mu(\beta)\right]_i = \frac{N_\mu}{Q_\mu[w](\beta)} \sum_{ij} \left[q_\mu(\beta)\right]_{ij} \Gamma_{kij} \,. \tag{3.36}$$

Equation 3.36 can then be promoted to a matrix equation and the spectral coefficients $\left[n_\mu(\beta)\right]_i$ isolated for by left multiplying each side by the inverse of the overlap matrix. However, one should note that eqn. 3.36 in its present form is more useful for computational purposes, since the algorithm for solving a matrix equation in the Python module SciPy [77] is a wrapped function from the Fortran library LAPACK, which is much faster than matrix multiplying by the inverse over the total number of self-consistent iterations.

The diffusion equation governing the single-particle propagator for the μ^{th} pair, also using eqn. 3.30, can be expressed as

$$\begin{aligned}\frac{\partial q_\mu(\boldsymbol{r},\boldsymbol{r}',s)}{\partial s} &= \sum_{ij}\frac{\partial\left[q_\mu(s)\right]_{ij}}{\partial s} f_i(\boldsymbol{r}) f_j(\boldsymbol{r}') \\ &= \sum_{ij}\left[q_\mu(s)\right]_{ij} f_j(\boldsymbol{r}')\left[\frac{\hbar^2}{2m}\boldsymbol{\nabla}^2 f_i(\boldsymbol{r}) - \sum_k \left[w_\mu\right]_k f_i(\boldsymbol{r}) f_k(\boldsymbol{r})\right], \end{aligned} \tag{3.37}$$

and after multiplying both sides with $f_l(\boldsymbol{r}) f_m(\boldsymbol{r}')$ and then integrating both sides with respect to $\boldsymbol{r}$ and $\boldsymbol{r}'$ we get

$$\sum_{ij}\frac{\partial\left[q_\mu(s)\right]_{ij}}{\partial s} S_{li} S_{mj} = \sum_{ij}\left[q_\mu(s)\right]_{ij} S_{mj}\left[\frac{\hbar^2}{2m}L_{li} - \sum_k [w_\mu]_k \Gamma_{kil}\right] \equiv \sum_{ij}\left[q_\mu(s)\right]_{ij} S_{mj}\left[A_\mu\right]_{il}, \tag{3.38}$$

where the matrix components $\left[A_\mu\right]_{il}$ are defined to be the quantity in the large square brackets. We can again promote eqn. 3.38 to a matrix equation and then left and right multiply both sides by the inverse of the overlap matrix to yield the following matrix differential equation

$$\frac{\mathrm{d}\boldsymbol{q}_\mu(s)}{\mathrm{d}s} = \boldsymbol{S}^{-1}\boldsymbol{A}_\mu\boldsymbol{q}_\mu(s), \tag{3.39}$$

whose components have the simple solution

$$\left[q_\mu(s)\right]_{ij} = \sum_k \left[q_\mu(0)\right]_{ik}\left[e^{(S^{-1}A_\mu)s}\right]_{kj}. \tag{3.40}$$

To determine the components of the matrix of initial conditions $\left[q_\mu(0)\right]_{ij}$ for the spectral expansion of the initial propagator $q_\mu(\boldsymbol{r},\boldsymbol{r}',0) = \delta(\boldsymbol{r}-\boldsymbol{r}')$, we first spectrally expand $q_\mu(\boldsymbol{r},\boldsymbol{r}',0)$ as

$$q_\mu(\boldsymbol{r},\boldsymbol{r}',0) = \delta(\boldsymbol{r}-\boldsymbol{r}') = \sum_{ij}\left[q_\mu(0)\right]_{ij} f_i(\boldsymbol{r}) f_j(\boldsymbol{r}'), \tag{3.41}$$

then multiply both sides by $f_k(\boldsymbol{r})$ and $f_l(\boldsymbol{r}')$, and integrate with respect to $\boldsymbol{r}$ and $\boldsymbol{r}'$ to get

$$\sum_{ij} \left[q_\mu(0)\right]_{ij} \int\int \mathrm{d}\boldsymbol{r}'\mathrm{d}\boldsymbol{r}\, f_i(\boldsymbol{r}) f_j(\boldsymbol{r}') f_k(\boldsymbol{r}) f_l(\boldsymbol{r}') = \sum_{ij} \left[q_\mu(0)\right]_{ij} S_{ik} S_{jl}$$

$$= \int\int \mathrm{d}\boldsymbol{r}'\mathrm{d}\boldsymbol{r}\, f_k(\boldsymbol{r}) f_l(\boldsymbol{r}') \delta(\boldsymbol{r}-\boldsymbol{r}') = \int \mathrm{d}\boldsymbol{r}\, f_k(\boldsymbol{r}) f_l(\boldsymbol{r}) = S_{kl}\,, \tag{3.42}$$

which we can trivially see yields $\left[q_\mu(0)\right]_{ij} = S^{-1}_{ij}$. Now to compute the matrix exponential in eqn. 3.40, we can spectrally decompose $\boldsymbol{S}^{-1}\boldsymbol{A}_\mu$ and take advantage of the matrix exponential property $e^{\boldsymbol{YXY}^{-1}} = \boldsymbol{Y}e^{\boldsymbol{X}}\boldsymbol{Y}^{-1}$ (provided $\boldsymbol{Y}$ is invertible). While we could follow this path in principle, the fact that the product of two Hermitian matrices is not necessarily Hermitian forces us to abandon the Hermiticity of the problem, meaning the computer will be unaware of the fact that $\boldsymbol{S}$ and $\boldsymbol{A}_\mu$ were both Hermitian once upon a time. To preserve the Hermiticity of $\boldsymbol{S}$ and $\boldsymbol{A}_\mu$, we can instead find a spectral decomposition for $\boldsymbol{A}_\mu$ from the generalized eigenvalue problem (where the columns of $\boldsymbol{U}_\mu$ are composed of the eigenvectors $\left[\boldsymbol{v}_\mu\right]_i$ and $\boldsymbol{D}_\mu$ is the matrix composed of the eigenvalues $\left[\lambda_\mu\right]_i$ along its diagonal) [22]

$$\boldsymbol{A_\mu U_\mu} = \boldsymbol{S U_\mu D_\mu} \;\rightarrow\; \boldsymbol{A_\mu} = \boldsymbol{S U_\mu D_\mu U_\mu^{-1}} \;\rightarrow\; \boldsymbol{S^{-1} A_\mu} = \boldsymbol{U_\mu D_\mu U_\mu^{-1}}\,. \tag{3.43}$$

The solution for $\left[q_\mu(s)\right]_{ij}$ then takes the form

$$\left[q_\mu(s)\right]_{ij} = \sum_{kl} S^{-1}_{ik} \left[U_\mu\right]_{kl} e^{\left[\lambda_\mu\right]_l s} \left[U^{-1}_\mu\right]_{jl}\,. \tag{3.44}$$

With the eigenvector matrices from the generalized eigenvalue problem, we can express the identity matrix as $\boldsymbol{I} = \boldsymbol{U}^T_\mu \boldsymbol{S} \boldsymbol{U}_\mu$, leading to an expression for $\boldsymbol{U}^{-1}_\mu = \boldsymbol{U}^T_\mu \boldsymbol{S}$. If we substitute this expression into the propagator matrix expression, then we see that it reduces to

$$\left[q_\mu(s)\right]_{ij} = \sum_{l} \left[U_\mu\right]_{il} e^{\left[\lambda_\mu\right]_l s} \left[U_\mu\right]_{jl}\,. \tag{3.45}$$

Observe also that if we substitute eqn. 3.45 into eqn. 3.34, using the value $s = \beta$, and use the cyclic property of the matrix trace, we can identify the expression for the identity matrix $\boldsymbol{I} = \boldsymbol{U}^T_\mu \boldsymbol{S} \boldsymbol{U}_\mu$, reducing eqn. 3.1 to

$$Q_\mu(\beta) = \sum_i e^{\left[\lambda_\mu\right]_i \beta}\,, \tag{3.46}$$

which bares a resemblance to the quantum partition function in the canonical ensemble. In actuality, eqn. 3.46 is merely a statement of the fact that the trace of an operator equals the

sum of its eigenvalues. Computationally, eqn. 3.46 is enormously more useful than eqn. 3.34, since it does not require eqn. 3.45 to be computed first and can be used to scale down the massive numbers that are characteristic of the summand in eqn. 3.46 for large β values (closer to zero temperature). If the summand in eqn. 3.46 and eqn. 3.46 itself are computed using a computer algebra system (e.g. the Python module SymPy [57]) before computing eqn. 3.45, we then have a numerical recipe for bypassing overflow errors due to large β or $\lambda_{\mu i}$ during the self-consistent iterations. This effectively removes the bottleneck due to large β, allowing us to approach the ground-state electron density more confidently (all calculations were done using values of $\beta \geq 100$ in this work). Alternatively, one could note that the free energy is invariant under the operation $w(\boldsymbol{r}, \beta) \rightarrow w(\boldsymbol{r}, \beta) + w_0$, where w_0 is a constant. This has the effect of shifting each eigenvalue in the spectrum of $\boldsymbol{S^{-1}A_\mu}$ by w_0, which is similar to the previous idea but changes the value of the field [52].

In previous work [72, 78, 79] the eigenfunctions of the Laplacian were chosen to be the basis set partly due to their orthonormality relation, which allows the SCFT equations to be expressed in a concise fashion. While being a convenient choice, the eigenfunctions of the Laplacian have two undesirable features when it comes to atomic systems: they are typically subject to the finite boundary conditions of the Laplacian and their functional form requires many hundreds to thousands of them to achieve adequate resolution. The first feature allows for the introduction of finite-size effects into the computations, which admittedly were present in the original works of Thompson [78, 79] in the form of the Laplacian boundary length being too small, resulting in the free energies being too high. The second feature seriously hinders the scalability of the computations, which is why many in the quantum chemistry community have decided to use Gaussian basis functions for basis function expansions [74]. The move from eigenfunctions of the Laplacian to Gaussians will allow for the robustness necessary to investigate more complicated systems efficiently. In this thesis the systems we concentrate on are isolated atoms, since they represent some of the simplest quantum systems and are thus a good choice for testing the validity of the model.

Normalized Gaussian basis functions in spherical coordinates (r, θ, ϕ) take the form [27]

$$f_i(\boldsymbol{r}) = \mathcal{N}_{pl} Z_l^m(\theta, \phi) r^l e^{-c_{pl} r^2} , \tag{3.47}$$

where the index i represents the tuple of indices (p, l, m), $\mathcal{N}_{pl}$ are the components of the normalization matrix, and $Z_m^l(\theta, \phi)$ are the real spherical harmonics defined in appendix A. Spherical coordinates are chosen as they represent the most natural system to describe the geometry of isolated atoms having only one centre.

Unfortunately, the radial part of these Gaussian basis functions form an over-complete basis, meaning that each basis function is not necessarily orthogonal to another (which introduces a

host of numerical errors that will be discussed later in chapter 4). On top of this, they also do not satisfy the Kato cusp condition at the nuclear centre(s) [37], and introduce arbitrary parameters c_{pl} that must be chosen so as to span the basis space well. However, these deficiencies are more than made up for by the fact that the number of Gaussians required to achieve good resolution is orders of magnitude smaller than for the eigenfunctions of the Laplacian, not to mention that the Gaussians can be defined over all of $\mathbb{R}^3$. A more thorough discussion of the Gaussians will be undertaken in chapter 4.

In the next section we will define the fields at play and give their spectral representations as well.

3.3 Potentials and Fields

The potential $U[n]$ is the only remaining quantity yet to be specified, which will give us the expressions for the fields $w_\mu(\boldsymbol{r},\beta)$ in the system through eqn. 3.26, and finally the free energy eqn. 3.28. In our model, the electron pairs experience four fields in the vicinity of the atomic nucleus: the Coulomb field between the nucleus and the electron pairs $w^{e-n}(\boldsymbol{r},\beta)$, the Coulomb field between the electron pairs $w^{e-e}(\boldsymbol{r},\beta)$, and the exchange-correlation field between electron pairs $w^{xc}(\boldsymbol{r},\beta)$ representing two separate fields. The first of these two fields is the electron self-interaction field $w^{sic}(\boldsymbol{r},\beta)$, which attempts to correct for the interaction of the electron with its own field that is not accounted for in the electron-electron Coulomb field $w^{e-e}(\boldsymbol{r},\beta)$. In this work, a novel self-interaction correction unique to the physical circumstance in this model is used, which is adapted from the Fermi-Amaldi self-interaction correction [6]. The second of these two fields is the Pauli-exclusion field $w^{P}(\boldsymbol{r},\beta)$, which tries to account for the repulsion felt by electrons with the same configuration attempting to occupy the same location, as stipulated by the Pauli-exclusion principle (further discussion will appear in subsection 3.3.2). Note that the two exchange-correlation fields introduced here actually only account for exchange effects and correlations are ignored for the time being.

The potential functional $U[n]$ can then be decomposed as

$$U[n] = U_{e-n}[n] + U_{e-e}[n] + U_{\text{sic}}[n] + U_P[n]\,, \tag{3.48}$$

and the fields are obtained from $U[n]$ as

$$\begin{aligned} w_\mu(\boldsymbol{r},\beta) &= \frac{\delta U_{e-n}[n]}{\delta n_\mu(\boldsymbol{r},\beta)} + \frac{\delta U_{e-e}[n]}{\delta n_\mu(\boldsymbol{r},\beta)} + \frac{\delta U_{\text{sic}}[n]}{\delta n_\mu(\boldsymbol{r},\beta)} + \frac{\delta U_P[n]}{\delta n_\mu(\boldsymbol{r},\beta)} \\ &= w_\mu^{e-n}(\boldsymbol{r},\beta) + w_\mu^{e-e}(\boldsymbol{r},\beta) + w_\mu^{\text{sic}}(\boldsymbol{r},\beta) + w_\mu^{P}(\boldsymbol{r},\beta)\,. \end{aligned} \tag{3.49}$$

3.3.1 Coulombic Fields

The electron-nucleus potential $U_{e-n}[n]$ takes the form

$$U_{e-n}[n] = -\int\int \mathrm{d}\boldsymbol{r}\,\mathrm{d}\boldsymbol{r}'\, n(\boldsymbol{r},\beta)\frac{\rho_{\mathrm{nuc}}(\boldsymbol{r}')}{|\boldsymbol{r}-\boldsymbol{r}'|}\,, \tag{3.50}$$

where $\rho_{\mathrm{nuc}}(\boldsymbol{r})$ is the nuclear density. The electron-nucleus field for each pair $w_\mu^{e-n}(\boldsymbol{r},\beta)$, using the sum of pair densities relation, is then derived from

$$\begin{aligned} w_\mu^{e-n}(\boldsymbol{r},\beta) &= \frac{\delta U_{e-n}[n]}{\delta n_\mu(\boldsymbol{r},\beta)} = -\int\int \mathrm{d}\boldsymbol{r}''\,\mathrm{d}\boldsymbol{r}' \sum_\nu \frac{\delta n_\nu(\boldsymbol{r}'',\beta)}{\delta n_\mu(\boldsymbol{r},\beta)}\frac{\rho_{\mathrm{nuc}}(\boldsymbol{r}')}{|\boldsymbol{r}''-\boldsymbol{r}'|} \\ &= -\int\int \mathrm{d}\boldsymbol{r}''\,\mathrm{d}\boldsymbol{r}' \sum_\nu \delta_{\nu\mu}\delta(\boldsymbol{r}''-\boldsymbol{r})\frac{\rho_{\mathrm{nuc}}(\boldsymbol{r}')}{|\boldsymbol{r}''-\boldsymbol{r}'|} = -\int \mathrm{d}\boldsymbol{r}'\,\frac{\rho_{\mathrm{nuc}}(\boldsymbol{r}')}{|\boldsymbol{r}-\boldsymbol{r}'|}\,. \end{aligned} \tag{3.51}$$

The form of eqn. 3.51 shows that each electron pair feels the same force from the nucleus, since the pair index μ does not appear on the right-hand side. Equation 3.51 gives the field for a generic nuclear density, however in this model, the nucleus is treated as a point particle and the nuclear density then takes the form $\rho_{\mathrm{nuc}}(\boldsymbol{r}) = N\delta(\boldsymbol{r})$. The electron-nucleus field specific to this model is then

$$w_\mu^{e-n}(\boldsymbol{r},\beta) = -N\int \mathrm{d}\boldsymbol{r}'\,\frac{\delta(\boldsymbol{r}')}{|\boldsymbol{r}-\boldsymbol{r}'|} = -\frac{N}{|\boldsymbol{r}|}\,. \tag{3.52}$$

The spectral coefficients from the spectral expansion of eqn. 3.51 are better solved for by applying the Laplacian to both sides and using the fact that the Coulomb potential is the Green's function $G(\boldsymbol{r},\boldsymbol{r}')$ of the Laplacian [78, 32], meaning that it solves the differential equation $4\pi\nabla^2 G(\boldsymbol{r},\boldsymbol{r}') = -\delta(|\boldsymbol{r}-\boldsymbol{r}'|)$:

$$\nabla^2 w_\mu^{e-n}(\boldsymbol{r},\beta) = -\int \mathrm{d}\boldsymbol{r}'\,\rho_{\mathrm{nuc}}(\boldsymbol{r}')\nabla^2\frac{1}{|\boldsymbol{r}-\boldsymbol{r}'|} = \int \mathrm{d}\boldsymbol{r}'\,\rho_{\mathrm{nuc}}(\boldsymbol{r}')4\pi\delta(|\boldsymbol{r}-\boldsymbol{r}'|) = 4\pi\rho_{\mathrm{nuc}}(\boldsymbol{r})\,, \tag{3.53}$$

thereby transforming it into Poisson's equation with source term $-4\pi\rho_{\mathrm{nuc}}(\boldsymbol{r})$. Let us point out one of the immediate benefits of using basis functions defined over all of $\mathbb{R}^3$: the surface term that arises from the Green's function of the Laplacian for finite boundary terms goes to zero in the limit of an infinite boundary[2]. If we now spectrally expand $w_\mu^{e-n}(\boldsymbol{r},\beta)$ and then multiply both sides of eqn. 3.53 by $f_k(\boldsymbol{r})$ and integrate with respect to $\boldsymbol{r}$ we get

$$\sum_i L_{ki}\left[w_\mu^{e-n}\right]_i = 4\pi N\int \mathrm{d}\boldsymbol{r}\delta(\boldsymbol{r})f_k(\boldsymbol{r}) = 4\pi N f_k(\boldsymbol{0})\,, \tag{3.54}$$

[2] A derivation of the surface term can be found in Jackson [32], where the infinite boundary limit can be readily seen.

which is then promoted to a matrix equation and left multiplied by the inverse of the Laplace matrix to isolate for $\left[w_\mu^{e-n}\right]_i$. The form of eqn. 3.54 is again desirable due to considerations made earlier.

The potential due to electron-electron Coulomb-type interactions $U_{e-e}[n]$ is given by

$$U_{e-e}[n] = \frac{1}{2}\int\int \mathrm{d}\boldsymbol{r}\,\mathrm{d}\boldsymbol{r}'\, n(\boldsymbol{r},\beta)\frac{n(\boldsymbol{r}',\beta)}{|\boldsymbol{r}-\boldsymbol{r}'|}\,. \tag{3.55}$$

The electron-electron field for each pair $w_\mu^{e-e}(\boldsymbol{r},\beta)$, using the sum of pair densities relation, is then derived from

$$\begin{aligned} w_\mu^{e-e}(\boldsymbol{r},\beta) &= \frac{\delta U_{e-e}[n]}{\delta n_\mu(\boldsymbol{r},\beta)} = \frac{1}{2}\int\int \mathrm{d}\boldsymbol{r}''\,\mathrm{d}\boldsymbol{r}' \sum_{\nu,\gamma}\left(\frac{\delta n_\nu(\boldsymbol{r}'',\beta)}{\delta n_\mu(\boldsymbol{r},\beta)}\frac{n_\gamma(\boldsymbol{r}',\beta)}{|\boldsymbol{r}''-\boldsymbol{r}'|} + \frac{n_\nu(\boldsymbol{r}'',\beta)}{|\boldsymbol{r}''-\boldsymbol{r}'|}\frac{\delta n_\gamma(\boldsymbol{r}',\beta)}{\delta n_\mu(\boldsymbol{r},\beta)}\right) \\ &= \frac{1}{2}\int\int \mathrm{d}\boldsymbol{r}''\,\mathrm{d}\boldsymbol{r}' \sum_{\nu,\gamma}\left(\delta_{\nu\mu}\delta(\boldsymbol{r}''-\boldsymbol{r})n_\gamma(\boldsymbol{r}',\beta) + n_\nu(\boldsymbol{r}'',\beta)\delta_{\gamma\mu}\delta(\boldsymbol{r}'-\boldsymbol{r})\right)\frac{1}{|\boldsymbol{r}''-\boldsymbol{r}'|} \\ &= \frac{1}{2}\int \mathrm{d}\boldsymbol{r}' \sum_\gamma n_\gamma(\boldsymbol{r}',\beta)\frac{1}{|\boldsymbol{r}-\boldsymbol{r}'|} + \frac{1}{2}\int \mathrm{d}\boldsymbol{r}'' \sum_\nu n_\nu(\boldsymbol{r}'',\beta)\frac{1}{|\boldsymbol{r}''-\boldsymbol{r}|} \\ &= \int \mathrm{d}\boldsymbol{r}'\frac{n(\boldsymbol{r}',\beta)}{|\boldsymbol{r}'-\boldsymbol{r}|}\,, \end{aligned} \tag{3.56}$$

where the arbitrary variable in the second term of the second-last line has been relabelled from $\boldsymbol{r}''$ to $\boldsymbol{r}'$, and the two terms are recognized as being the same. Due to the similarity of $w_\mu^{e-e}(\boldsymbol{r},\beta)$ with $w_\mu^{e-n}(\boldsymbol{r},\beta)$, we need only modify the source term of the resulting Poisson equation to $4\pi n(\boldsymbol{r},\beta)$ and a result with almost identical form follows for $w_\mu^{e-e}(\boldsymbol{r},\beta)$:

$$\sum_i L_{ji}\left[w_\mu^{e-e}\right]_j = -4\pi\sum_i S_{ji}n_i(\beta)\,, \tag{3.57}$$

which is then also promoted to a matrix equation and left multiplied by the inverse of the Laplace matrix to isolate for $\left[w_\mu^{e-e}\right]_i$. It is also clear from eqn. 3.57 that each pair feels the same electron-electron Coulomb field generated by all electrons in the atom. The total field experienced by each pair on the other hand, will not be the same.

3.3.2 Pauli-Exclusion Field

In the derivation of the SCFT equations (eqns. 3.23-3.26), the wavefunction picture was transformed into the density-functional picture, and the notion of particle statistics was outsourced

from the wavefunction to particle "pairs" plus some as yet unknown entity. In OF-DFT, this entity is typically an internal field called the Pauli field, which is used to enforce the Pauli-exclusion principle among Fermions [47]. For a system of Bosons, it is not clear how excluded-volume would model their statistics properly, since there is no restriction on how many Bosons can occupy the same state; more thought would be required to elucidate the exact mechanism. A Pauli-exclusion field $w^P(\boldsymbol{r}, \beta)$ is also introduced into this model, with slight modifications to accommodate the classical space we are working in.

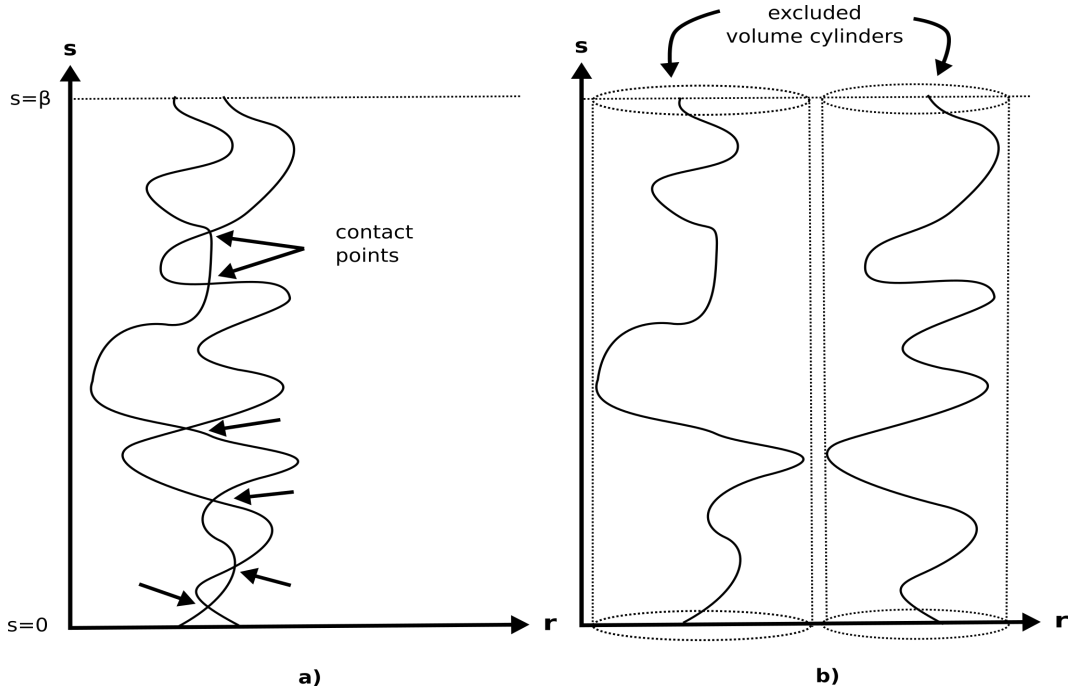

Figure 3.1: A visual representation of two quantum particle trajectories in s parameter space, where the horizontal axes are the spatial coordinates and the vertical axes are the s coordinates. a) Two trajectories very close together sharing many points of excluded-volume contact indicated by the arrows. b) The approximation of the Pauli-exclusion field used in this model, which completely separates the two trajectories so that they have no overlaps for any value of s.

Following Thompson [79], the closest classical analogue of the Pauli-exclusion principle is the notion of excluded-volume, which in polymer SCFT, is often implemented as a Dirac delta energy penalty for overlapping polymer segments. If we are to be truly faithful to the exclusion principle however, the energy penalty should be for overlapping polymer segments from *different* polymer contours representing quantum particles (see figure 3.1a). Now allowing for the possibility of quantum particle spin, the particle "pair" idea introduced earlier manifests itself naturally as the

entities which feel the excluded-volume repulsion[3]. Since the position along the polymer contour is parametrized by a parameter s, the energy penalty due to overlapping polymer contours occurs only for contours at the same value of s. Recall from the quantum-classical correspondence that the parameter s can be interpreted as an imaginary time, so the Pauli-exclusion repulsion is akin to a particle pair feeling the excluded-volume repulsion when at the same place and (imaginary) time as another pair [79]. As a potential, the Pauli-exclusion potential $U_P[n]$ should be expressed along the lines of

$$U_P[n] = \frac{1}{2}\sum_{\substack{\mu,\nu \\ \mu\neq\nu}} \int\int \mathrm{d}\boldsymbol{r}(s)\mathrm{d}\boldsymbol{r}'(s) n_\mu(\boldsymbol{r}(s),\beta)\frac{1}{g_0}\delta(\boldsymbol{r}(s)-\boldsymbol{r}'(s)) n_\nu(\boldsymbol{r}'(s),\beta)\,, \tag{3.58}$$

where g_0 is a constant with the same units as the density of states [79]. Equation 3.58 is difficult to implement in practice, so we approximate it by projecting out the degrees of freedom from the s parameter space, which effectively amounts to imposing the excluded-volume energy penalties for every value of s (see figure 3.1b). The downside to this approximation is that it ignores the inter-contour correlations and will clearly overestimate the excluded-volume felt between the pairs [79]. The approximate Pauli-exclusion potential is then given by

$$U_P[n] = \frac{1}{2g_0}\sum_{\substack{\mu,\nu \\ \mu\neq\nu}} \int\int \mathrm{d}\boldsymbol{r}\mathrm{d}\boldsymbol{r}' n_\mu(\boldsymbol{r},\beta)\delta(\boldsymbol{r}-\boldsymbol{r}')n_\nu(\boldsymbol{r}',\beta) = \frac{1}{2g_0}\sum_{\substack{\mu,\nu \\ \mu\neq\nu}} \int \mathrm{d}\boldsymbol{r} n_\mu(\boldsymbol{r},\beta)n_\nu(\boldsymbol{r},\beta)\,. \tag{3.59}$$

In principle, since the excluded-volume interaction is independent of the specific system under study, g_0 should be a universal constant whose value can be determined by comparing the Pauli potential for a very simplistic system (e.g. a uniform gas with only excluded-volume interactions) to experimental results; see appendix A of Thompson [79] for an explicit calculation. Due to the approximation used in this work, g_0 is taken to be arbitrary, thus we choose its value once for all calculations. The exact value chosen and how it was chosen will be detailed in chapter 4.

The Pauli-exclusion field for each pair $w_\mu^P(\boldsymbol{r},\beta)$ is then derived from

$$\begin{aligned} w_\mu^P(\boldsymbol{r},\beta) &= \frac{\delta U_P[n]}{\delta n_\mu(\boldsymbol{r},\beta)} = \frac{1}{2g_0}\int \mathrm{d}\boldsymbol{r}' \sum_{\substack{\gamma,\nu \\ \gamma\neq\nu}} \left(\frac{\delta n_\nu(\boldsymbol{r}',\beta)}{\delta n_\mu(\boldsymbol{r},\beta)} n_\gamma(\boldsymbol{r}',\beta) + n_\nu(\boldsymbol{r}',\beta)\frac{\delta n_\gamma(\boldsymbol{r}',\beta)}{\delta n_\mu(\boldsymbol{r},\beta)}\right) \\ &= \frac{1}{2g_0}\int \mathrm{d}\boldsymbol{r}' \sum_{\substack{\gamma,\nu \\ \gamma\neq\nu}} \left(\delta_{\nu\mu}\delta(\boldsymbol{r}'-\boldsymbol{r})n_\gamma(\boldsymbol{r}',\beta) + n_\nu(\boldsymbol{r}',\beta)\delta_{\gamma\mu}\delta(\boldsymbol{r}'-\boldsymbol{r})\right) \end{aligned}$$

[3]Note that we are not describing how spin works or manifests itself in the polymer picture, merely that the particle pairs are grouped accordingly.

$$= \frac{1}{2g_0} \sum_{\substack{\gamma \\ \gamma \neq \mu}} n_\gamma(\boldsymbol{r}, \beta) + \frac{1}{2g_0} \sum_{\substack{\nu \\ \mu \neq \nu}} n_\nu(\boldsymbol{r}, \beta) = \frac{1}{g_0} \sum_{\substack{\gamma \\ \gamma \neq \mu}} n_\gamma(\boldsymbol{r}, \beta) \,, \tag{3.60}$$

where the arbitrary parameter in the second term of the last line has been relabelled from ν to γ, and the two terms are recognized as being the same. Due to the form of $w_\mu^P(\boldsymbol{r}, \beta)$, its spectral expansion coefficients $\left[w_\mu^P\right]_i$ will simply be given by

$$\left[w_\mu^P\right]_i = \frac{1}{g_0} \sum_{\substack{\gamma \\ \gamma \neq \mu}} \left[n_\gamma(\beta)\right]_i \,. \tag{3.61}$$

Systematic investigations of the exact Pauli potential functional $U_P[n]$ and its associated field $w^P(\boldsymbol{r}, \beta)$ undertaken by Levy and Ou-Yang [47] have spawned a number of constraints that must be satisfied by it or any approximation thereof. Only some of the constraints will be presented here because a good portion of them are expressed in terms of Kohn-Sham orbitals, which the present orbital-free approach does not have. The relevant constraints are as follows:

$$w^P(\boldsymbol{r}, \beta) \geq 0 \;\;, \;\; \lim_{|\boldsymbol{r}| \to \infty} w^P(\boldsymbol{r}, \beta) = 0 \;\;, \;\; \int \mathrm{d}\boldsymbol{r}\, w^P(\boldsymbol{r}, \beta) n(\boldsymbol{r}, \beta) < \infty \;\;, \;\; w^P(\boldsymbol{r}, \beta) = 0 \;\text{ for }\; N = 2 \;\;,$$

$$w^P[\lambda^3 n](\lambda \boldsymbol{r}, \beta) = \lambda^2 w^P[n](\lambda \boldsymbol{r}, \beta) \,, \tag{3.62}$$

where in the last criterion λ is a scale factor and the functional dependence of the field on the density has been explicitly reinstated. The approximate Pauli-exclusion potential used in this model is therefore provided with some useful criteria to test its scope of validity. The first constraint is satisfied by eqn. 3.60, since the total electron density and the individual pair electron densities obey the same constraint, meaning the total electron density must be larger than each pair density by virtue of eqn. 3.27. The second constraint is also satisfied by eqn. 3.60, since the electron density goes to zero far away from the nucleus. The satisfaction of the first two constraints combined with the properties of the electron density imply that the third constraint is satisfied by eqn. 3.60 as well. The fourth constraint is trivially satisfied because each pair can be comprised of at most 2 electrons and eqn. 3.60 is zero for 1 pair. By inspection, the last constraint clearly does not hold for eqn. 3.60, suggesting that the approximation used in this work does not quite scale correctly with coordinate scaling. This last point is discussed in Thompson [79], where it becomes clearer that the approximate Pauli potential used in this model overestimates the excluded-volume interactions by precisely the amount required to fulfill the last constraint in eqn. 3.62.

3.3.3 Self-Interaction Correction

The electron self-interaction field $w^{\text{sic}}(\boldsymbol{r}, \beta)$ that is used in this work evolved from the well-known Fermi-Amaldi electron self-interaction correction that can be found in some OF-DFT models [6], including the progenitor model to the one used in this work (see [78, 79]). The Fermi-Amaldi electron self-interaction correction is possibly the simplest orbital-free expression that properly accounts for the absence of electron-electron interactions in hydrogen and asymptotically for the electron-electron interactions in the limit of large N; the corresponding field is simply $w^{e-e}(\boldsymbol{r}, \beta)$ multiplied by $-1/N$. The agreement with the binding energy predicted by the Hartree-Fock model for helium is also phenomenally accurate (see chapter 4). For this work, since we take electron pairs as the primitive quantity, it is only appropriate that the Fermi-Amaldi electron self-interaction correction be transformed into

$$w_{\mu}^{\text{sic}}(\boldsymbol{r}, \beta) = -\frac{1}{N_{\mu}} \int \mathrm{d}\boldsymbol{r}' \frac{n_{\mu}(\boldsymbol{r}', \beta)}{|\boldsymbol{r} - \boldsymbol{r}'|}, \tag{3.63}$$

where the corresponding potential $U_{\text{sic}}[n]$ is simply

$$U_{\text{sic}}[n] = -\sum_{\mu} \frac{1}{2N_{\mu}} \int \int \mathrm{d}\boldsymbol{r} \mathrm{d}\boldsymbol{r}' \frac{n_{\mu}(\boldsymbol{r}', \beta) n_{\mu}(\boldsymbol{r}, \beta)}{|\boldsymbol{r} - \boldsymbol{r}'|}, \tag{3.64}$$

with the derivation of $w^{\text{sic}}(\boldsymbol{r}, \beta)$ proceeding in the same way as for $w^{e-e}(\boldsymbol{r}, \beta)$. In this form, eqn. 3.63 directly preserves the desirable qualities of the Fermi-Amaldi electron self-interaction correction for hydrogen and helium. Furthermore, because eqn. 3.63 acts on electron pairs and $0 \leq N_{\mu} \leq 2$, then eqn. 3.63 effectively accounts for the self-interaction of every electron in the atomic system. Those familiar with the Hartree-Fock model will immediately recognize that our model with eqn. 3.63 is *identical* to the situation in the Hartree-Fock model, which models exchange effects exactly. However, because we are approximating the Pauli-exclusion field by projecting out the degrees of freedom from the s parameter space, our model in its current implementation will not reproduce the precise binding energies predicted by Hartree-Fock theory. This is because our Pauli-exclusion field overestimates the excluded-volume felt by the polymer contours in the s-parameter space, hence electron pairs feel too much repulsion between each other and the electron shells will be too distant from their neighbours, raising the free energy substantially in some cases. The Hartree-Fock model on the other hand, is a wavefunction-based model, so the Pauli-exclusion effect is automatically encoded into the wavefunction thanks to the spin-statistics theorem. Additionally, the populating of pairs according to rows of the periodic table that is done in section 4.2 will also prevent complete agreement with Hartree-Fock, since the self-interaction correction will work on shells containing more than 2 electrons. We then stipulate that if the complete expression for the Pauli-exclusion field is realized, and the pairs populated correctly, our model would coincide exactly with Hartree-Fock theory.

Formally, eqn. 3.63 can be seen to be a type of self-interaction correction according to the scheme introduced by Perdew and Zunger [62]. Following the presentation in Parr and Yang [61], but suppressing the spin labels and using the pair densities $n_\mu(\boldsymbol{r})$ in place of the single-particle densities ρ_i corresponding to the i^{th} orbital, the exact electron-electron potential can be broken down into two terms $V_{e-e}[n] = U_{e-e}[n] + U_{xc}[n]$ which must satisfy the requirement that $V_{e-e}[n] = 0$ when $N = 1$. So the necessary requirement to exclude self-interactions can be expressed in terms of the pair densities as $V_{e-e}[n_\mu] = U_{e-e}[n_\mu] + U_{xc}[n_\mu] = 0$. If $U_{xc}[n]$ is further broken down into its exchange $U_x[n]$ and correlation $U_c[n]$ components such that $U_{xc}[n] = U_x[n] + U_c[n]$, then we can re-express the condition as $V_{e-e}[n_\mu] = U_{e-e}[n_\mu] + U_x[n_\mu] = 0$ and $U_c[n_\mu] = 0$, i.e. there are no correlations for single electron systems. Now since we do not have access to the exact exchange-correlation potential $U_{xc}[n]$, it must be approximated by some term which we will denote by $\tilde{U}_{xc}[n]$. The scheme introduced by Perdew and Zunger [62] to account for self-interactions for a given approximation $\tilde{U}_{xc}[n]$ can then be expressed as

$$U_{xc}^{\text{SIC}}[n] = \tilde{U}_{xc}[n] - \sum_\mu \left(U_{e-e}[n_\mu] + \tilde{U}_{xc}[n_\mu] \right) . \tag{3.65}$$

Our exchange-correlation functional with self-interaction correction eqn. 3.64 can then be recovered by setting $\tilde{U}_{xc}[n] = \frac{1}{g_0} \int \mathrm{d}\boldsymbol{r}\, n(\boldsymbol{r},\beta) n(\boldsymbol{r},\beta)$ and substituting $n_\mu(\boldsymbol{r})/N_\mu$ into the argument of U_{e-e} in eqn. 3.65.

The equation for the spectral expansion of eqn. 3.63 is obtained by multiplying the right-hand side of eqn. 3.57 by $-1/N_\mu$, replacing $n_i(\beta)$ with $\left[n_\mu(\beta)\right]_i$ and $\left[w_\mu^{e-e}\right]_j$ with $\left[w_\mu^{\text{sic}}\right]_j$:

$$\sum_i L_{ji} \left[w_\mu^{\text{sic}}\right]_j = \frac{4\pi}{N_\mu} \sum_i S_{ji} \left[n_\mu(\beta)\right]_i , \tag{3.66}$$

and $\left[w_\mu^{\text{sic}}\right]_j$ is isolated for in the same manner.

As was mentioned at the beginning of section 3.3, the combination of the self-interaction correction presented here (eqn. 3.63) and the Pauli-exclusion field (eqn. 3.60) in the previous subsection, represent the exchange-correlation field in this work. The exact exchange-correlation field has been shown to obey a "sum rule" [5] given by the expression

$$\int \mathrm{d}\boldsymbol{r}\, \nabla^2 w_{xc}(\boldsymbol{r}) = 4\pi . \tag{3.67}$$

Equation 3.67 represents another crucial constraint on the exchange-correlation field that any approximation should satisfy, and is thus a good check for the one presented in this work. The Laplacian of the self-interaction correction $w_\mu^{\text{sic}}(\boldsymbol{r},\beta)$ was essentially already shown to give the

result $4\pi n_\mu(\boldsymbol{r},\beta)/N_\mu$, which then integrates simply to 4π. The Laplacian applied to the Pauli-exclusion field $w_\mu^P(\boldsymbol{r},\beta)$, using the spectral expansion in terms of Gaussians and the result eqn. A.10, yields

$$\nabla^2 w_\mu^P(\boldsymbol{r},\beta) = \frac{1}{g_0}\sum_{\substack{\gamma\\ \gamma\neq\mu}}\sum_i \left[n_\gamma(\beta)\right]\nabla^2 f_i(\boldsymbol{r}) = \frac{1}{g_0}\sum_{\substack{\gamma\\ \gamma\neq\mu}}\sum_i \left[n_\gamma(\beta)\right] f_i(\boldsymbol{r})(4c_{pl}^2 r^2 - 2c_{pl}(2l+3))\,, \tag{3.68}$$

which integrates to

$$\begin{aligned}
&\frac{1}{g_0}\sum_{\substack{\gamma\\ \gamma\neq\mu}}\sum_i \left[n_\gamma(\beta)\right]\int \mathrm{d}\boldsymbol{r}\, f_i(\boldsymbol{r})(4c_{pl}^2 r^2 - 2c_{pl}(2l+3)) \\
&\quad = \frac{1}{g_0}\sum_{\substack{\gamma\\ \gamma\neq\mu}}\sum_i \left[n_\gamma(\beta)\right] 4\mathcal{N}_{pl}\left(\frac{\Gamma\left(\frac{l+5}{2}\right)}{c_{pl}^{(l+1)/2}} - \frac{(2l+3)\Gamma\left(\frac{l+3}{2}\right)}{2c_{pl}^{(l+1)/2}}\right)\delta_{l0}\delta_{m0}\sqrt{\pi} = 0\,.
\end{aligned} \tag{3.69}$$

Therefore, the sum of these two integrals is equal to 4π, and the exchange-correlation field felt by each pair satisfies the sum rule[4]. Note however, that the total exchange-correlation field does not satisfy the sum rule, as it yields $4\pi N_p$, where N_p is the total number of pairs. This is hardly surprising as we would not expect 3.67 to be satisfied by our exchange-correlation potential given that eqn. 3.59 is an approximation.

3.4 Free Energy and Spectral SCFT Equations

We now have all the ingredients necessary to derive the spectral expression for the free energy functional eqn. 3.18:

$$\begin{aligned}
F[n,w] = &-\sum_\mu \frac{N_\mu}{\beta}\ln\left(Q_\mu[w](\beta)\right) + \left(\frac{1}{2}-1\right)\sum_\mu \int \mathrm{d}\boldsymbol{r} n_\mu(\boldsymbol{r},\beta)\left(w_\mu^P(\boldsymbol{r},\beta) + w_\mu^{\mathrm{sic}}(\boldsymbol{r},\beta)\right) \\
&+ (1-1)\int \mathrm{d}\boldsymbol{r} n(\boldsymbol{r},\beta) w^{e-n}(\boldsymbol{r},\beta) + \left(\frac{1}{2}-1\right)\int \mathrm{d}\boldsymbol{r} n(\boldsymbol{r},\beta) w^{e-e}(\boldsymbol{r},\beta)
\end{aligned}$$

[4]Equation 3.69 also works out to 0 when using Slater basis functions and is not specific to the Gaussian basis functions.

$$= -\sum_{\mu} \frac{N_\mu}{\beta} \ln\left(Q_\mu[w](\beta)\right) - \frac{1}{2}\int \mathrm{d}\boldsymbol{r}\Bigg(\sum_{\mu} n_\mu(\boldsymbol{r},\beta)\left(w_\mu^P(\boldsymbol{r},\beta) + w_\mu^{\mathrm{sic}}(\boldsymbol{r},\beta)\right) - n(\boldsymbol{r},\beta) w^{e-e}(\boldsymbol{r},\beta)\Bigg)$$

$$= -\sum_{\mu} \frac{N_\mu}{\beta} \ln\left(\sum_i e^{[\lambda_\mu]_i \beta}\right) - \sum_{ij}\frac{1}{2}\Bigg(\sum_{\mu} \left[n_\mu(\beta)\right]_i \left(\left[w_\mu^P(\beta)\right]_j + \left[w_\mu^{\mathrm{sic}}(\beta)\right]_j\right) - n_i(\beta) w_j^{e-e}(\beta)\Bigg) S_{ij}\,. \tag{3.70}$$

The expression for the kinetic energy functional $K[n]$ can also be expressed, using the derivative property of the Dirac delta function, through

$$K[n] = -\sum_j^N \left\langle \frac{\hbar^2}{2m}\nabla_j^2 \right\rangle = -\frac{\hbar^2}{2m}\sum_\mu \sum_j^N \prod_i^N \prod_k^N \frac{1}{Q_\mu[w](\beta)} \int\int \mathrm{d}\boldsymbol{r}_i \mathrm{d}\boldsymbol{r}'_k\, q_\mu(\boldsymbol{r}_i,\boldsymbol{r}'_k,\beta)\langle \boldsymbol{r}'_k|\nabla_j^2|\boldsymbol{r}_i\rangle$$

$$= -\frac{\hbar^2}{2m}\sum_\mu \sum_j^N \prod_i^N \prod_{k\neq j}^{N-1} \frac{1}{Q_\mu[w](\beta)} \int\int \mathrm{d}\boldsymbol{r}_i \mathrm{d}\boldsymbol{r}'_k\, q_\mu(\boldsymbol{r}_i,\boldsymbol{r}'_k,\beta)\delta(\boldsymbol{r}'_k-\boldsymbol{r}_i)\nabla_j^2\delta(\boldsymbol{r}'_j-\boldsymbol{r}_i)$$

$$= -\frac{\hbar^2}{2m}\sum_\mu \sum_j^N \prod_i^N \frac{1}{Q_\mu[w](\beta)} \int \mathrm{d}\boldsymbol{r}_i\, q_\mu(\boldsymbol{r}_i,\boldsymbol{r}_i,\beta) \int \mathrm{d}\boldsymbol{r}'_j q_\mu(\boldsymbol{r}_i,\boldsymbol{r}'_j,\beta)\nabla_j^2\delta(\boldsymbol{r}'_j-\boldsymbol{r}_i)$$

$$= -\frac{\hbar^2}{2m}\sum_\mu \sum_j^N \frac{1}{Q_\mu[w](\beta)} \int\int \mathrm{d}\boldsymbol{r}_j \mathrm{d}\boldsymbol{r}'_j q_\mu(\boldsymbol{r}_j,\boldsymbol{r}'_j,\beta)\nabla_j^2\delta(\boldsymbol{r}'_j-\boldsymbol{r}_j)$$

$$= -\frac{\hbar^2}{2m}\sum_\mu \sum_j^N \frac{1}{Q_\mu[w](\beta)} \int \mathrm{d}\boldsymbol{r}_j \nabla_{\boldsymbol{r}'_j}^2 q_\mu(\boldsymbol{r}_j,\boldsymbol{r}'_j,\beta)\Big|_{\boldsymbol{r}'_j=\boldsymbol{r}_j} \tag{3.71}$$

$$= -\frac{\hbar^2}{2m}\sum_\mu \sum_j^N \sum_{ik} \frac{1}{Q_\mu[w](\beta)} \left[q_\mu(\beta)\right]_{ik} \int \mathrm{d}\boldsymbol{r}_j f_i(\boldsymbol{r}_j)\nabla_j^2 f_k(\boldsymbol{r}_j)$$

$$= -\sum_\mu \sum_{ik} \frac{N\hbar^2}{2mQ_\mu[w](\beta)} \left[q_\mu(\beta)\right]_{ik} L_{ki}\,. \tag{3.72}$$

Together with the above expression for the free energy eqn. 3.70, the full set of spectral SCFT

equations are summarized below for convenience.

$$\frac{\mathrm{d}\left[q_\mu(s)\right]_{ij}}{\mathrm{d}s} = \sum_{kh} S^{-1}_{ik}\left[A_\mu\right]_{kh}\left[q_\mu(s)\right]_{hj} \tag{3.73}$$

$$\left[q_\mu(0)\right]_{ij} = S^{-1}_{ij} \tag{3.74}$$

$$Q_\mu[w](\beta) = \sum_{ij} S_{ji}\left[q_\mu(\beta)\right]_{ij} \tag{3.75}$$

$$\left[n_\mu(\beta)\right]_i = \frac{N_\mu}{Q_\mu[w](\beta)} \sum_{jkq} S^{-1}_{ik}\left[q_\mu(\beta)\right]_{jq}\Gamma_{kqj} \tag{3.76}$$

$$\left[w_\mu(\beta)\right]_i = 4\pi \sum_j L^{-1}_{ij}\left(\sum_k S_{jk}\left(\frac{1}{N_\mu}\left[n_\mu(\beta)\right]_k - \left[n(\beta)\right]_k\right) + N f_j(\mathbf{0})\right) + \frac{1}{g_0}\sum_{\substack{\gamma \\ \gamma\neq\mu}}\left[n_\gamma(\beta)\right]_i \tag{3.77}$$

Chapter 4

Atomic Shell Structure

One of the many objectives of this work, as stated in the first chapter, is to use Gaussian basis functions in the spectral expansions of the SCFT equations 3.73-3.77. The rationale for doing this, is that Gaussian basis sets are much more computationally efficient than eigenfunctions of the Laplacian [27], so the hope is that more complicated systems can be numerically explored and delicate system characteristics such as symmetry-breaking can be extracted with better resolution. Since adding the Gaussian basis functions into the model required significant infrastructure to be constructed, it is more desirable to test simple systems first, which is why isolated atomic systems were chosen to be the subject of the thesis. All known elements were investigated with the model using a spherical-averaging approximation that groups electrons into their known shell configurations for the given atom, ignoring subshells, and uses only the radial part of the basis functions. However, only the results up to the element radon are reported, as we observed the predictable monotonically decreasing trend in accuracy and felt that the increasing importance of relativistic effects meant that the results from our non-relativistic model would not be very useful or insightful. The approximation to the Pauli-exclusion field and the self-interaction correction through spherical-averaging also limits the accuracy we can achieve, which is another reason for stopping at radon. The atomic binding energies are reported and compared with those predicted by Hartree-Fock theory, since we claim that the model is equivalent to this theory and the deviations of Hartree-Fock from the experimental values listed in the NIST database are well-studied, so we forego including them here. The electronic density profiles are given for all elements up to xenon and are further contrasted with Hartree-Fock plots generated by functions obtained from Strand and Bonham [73], up to the element krypton. Xenon is chosen to be the cut-off for the density profiles instead of radon because the effects of the approximations are more pronounced in the density profiles than in the binding energies. The elements up to neon using full angular

Gaussian basis functions were also investigated, enforcing the original pair structure of the model, and the atomic binding energies and contour plots of the electronic density are also shown. The computational methods are detailed before the results are shown to understand how the data were generated.

The model used in this work has been shown to predict molecular bonding [72] and atomic shell structure [78, 79], but has not yet demonstrated that it can produce atomic shell structure without imposing partial shell information to begin with. Furthermore, it remains to be seen if the model will predict the spontaneous symmetry-breaking characteristic of certain atoms. Both of these tests are fundamental to the foundation of the theory, especially in evaluating the suitability of the Pauli-exclusion field to account for particle statistics.

All results are reported using Hartree atomic units, which can be obtained by setting the electron mass (m_e), elementary charge (e), reduced Planck constant ($\hbar$), and inverse Coulomb constant ($4\pi\varepsilon_0$) equal to 1. As a result, distances are measured in atomic units ($1\,a.u. = 5.29177210903(80)\times10^{-11}m$) and energies are measured in Hartrees ($E_h = 4.3597447222071(85)\times 10^{-18}J$).

4.1 Computational Methods

The expressions for the SCFT equations and the free energy (eqns. 3.70-3.77) in terms of the Gaussian basis set are obtained simply by substituting in eqns. A.9,A.12, and A.13 from appendix A. The remarkable utility of the Gaussian basis sets becomes evident again, as they allow everything to be expressed relatively neatly and analytically, lending further credence to the ubiquity of Gaussian basis sets in the quantum chemistry literature. That being said, the time complexity of each expression has increased due to the presence of additional matrix multiplications with the overlap and Laplace matrices as compared to previous work [78, 79, 72]. However, as was mentioned earlier, we need significantly fewer Gaussians to achieve good resolution, so the increase in performance from having less Gaussians more than off-sets this increase in time complexity.

As was also mentioned earlier, we still need to determine a suitable set of Gaussian exponents c_{pl}, so that the basis functions can span the space well. There is a huge body of literature on this topic alone, with a wide variety of approaches [27, 26, 14, 68, 30]. To simplify the process and avoid carrying out endless minimization routines, we choose the exponents according to an "even-tempered"-type scheme similar to reference [14]. Our even-tempered scheme differs from

the standard scheme outlined in Schmidt and Ruedenberg [68], since the exponents are determined by evenly partitioning the logarithmic space between a minimum and maximum exponent of our choosing. This approach can be justified using the encouraging results from references [68, 14] showing the relative linearity of optimized basis exponent sets, and is intuitively easier to visualize. The choice of these minimum and maximum exponents is informed by how accurate the total electron and pair electron numbers are compared to their known values, and changes depending on how many basis functions are included in the set. This last point should be emphasized: because the Gaussians are a non-orthogonal set, it is possible to introduce linear dependence problems by defining the basis set in too narrow a space, spoiling the guarantee of convergence to the infinite basis set limit [68, 14, 71]. The minimum and maximum exponents should also technically depend on the number of electrons in the system, since the inhomogeneities in the electron density due to shell structure could alter the optimal range of exponents or increase the deviation of the sequence from linearity. However, we kept these two values fixed for our calculations and as will be shown in sections 4.2 and 4.3, our results did not show any signs of significant issues due to this factor. Although this scheme lacks the sophistication of the other schemes mentioned above, its simplicity and minimal number of tunable parameters combined with the linear behaviour of optimized basis exponent sets, makes it a good first choice for an initial encounter with Gaussian basis sets. Since much of this work is proof-of-concept, achieving peak performance was not one of the objectives, nor was it our desire to navigate the industrial labyrinth of Gaussian basis exponent optimization.

In this work we almost exclusively used $N_b = 175$ Gaussian basis functions for the spherically-averaged results in section 4.2, since this number provided excellent resolution and converged far enough to the infinite basis set limit as seen in figure 4.2 for example. Note that the reported binding energies in section 4.2 have not been extrapolated in contrast to figure 4.2, since the approximations used in this work limit our accuracy a lot more than the basis set truncation error does. Anything higher than 175 would only add a small amount of resolution and would require a relatively large increase in computation time, which is not a good use of resources considering the resolution is already adequate. The minimum exponent we chose was $c_1 = 10^{-16}$ and the maximum exponent was $c_{175} = 10^{12}$ for the reasons given in the previous paragraph. $N_b = 375$ Gaussian basis functions were used for the angular results in section 4.3 for the same reasons as before, although more basis functions are used in this case because we assigned numbers for each l value of the real spherical harmonics, which in turn have $2l + 1$ types of basis functions (for the number of m values associated to each l). The number 375 comes from assigning 100 basis functions to $l = 0$, 50×3 basis functions to $l = 1$, and 25×5 basis functions to $l = 2$. Increasing l values are assigned smaller numbers of basis functions because the corresponding basis functions become much more diffuse and start to represent smaller portions of the electron density profile. The angular results are also only presented for the first 10 elements, so 100

basis functions for the $l = 0$ portion is more than enough to achieve good resolution. The set of minimum exponents we chose was $c_{1,1,1} = (10^{-14}, 10^{-10}, 10^{-6})$ and the set of maximum exponents was $c_{100,50,25} = (10^{10}, 10^{5}, 10^{3})$, where each entry corresponds to l values in increasing order, respectively.

All of the equations we need to illustrate the self-consistent algorithm used in this work are now present and we give a concise description of it as follows. The number of basis functions along with a suitable minimum and maximum exponent are selected; eqns. A.9, A.12, and A.13 are computed, and an initial guess for the spectral coefficients of the field are chosen[1]. The matrix differential equation for the spectral coefficients of the single-particle propagator 3.38 is then solved for all pairs yielding eqn. 3.40 and then further decomposed into eqn. 3.45 after solving the generalized eigenvalue problem eqn. 3.43. The single-particle partition function eqn. 3.46 is then calculated along with the spectral coefficients for the electron pair densities eqn. 3.36. The spectral coefficients of the fields are then updated self-consistently according to eqns. 3.73-3.77, while the spectral convergence parameter

$$\varepsilon_s \equiv \sqrt{\frac{\sum_{\mu ijk} \left[w_\mu^{\text{new}}(\beta) - w_\mu^{\text{old}}(\beta)\right]_i \left[w_\mu^{\text{new}}(\beta) - w_\mu^{\text{old}}(\beta)\right]_j \left[n_\mu(\beta)\right]_k \Gamma_{ijk}}{\sum_{\mu ijk} \left[w_\mu^{\text{new}}(\beta)\right]_i \left[w_\mu^{\text{new}}(\beta)\right]_j \left[n_\mu(\beta)\right]_k \Gamma_{ijk}}} \tag{4.1}$$

remains above a certain user-defined tolerance value tol. For 175 basis functions, every element was able to satisfy a tolerance of at least 10^{-7}, and for the first 40 elements, a tolerance of at least 10^{-10}. To speed up the convergence of the algorithm, an Anderson acceleration scheme from reference [80] and a simple mixing procedure were used to update the spectral coefficients of the fields. More detail can be found in references [80, 53]. The spectral coefficients of the electron density appearing in eqn. 4.1 are introduced to localize the integration around the atomic nucleus, since Gaussians cover all of $\mathbb{R}^3$, thereby suppressing the field profile far from the nuclear centre and giving a better measure of spectral convergence. Once all quantities have been calculated, the free energy eqn. 3.70 can then be computed along with the density $n(\boldsymbol{r}, \beta)$ and field $w(\boldsymbol{r}, \beta)$ profiles in real space. Due to basis set truncation errors (which will be discussed shortly), it is also desirable to calculate a measure of real-space convergence by numerically integrating the real space version of eqn. 4.1:

$$\varepsilon_r \equiv \sqrt{\frac{\int \mathrm{d}\boldsymbol{r} |w^{\text{new}}(\boldsymbol{r}) - w^{\text{old}}(\boldsymbol{r})|^2 n(\boldsymbol{r})}{\int \mathrm{d}\boldsymbol{r} (w^{\text{new}}(\boldsymbol{r}))^2 n(\boldsymbol{r})}}, \tag{4.2}$$

which was done mainly using the trapezoid rule algorithm. The trapezoid rule is actually one of the most accurate methods to calculate the electron numbers and convergence rates, given

[1]Starting from all zeros for hydrogen and using the previous atomic configuration for subsequent elements.

equal step size and grid point number, because the sharply peaked density profiles that are characteristic of atomic electron densities have their derivatives vanish at the endpoints of the peaks. The contribution of the derivatives to the error of the method is then severely reduced; see reference [34] for a more in-depth discussion. A graphical representation of the self-consistent solution procedure can be seen in figure 4.1. To further reduce the computation time, the basis function specific quantities in appendix A were computed once using a custom algorithm written in Fortran that had been imported to Python, and stored for the duration of the self-consistent iterations.

In addition to the possible sources of numerical error mentioned above, we also note the standard round-off error incurred from finite-precision computer arithmetic using 64-bit floating-point numbers, which will be negligible in this work compared to the other sources of error that are discussed. There is also the potential convergence errors from setting the tolerance level too high or not having the β value high enough to approach the ground-state, although great care was exercised in making sure these issues were minimized by evaluating the program for many different values of these parameters, holding all other parameters fixed, and then deciding on values such that the digits in the atomic binding energies effectively stopped fluctuating. The most significant source of error in this work, and frankly in most research using basis set expansion methods [27, 30], comes from truncating the size of the basis set to a finite number, which is impossible to avoid with a computational implementation. A finite truncation of the basis set means the spectral expansion of a given function is no longer exactly equal to that function, since the basis set can no longer be expected to faithfully span the space completely. In this regard, having less basis functions is actually a detriment to the physical accuracy of our calculations. Thankfully, it has been shown that the convergence of the Gaussians to the infinite basis set limit decays exponentially [71], so one does not have to go very high in basis function number to minimize the truncation error (e.g. figure 4.2). A basis set size of $N_b = 100$ for the smaller elements proved more than enough to account for any errors from finite truncation, which we tested by running the program for many different basis set sizes and then looking at how the digits in the atomic binding energies changed. We deemed that a basis set size of $N_b = 175$ for larger elements was necessary due to fluctuations higher in decimal places, which we again assessed using the previously introduced methodology (see figure 4.2). The confidence we have in the calculated binding energies can be seen in table 4.3 in the next section, which is a reflection of numerical accuracy only because our model is approximate in this work.

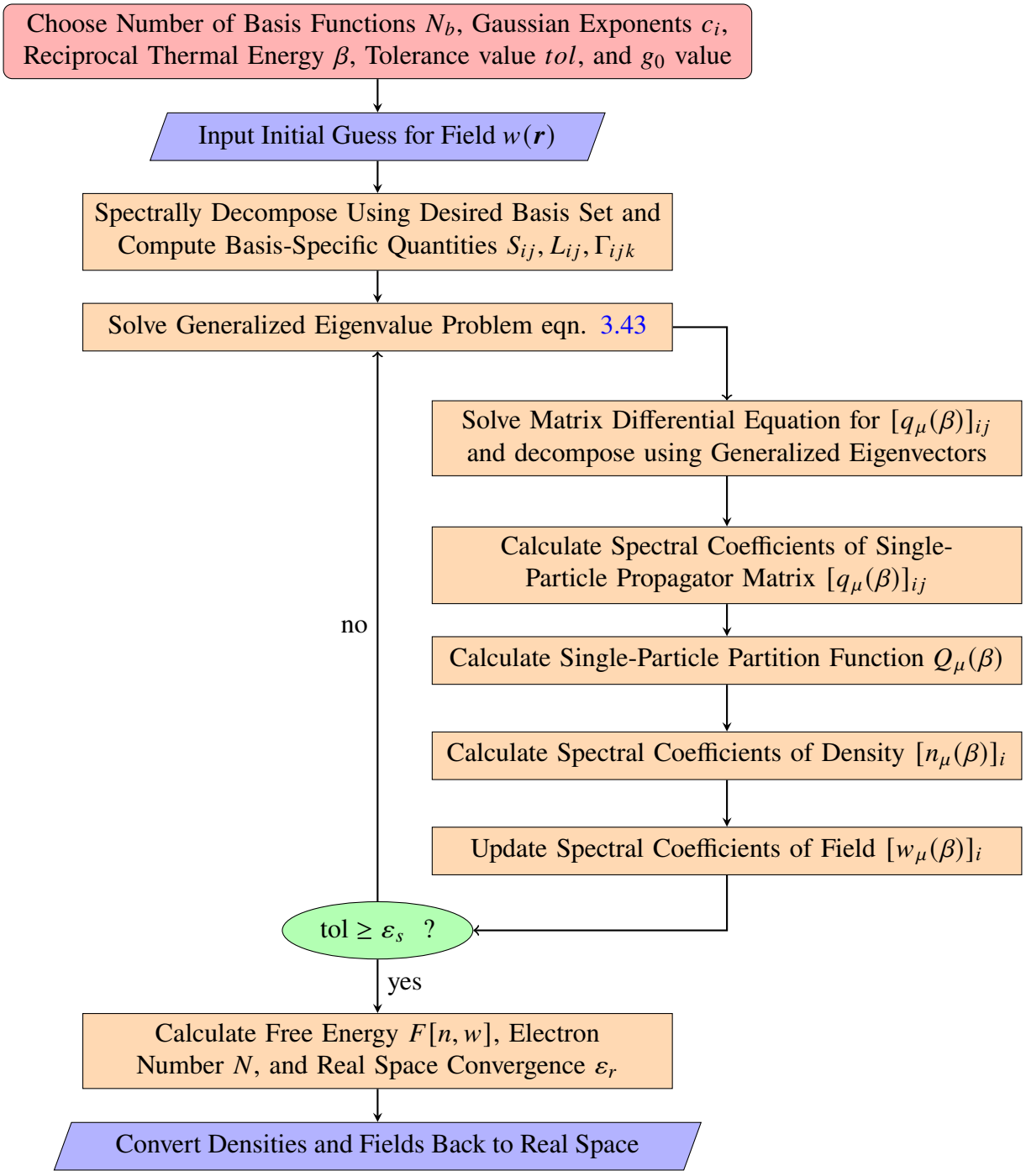

Figure 4.1: A flowchart of the algorithm used to solve the SCFT equations. A red box indicates initialization of parameters, purple boxes represent input and output quantities, beige boxes are calculational steps, and green ovals represent decision steps.

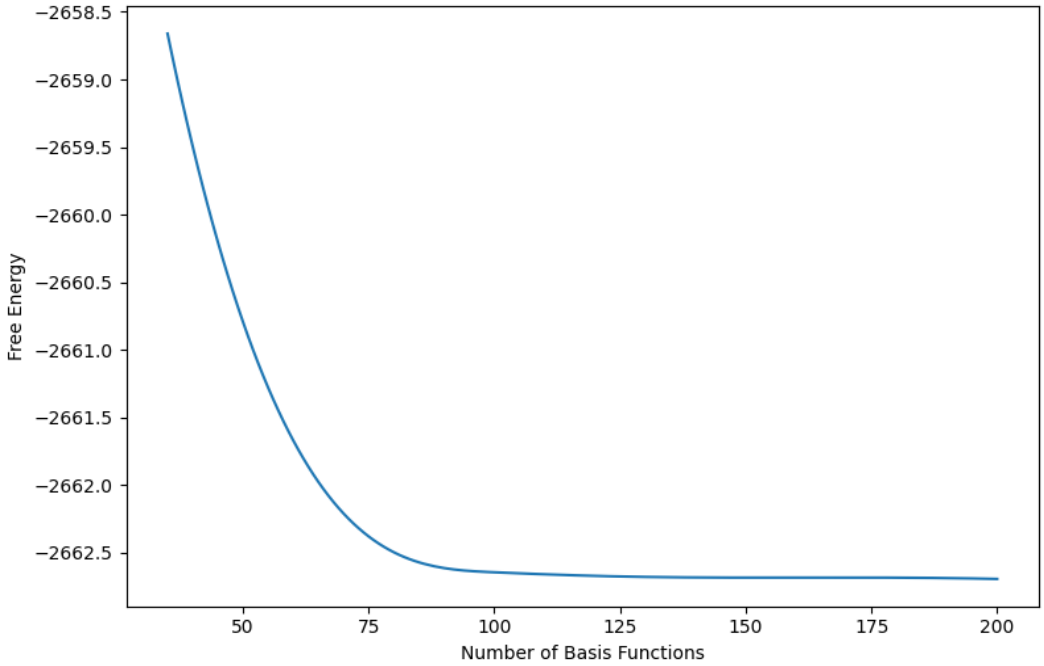

Figure 4.2: The convergence of the free energy for krypton with the number of Gaussian basis functions used. The plot clearly demonstrates the exponential convergence of the Gaussians mentioned in the text. Note that basis function numbers between 50 and 175 have been interpolated using a cubic spline interpolator for expediency, and values outside this range have been extrapolated.

4.2 Spherically-Averaged Atomic Electron Density

As was mentioned at the beginning of this chapter, the first test of the model that was conducted was to compute the atomic binding energies for all elements up to radon and the electronic density profiles for elements up to xenon using a spherical-averaging approximation. The spherical-averaging procedure consists of using only the radial parts of the Gaussian basis set and further populating the pair densities according to the number of electrons appearing in each row of the periodic table. That this approximation is physically reasonable can be justified from the results of reference [15], which shows how small the deviation from spherical symmetry is on the binding energy. This point will be further addressed in the next section when the results from the second test are introduced.

The computed atomic binding energies from this model can be seen in table 4.3, where the values predicted by Hartree-Fock [40] and their percent deviation from our values are listed adjacently. A plot of the percent deviation as a function of atomic number (figure 4.3) is also included to help visualize some of the trends. The data were produced with a value of $g_0 = 0.1$ for the arbitrary constant g_0 associated to the Pauli-exclusion field eqn. 3.60, since this value gives excellent results for argon which lies in the middle of the first 36 elements considered. g_0 can of course be chosen to be another number giving good agreement with Hartree-Fock for a different element, but this choice will have implications for the results in the full angular case in the next section. The value for g_0 was chosen to be a constant rather than a function of the electron number N because we wanted to minimize fine-tuning of parameters in the model. One could conceivably fit a function to the Hartree-Fock data for each N and arbitrarily approach the exact binding energy predicted by Hartree-Fock, but this still would not produce the correct density profiles because the structure of the approximate Pauli-exclusion field differs by more than just a constant factor from the exact field (the dynamics in the s parameter space are quite complicated).

Element	Our Model	Hartree-Fock	% Deviation
H	0.4999999	0.5000000000	0.000002
He	2.861680	2.861679996	0.000000014
Li	7.46841	7.432726931	0.47779
Be	14.70219	14.57302317	0.87856
B	24.90399	24.52906073	1.50550
C	38.40322	37.68861896	1.86078
N	55.52627	54.40093421	2.02667
O	76.59989	74.80939847	2.33746
F	101.95295	99.40934939	2.49488
Ne	131.9173	128.5470981	2.5548
Na	165.524	161.8589116	2.214
Mg	203.344	199.6146364	1.834
Al	245.5075	241.8767073	1.4789
Si	292.1387	288.8543625	1.1242
P	343.359	340.7187810	0.769
S	399.2910	397.5048959	0.4473
Cl	460.056	459.4820724	0.125
Ar	525.7794	526.8175128	0.1974
K	595.966	599.1647868	0.537
Ca	670.922	676.7581859	0.870
Sc	752.040	759.7357180	1.023
Ti	838.613	848.4059970	1.168
V	930.771	942.8843377	1.301
Cr	1030.160	1043.356376	1.281
Mn	1132.36	1149.866252	1.55
Fe	1242.067	1262.443665	1.641
Co	1357.883	1381.414553	1.733
Ni	1479.953	1506.870908	1.819
Cu	1610.74	1638.963742	1.75
Zn	1743.40	1777.848116	1.98
Ga	1881.82	1923.261010	2.20
Ge	2026.08	2075.359734	2.43
As	2176.23	2234.238654	2.67
Se	2332.34	2399.867612	2.90
Br	2494.47	2572.441333	3.13
Kr	2662.68	2752.054977	3.36

Element	Our Model	Hartree-Fock	% Deviation
Rb	2836.6	2938.357454	3.59
Sr	3016.5	3131.545686	3.81
Y	3203.2	3331.684170	4.01
Zr	3396.2	3538.995065	4.20
Nb	3596.5	3753.597728	4.37
Mo	3802.5	3975.549500	4.55
Tc	4014	4204.788737	4.75
Ru	4234.3	4441.539488	4.90
Rh	4460	4685.881704	5.07
Pd	4694	4937.921024	5.21
Ag	4932	5197.698473	5.39
Cd	5176.4	5465.133143	5.58
In	5427.4	5740.169156	5.76
Sn	5685	6022.931695	5.95
Sb	5949	6313.485321	6.13
Te	6219.4	6611.784059	6.31
I	6497	6917.980896	6.49
Xe	6781	7232.138364	6.66
Cs	7071	7553.933658	6.84
Ba	7367	7883.543827	7.01
La	7671	8221.066703	7.17
Ce	7988	8566.872681	7.26
Pr	8318	8921.181028	7.25
Nd	8650	9283.882945	7.33
Pm	8990	9655.098969	7.40
Sm	9338	10034.95255	7.47
Eu	9693.5	10423.54302	7.53
Gd	10049	10820.66121	7.67
Tb	10428	11226.56837	7.65
Dy	10808	11641.45260	7.71
Ho	11196	12065.28980	7.76
Er	11593	12498.15278	7.81
Tm	11997	12940.17440	7.86
Yb	12410	13391.45619	7.90
Lu	12822	13851.80800	8.03
Hf	13242	14321.24981	8.15

Element	Our Model	Hartree-Fock	% Deviation
Ta	13669	14799.81260	8.27
W	14103	15287.54637	8.40
Re	14545	15784.53319	8.52
Os	14996	16290.64860	8.63
Ir	15452	16806.11315	8.76
Pt	15919	17331.06996	8.87
Au	16392	17865.40008	8.99
Hg	16872	18408.99149	9.11
Tl	17358	18961.82482	9.24
Pb	17852	19524.00804	9.36
Bi	18355	20095.58643	9.48
Po	18864	20676.50091	9.60
At	19382	21266.88171	9.72
Rn	19907	21866.77224	9.84

Table 4.3: Atomic binding energies for hydrogen to radon using spherically-averaged electron densities as compared to Hartree-Fock theory [40]. The number of decimal places for the binding energies predicted by our model correspond to the numerical accuracy of our calculations, where the numerical uncertainty is expressed in the last digit.

As is clear from table 4.3 and figure 4.3, the spherically-averaged model does quite well for the first 34 elements, not exceeding a 3% deviation from Hartree-Fock theory. One thing that is immediately obvious is how close the binding energies are for hydrogen and helium, which after plotting their electronic density profiles (figure 4.4 and 4.5), essentially reveals that the only disagreement with Hartree-Fock is due to basis set truncation. The exact agreement with the analytically known solution for the hydrogen atom is an important first case because the hydrogen atom is the only atom that can be solved analytically and expressed in closed form, which gives a lower bound on our confidence of the model. The exact agreement with helium is another important step as hydrogen and helium are the only atoms whose electrons experience no repulsive forces from Pauli-exclusion effects in their ground state, allowing for the fitness of the self-interaction correction to be assessed independently from the approximate Pauli-exclusion field used in the model. The two elements are also not affected by the spherical-averaging approximation, since they have spherical ground-states and equivalent pair to shell configurations. Looking further at the results for helium after the introduction of lithium (figure 4.6), further evidence emerges that indicates the approximation to the Pauli-exclusion field used in this work really is the only physical barrier preventing the complete agreement with Hartree-Fock, but we

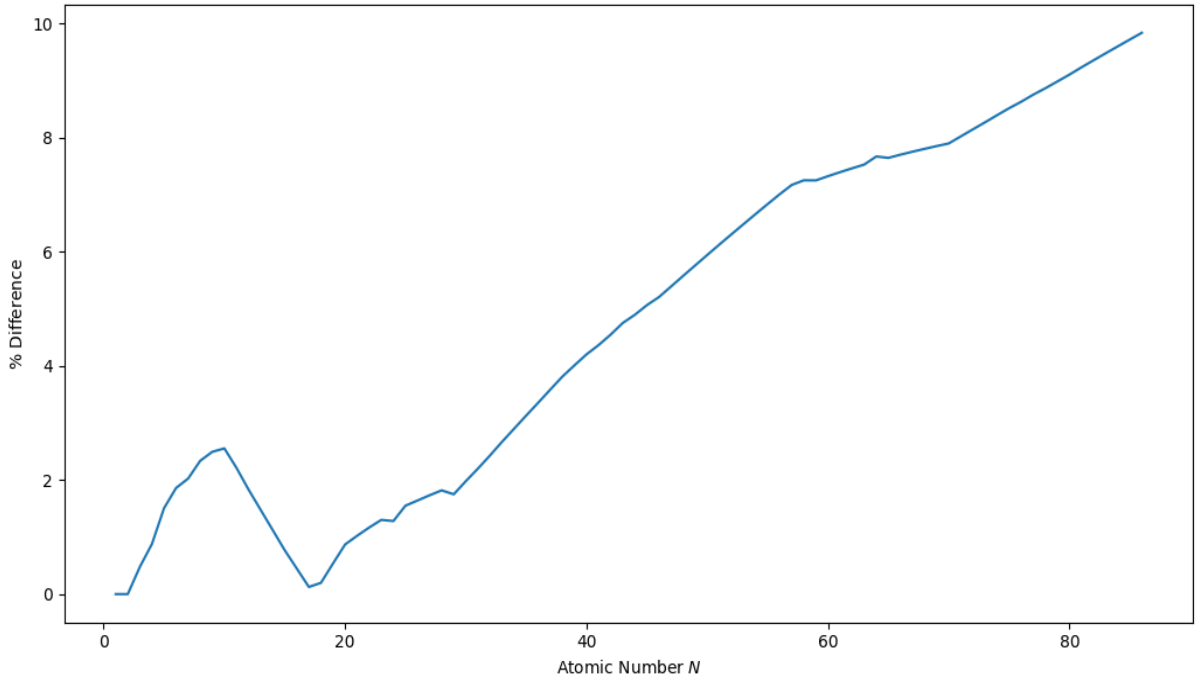

Figure 4.3: The percent difference between the binding energies predicted by Hartree-Fock and our model for elements hydrogen to radon. The general trends in this plot give some indication of how the true Pauli-exclusion field should behave.

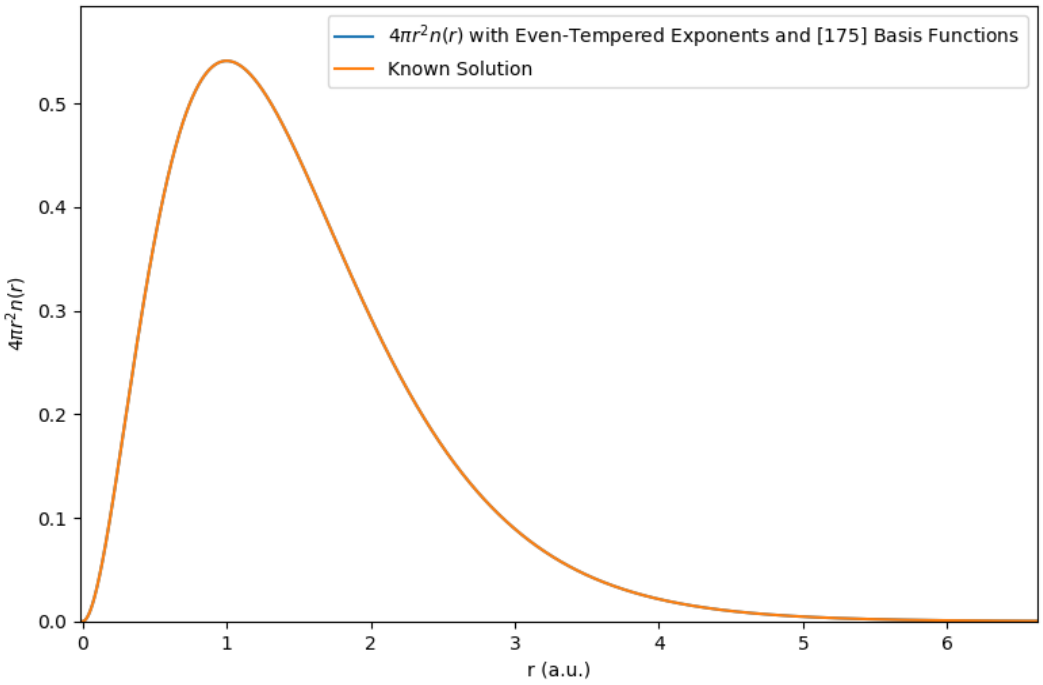

Figure 4.4: The spherically-averaged electron density for hydrogen compared with the known analytic solution.

won't truly know until the exact Pauli-exclusion field is properly implemented (see chapter 5).

Some other interesting trends to notice are in the shape of the percent deviation plot (figure 4.3), which has a distinctive 'hump' feature going through the first 18 elements, and then a roughly monotonically increasing line for the rest of the elements up to radon. The latter trend is hardly surprising, as the effects of the incorrect approximate Pauli-exclusion field start to compound for larger and more complicated configurations of electrons. The 'hump' feature also makes sense because the local minimum coincides with the element where the chosen value of g_0 gives good agreement with Hartree-Fock theory. Argon is thus of particular significance because it marks the point where the atomic systems stop being over-bound and start becoming under-bound, which is a consequence of the approximate Pauli-exclusion field and the specific value chosen for g_0. This also reveals an aspect of the exact Pauli-exclusion field, since we see that the agreement with Hartree-Fock for the binding energies places the value of g_0 much higher for smaller elements, which then rapidly decreases to 0.1 for the first 18 elements, and then slowly decreases for the rest of the periodic table. This behaviour can be further demonstrated by looking at figures 4.6-4.11, which show how the approximate Pauli-exclusion field overestimates the excluded-volume interactions, resulting in too much separation between peaks and deeper peak-to-peak valleys as

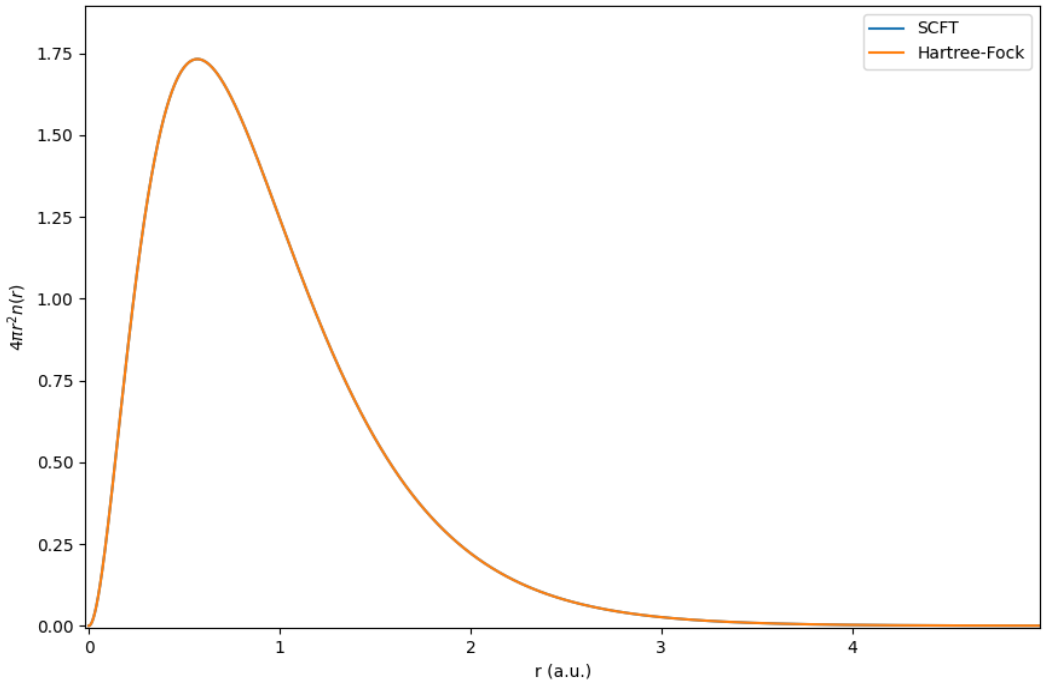

Figure 4.5: The spherically-averaged electron density for helium compared with the one predicted by Hartree-Fock theory.

compared with the density profiles predicted by Hartree-Fock (the plots on the bottom of figures 4.6-4.11). It is important to note however, that the peak locations predicted by our model are approximately in the same location as the peaks predicted by Hartree-Fock, with both models giving the correct area under each curve (the electron number). As an aside, we tried using other functional forms for the self-interaction correction, including the Fukui function from Ayers and Levy [4]: the same behaviour just described was exhibited by all of them, pointing to the Pauli-exclusion field as the culprit.

4.3 Full Angular Atomic Electron Density

The spherical-averaging approximation used in the previous section was useful to see how well the model could replicate the trends in atomic systems for a larger range of elements, most importantly the shell structure, but we know that some elements prefer to break spherical-symmetry in their ground state and so this approximation is not suitable to investigate whether the model will predict spherical-symmetry breaking or not. Additionally, we would like to restore the original pair structure of the model and see how well it does at spontaneously predicting shell structure.

The atomic binding energies are shown in table 4.5. One crucial difference with the spherically-averaged case can be spotted immediately by looking at the percent difference with Hartree-Fock: The model with pair structure and angular dependence is much closer to Hartree-Fock for the first 6 elements, but rapidly becomes worse due to the presence of too much Pauli-exclusion repulsion felt between electron pairs. In the angular case, the shell configurations are also not prebuilt into the code, so the overabundance of the Pauli-exclusion force causes the pairs after carbon to spread too far apart and not conspire to form the proper shell structure observed in nature. However, the observed shell structure still somewhat resembles what we expect (figures 4.15-4.20)[2] and more importantly, we do see spontaneous symmetry-breaking! Unfortunately, symmetry-breaking is first predicted to occur at carbon as opposed to boron, and the shapes of the pair densities don't seem to match our expectations (this second point will be addressed shortly). The magnitude of the symmetry-breaking effect can also be modified through the value of g_0 (i.e. a smaller value produces more noticeable deviations). Although nature predicts symmetry-breaking to occur at boron, this doesn't necessarily mean the theory is flawed; the issue may lie in the approximation used for the Pauli-exclusion field, in which case the exact field would need to be implemented to sufficiently test this. The fact that spontaneous symmetry-breaking does occur, and only one element over from where it is supposed to be, is a very encouraging result nevertheless.

[2]The density contour plots of the first four elements are not shown as they are all spherical and have identical pair to shell structure, so they can essentially be encapsulated by figure 4.6.

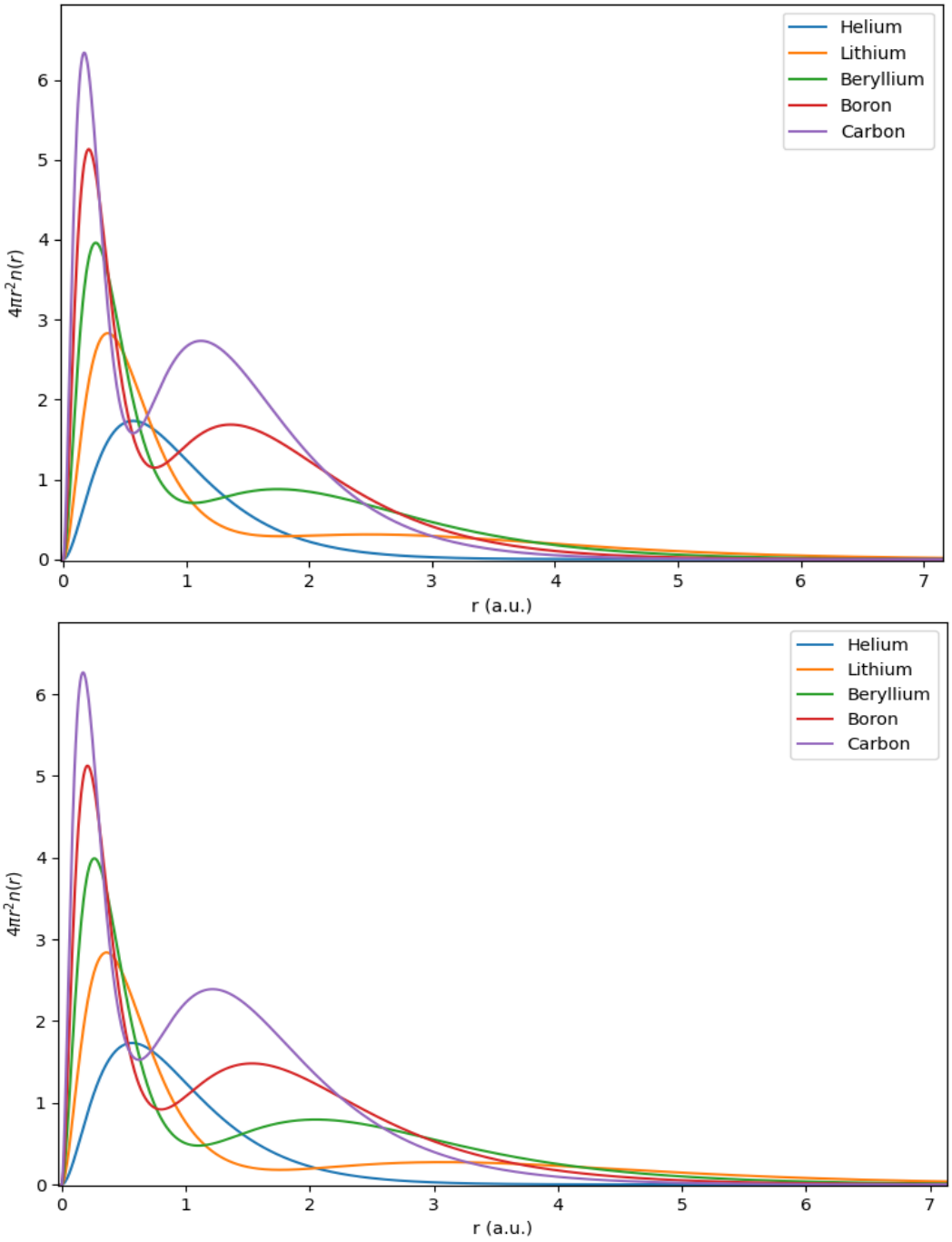

Figure 4.6: The spherically-averaged electron densities for helium to carbon. The top plot shows the densities predicted by our model while the bottom plot shows the densities predicted by Hartree-Fock for comparison.

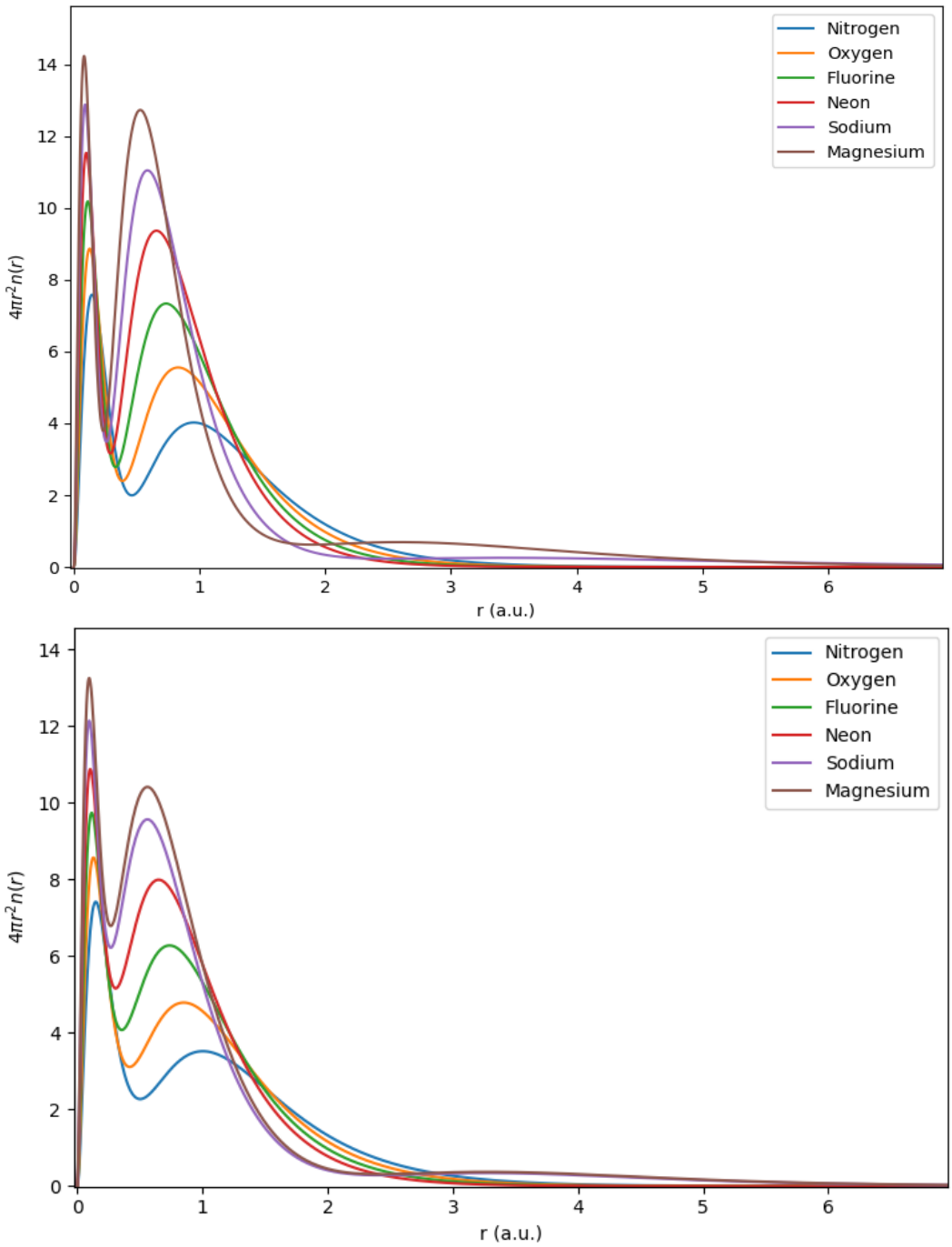

Figure 4.7: The spherically-averaged electron densities for nitrogen to magnesium. The top plot shows the densities predicted by our model while the bottom plot shows the densities predicted by Hartree-Fock for comparison.

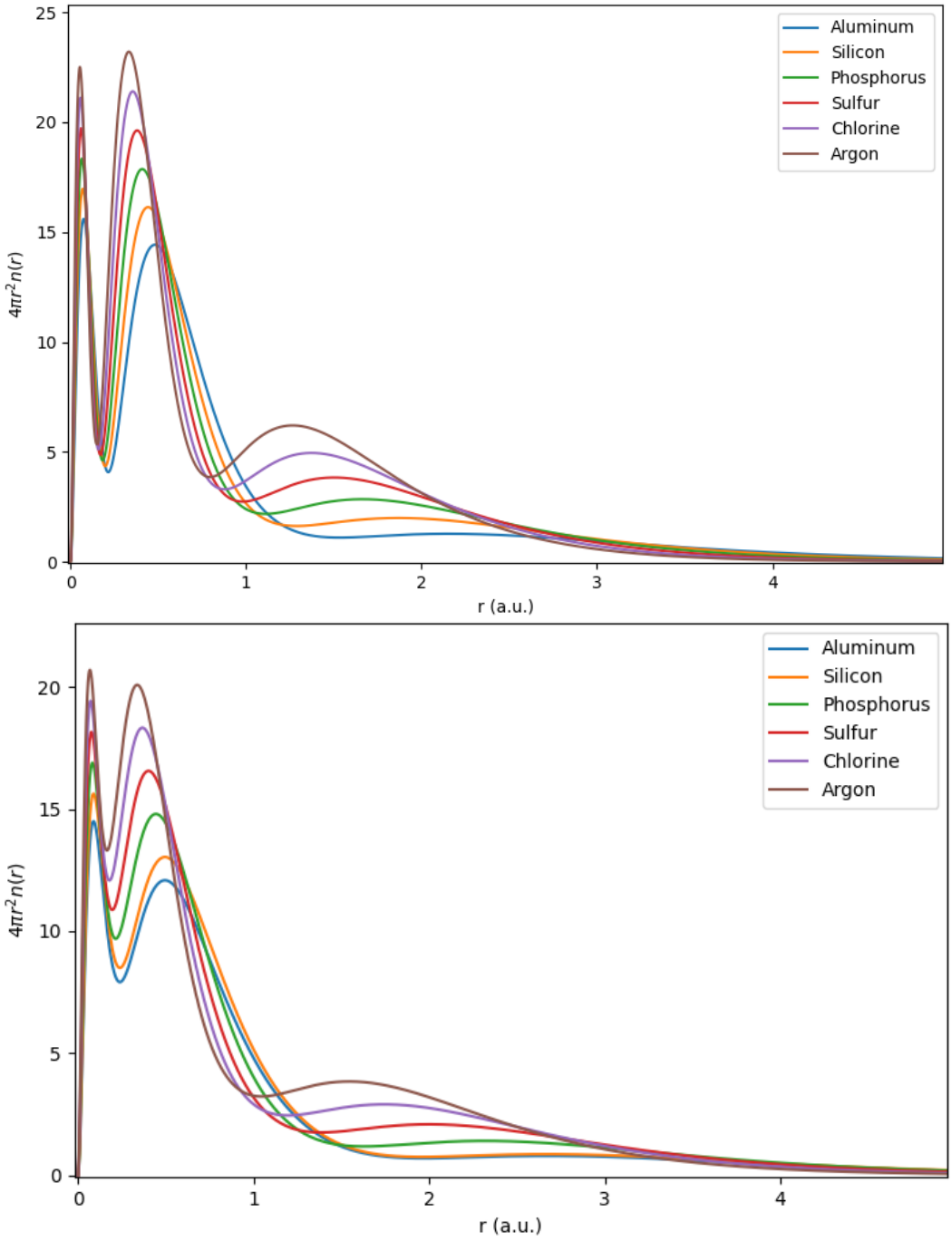

Figure 4.8: The spherically-averaged electron densities for aluminum to argon. The top plot shows the densities predicted by our model while the bottom plot shows the densities predicted by Hartree-Fock for comparison.

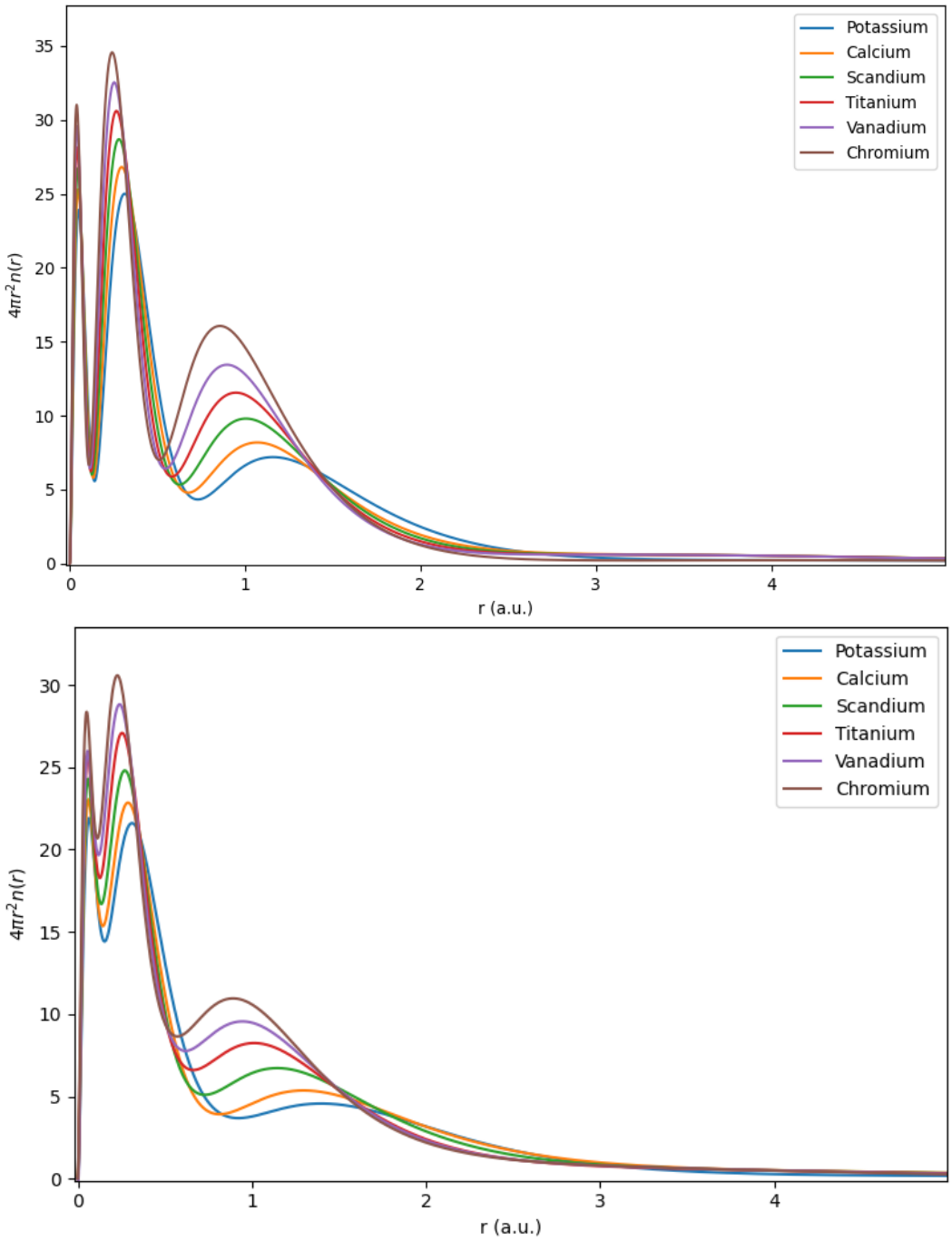

Figure 4.9: The spherically-averaged electron densities for potassium to chromium. The top plot shows the densities predicted by our model while the bottom plot shows the densities predicted by Hartree-Fock for comparison.

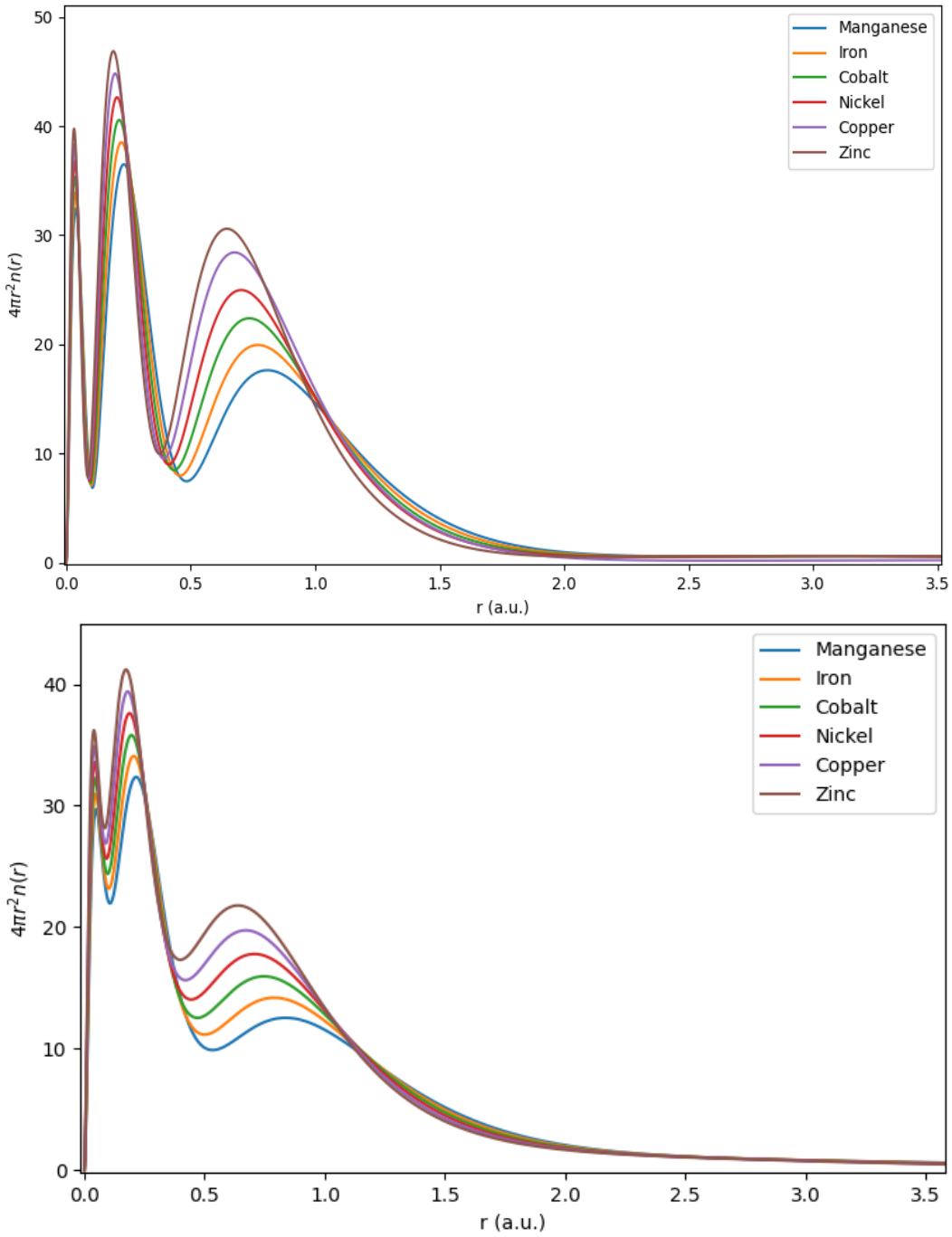

Figure 4.10: The spherically-averaged electron densities for manganese to zinc. The top plot shows the densities predicted by our model while the bottom plot shows the densities predicted by Hartree-Fock for comparison.

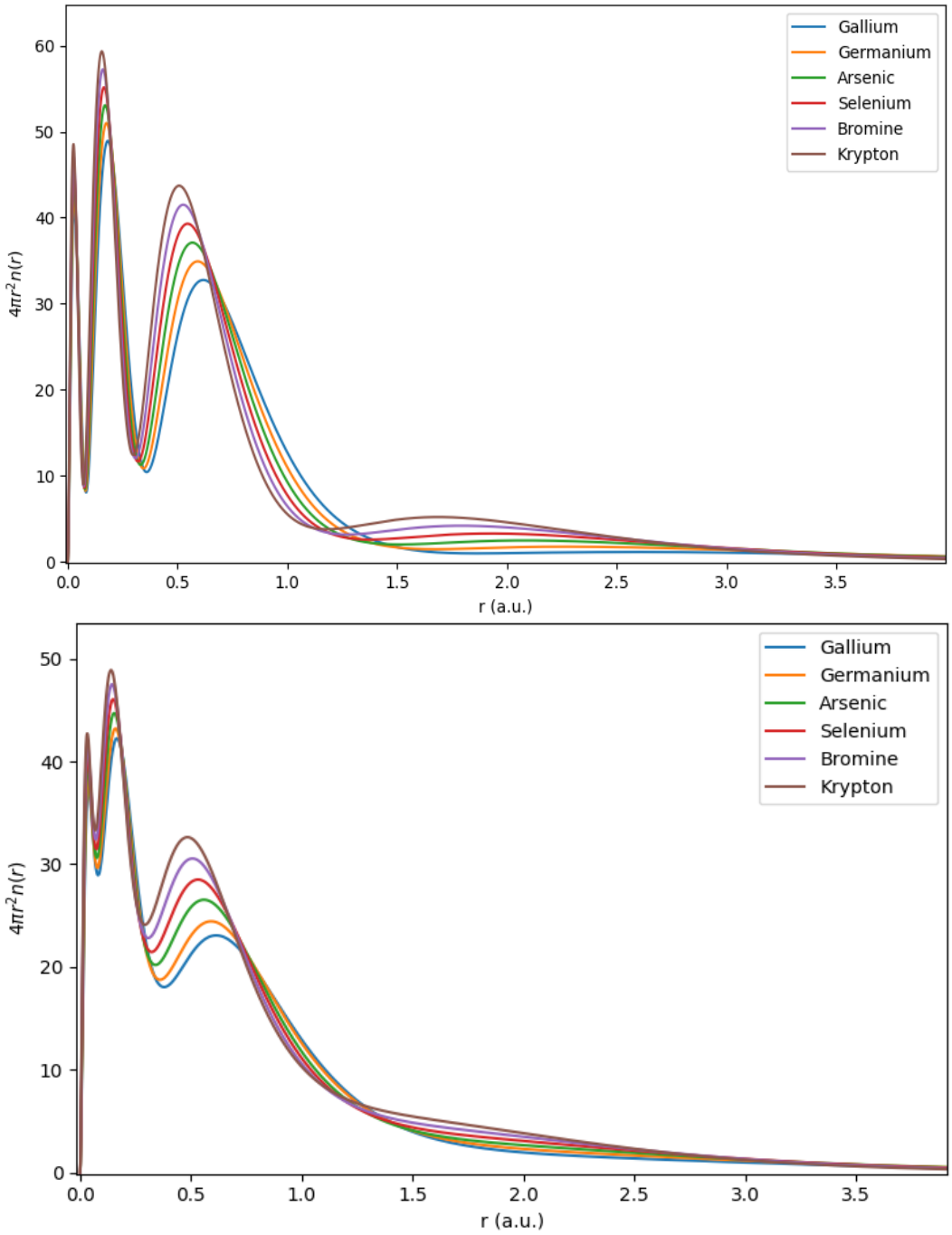

Figure 4.11: The spherically-averaged electron densities for gallium to krypton. The top plot shows the densities predicted by our model while the bottom plot shows the densities predicted by Hartree-Fock for comparison.

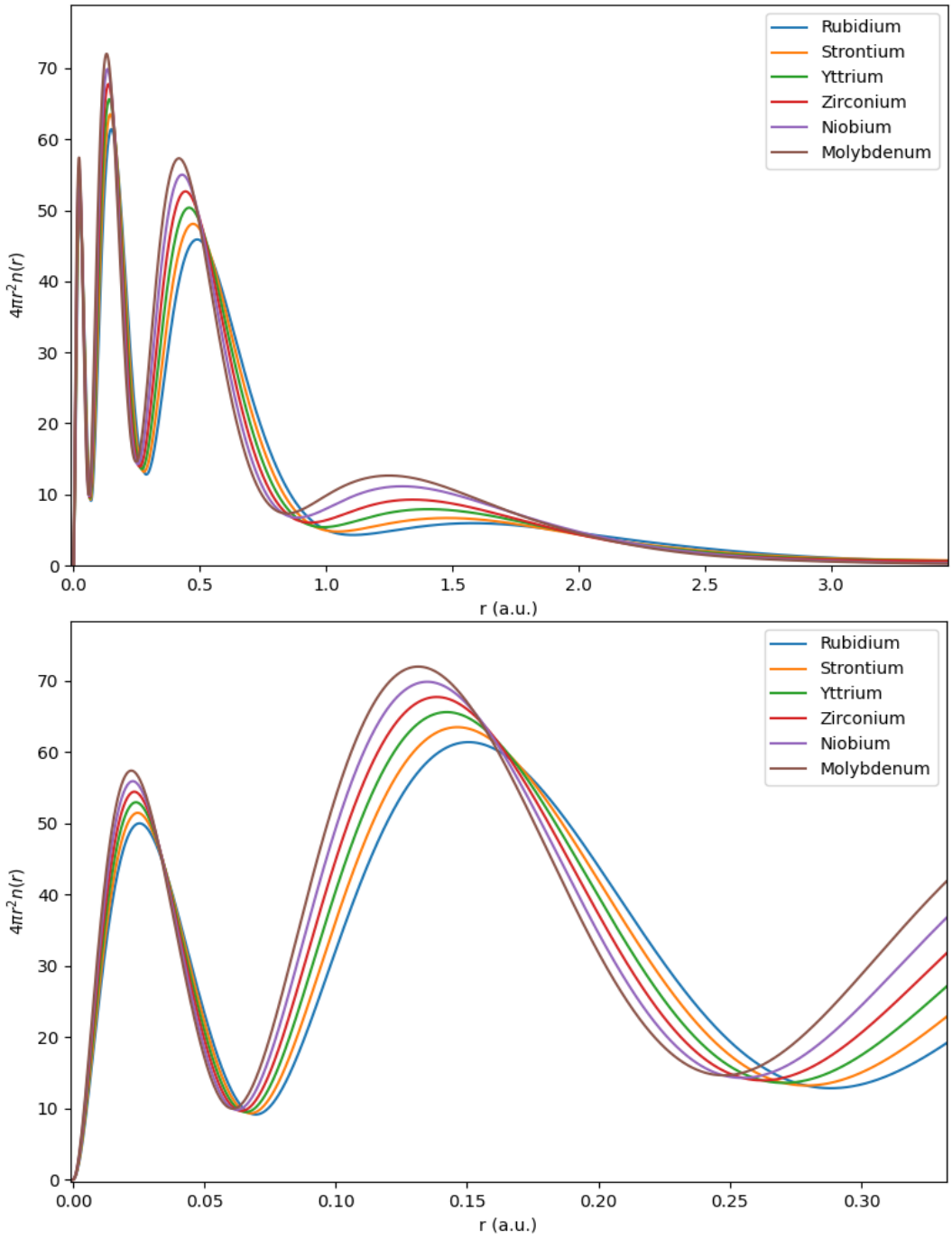

Figure 4.12: The spherically-averaged electron densities for rubidium to molybdenum. The top plot shows the densities predicted by our model and the bottom is a magnification of the inner peaks, since the individual curves of those peaks are difficult to distinguish in the complete profile.

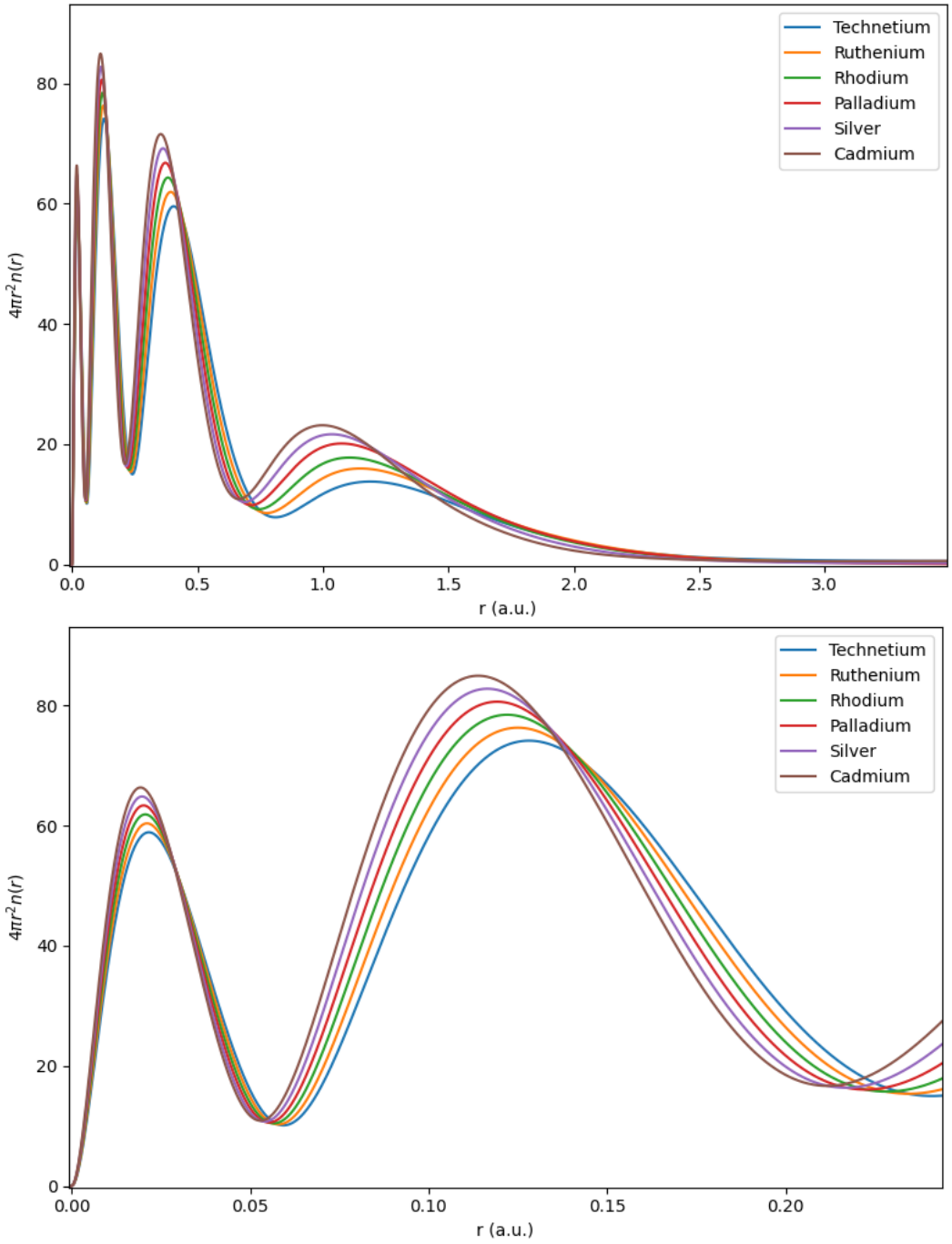

Figure 4.13: The spherically-averaged electron densities for technetium to cadmium. The top plot shows the densities predicted by our model and the bottom is a magnification of the inner peaks, since the individual curves of those peaks are difficult to distinguish in the complete profile.

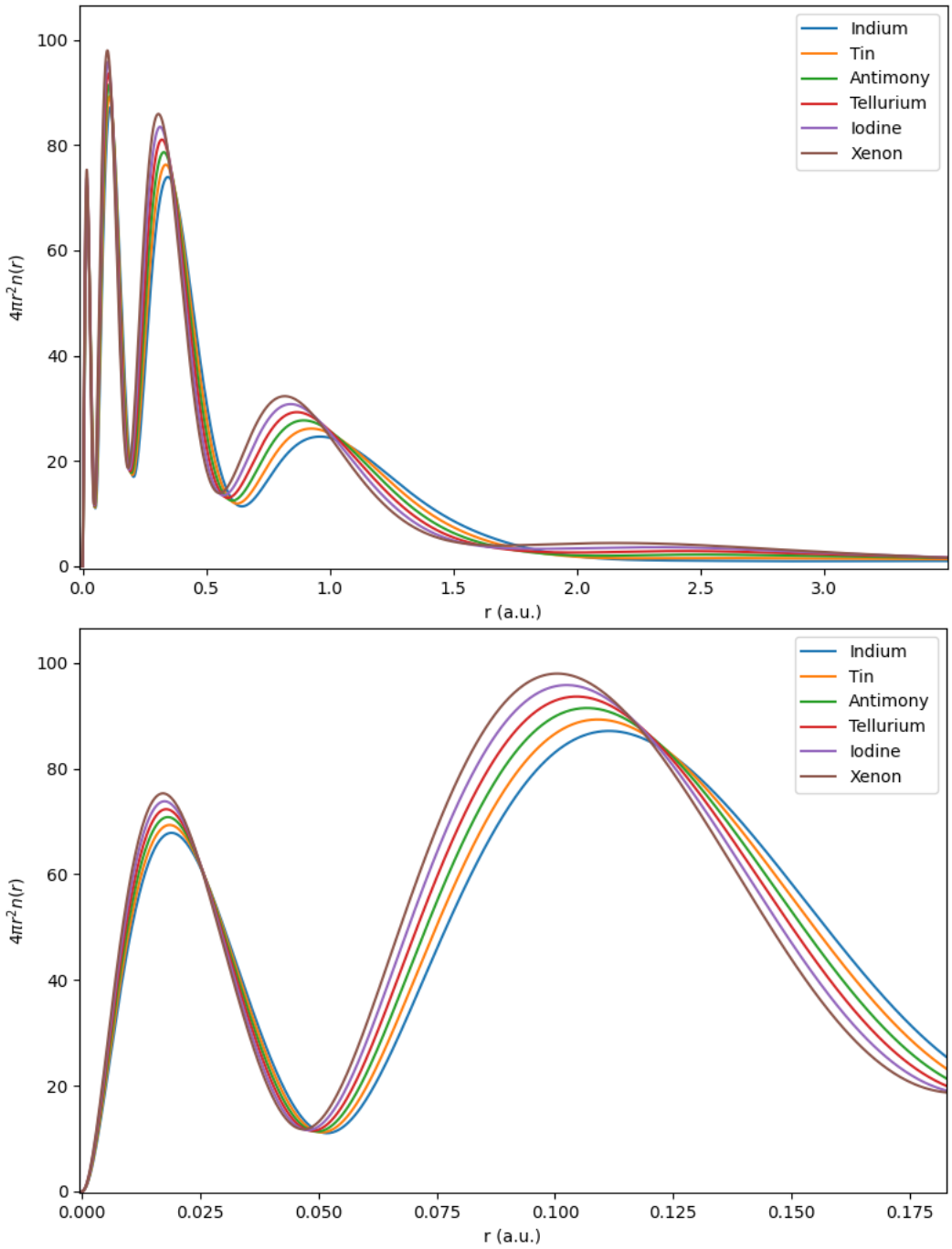

Figure 4.14: The spherically-averaged electron densities for indium to xenon. The top plot shows the densities predicted by our model and the bottom is a magnification of the inner peaks, since the individual curves of those peaks are difficult to distinguish in the complete profile.

Element	Our Model	Hartree-Fock	% Deviation
H	0.4999999	0.5000000000	0.000002
He	2.861679	2.861679996	0.000000014
Li	7.46842	7.432726931	0.47792
Be	14.70219	14.57302317	0.87856
B	24.66954	24.52906073	0.56944
C	37.567740	37.68861896	0.321764
N	53.40706	54.40093421	1.86094
O	72.3335	74.80939847	3.4229
F	94.3264	99.40934939	5.3887
Ne	119.5084	128.5470981	7.5633

Table 4.4: Atomic binding energies for hydrogen to neon using spherically-averaged basis sets and populating the pairs according to their original definition. The number of decimal places for the binding energies predicted by our model correspond to the numerical accuracy of our calculations, where the numerical uncertainty is expressed in the last digit.

Element	Our Model	Hartree-Fock	% Deviation
H	0.4999999	0.5000000000	0.000002
He	2.861679	2.861679996	0.000000014
Li	7.46842	7.432726931	0.47792
Be	14.70219	14.57302317	0.87856
B	24.66954	24.52906073	0.56944
C	37.676473	37.68861896	0.032238
N	53.71061	54.40093421	1.28527
O	72.9246	74.80939847	2.5846
F	95.3842	99.40934939	4.2199
Ne	121.2435	128.5470981	6.0239

Table 4.5: Atomic binding energies for hydrogen to neon using full angular basis sets and populating the pairs according to their original definition. The number of decimal places for the binding energies predicted by our model correspond to the numerical accuracy of our calculations, where the numerical uncertainty is expressed in the last digit.

The differences in the binding energies between the non-angular and angular runs are essentially non-existent for the first 4 elements, as they should be since these elements are known to have

spherical ground-state distributions and minimal Pauli-exclusion repulsion (tables 4.4 and 4.5, respectively). The lack of a noticeable binding energy difference for boron is attributed to the approximate Pauli potential used in this work, which predicts symmetry-breaking to occur at carbon instead of boron, as was previously mentioned. Carbon is the first element where any difference in the binding energy between the angular and non-angular cases can be seen: the percent difference with the prediction from Hartree-Fock theory in the angular case is approximately an order of magnitude smaller than in the non-angular case. However, it should be expected based on the other trends in tables 4.4 and 4.5, that part of the accuracy of this result is due to the cancellation of certain errors and not of a genuine agreement with Hartree-Fock theory. The rest of the elements from tables 4.4 and 4.5 display very minor changes in the binding energy, which agrees nicely with the results of Chowdhury and Perdew [15], who also report that the effect of symmetry-breaking has a small impact on the binding energy. These results suggest that the spherical-averaging approximation in section 4.2 actually performs quite well in most scenarios and that it would be physically reasonable to use it provided the aim isn't to investigate delicate features such as symmetry-breaking.

Having a look at figures 4.15-4.20, we can see that the pair densities beyond the first pair don't match up with the orbital picture we get from other DFT approaches. Once more, the non-spherical pair densities only resemble half of a lobe in contrast to the double lobe picture many are familiar with. However, let us point out that pair densities do not correspond to the squared modulus of individual orbitals from KS-DFT, rather, they correspond to sums of squared moduli of orbitals. To see this, recall that the effective Hamiltonian H_μ^{eff} appearing in the single-particle diffusion equation eqn. 3.16 is the same Hamiltonian that appears in the Kohn-Sham equation, therefore the orbitals $\phi_{\mu i}(\boldsymbol{r})$ from this Hamiltonian can be used as a basis set and solve for the single-particle propagator. The orbitals are defined as

$$H_\mu^{\text{eff}}\phi_{\mu i}(\boldsymbol{r}) = \left[\varepsilon_\mu\right]_i \phi_{\mu i}(\boldsymbol{r}) \quad \text{where} \quad \int \mathrm{d}\boldsymbol{r}\, \phi_{\mu i}(\boldsymbol{r})\phi_{\mu j}(\boldsymbol{r}) = \delta_{ij}\,, \tag{4.3}$$

so the single-particle propagator is

$$q_\mu(\boldsymbol{r}, \boldsymbol{r}', s) = \sum_{ij} \left[q_\mu(s)\right]_{ij} \phi_{\mu i}(\boldsymbol{r})\phi_{\mu j}(\boldsymbol{r}')\,. \tag{4.4}$$

The diffusion equation is then

$$\frac{\partial q_\mu(\boldsymbol{r}, \boldsymbol{r}', s)}{\partial s} = \sum_{ij} \frac{\partial \left[q_\mu(s)\right]_{ij}}{\partial s} \phi_{\mu i}(\boldsymbol{r})\phi_{\mu j}(\boldsymbol{r}') = -H_\mu^{\text{eff}} q_\mu(\boldsymbol{r}, \boldsymbol{r}', s)$$

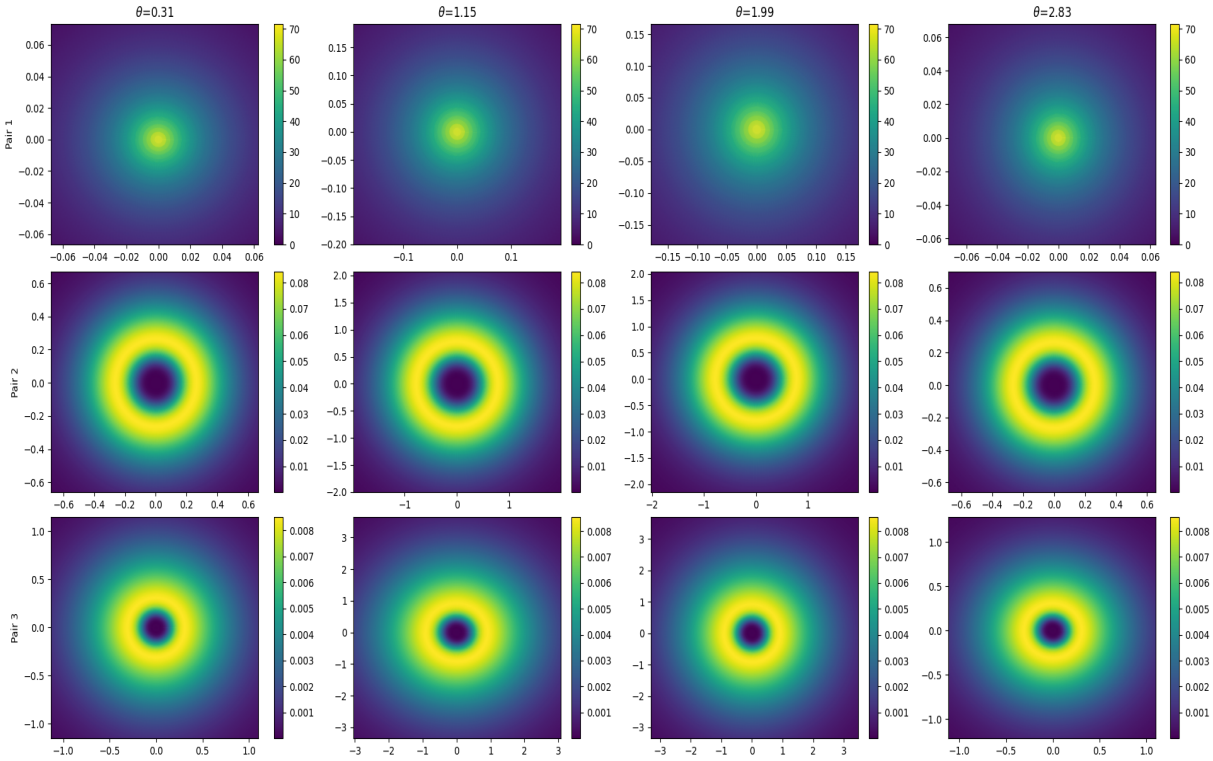

Figure 4.15: Boron angular electron pair density contour plots for fixed values of θ. The axes correspond to the y and x Cartesian coordinates respectively, and the colour bar indicates the magnitude of the density.

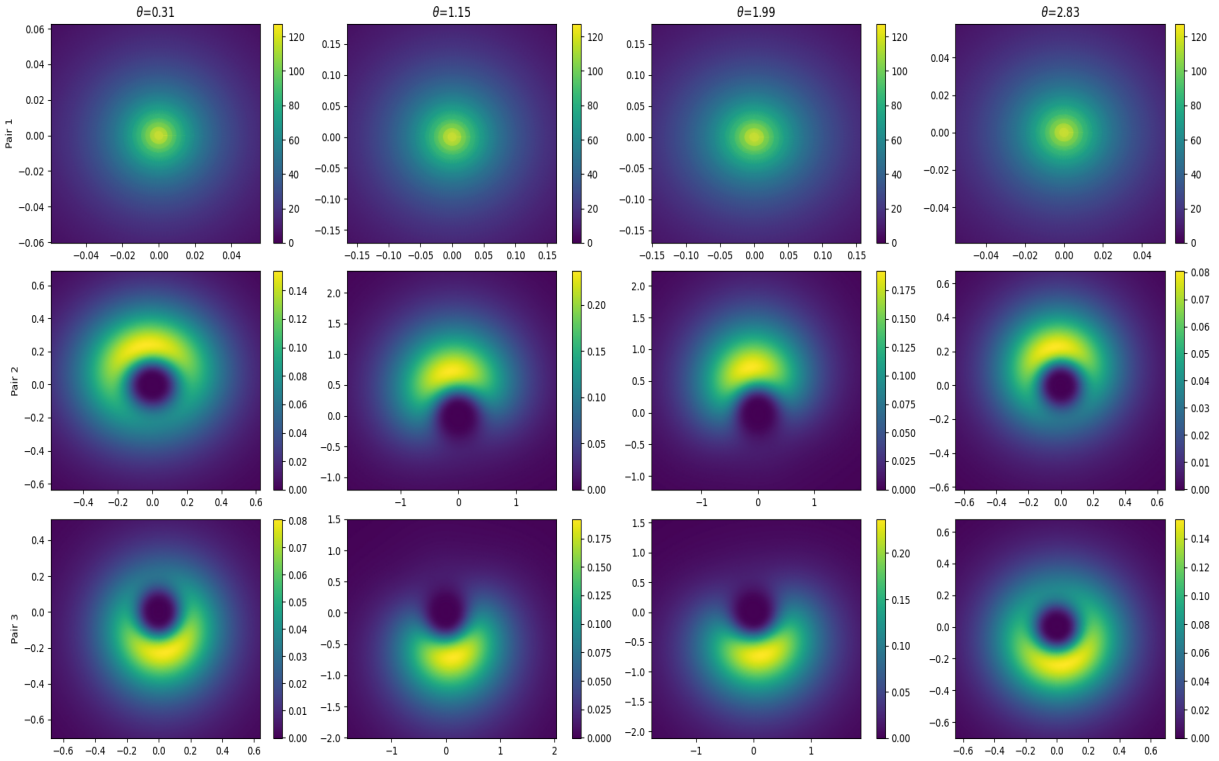

Figure 4.16: Carbon angular electron pair density contour plots for fixed values of θ. The axes correspond to the y and x Cartesian coordinates respectively, and the colour bar indicates the magnitude of the density.

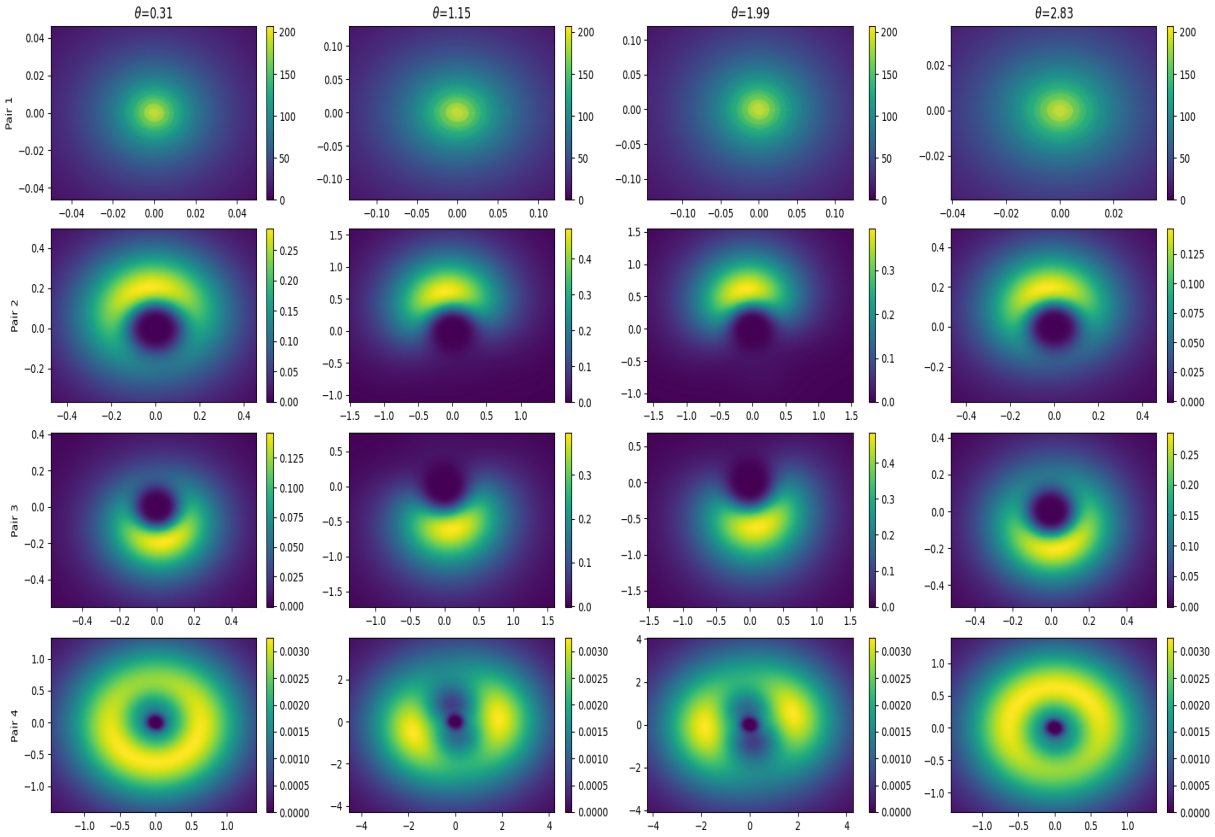

Figure 4.17: Nitrogen angular electron pair density contour plots for fixed values of θ. The axes correspond to the y and x Cartesian coordinates respectively, and the colour bar indicates the magnitude of the density.

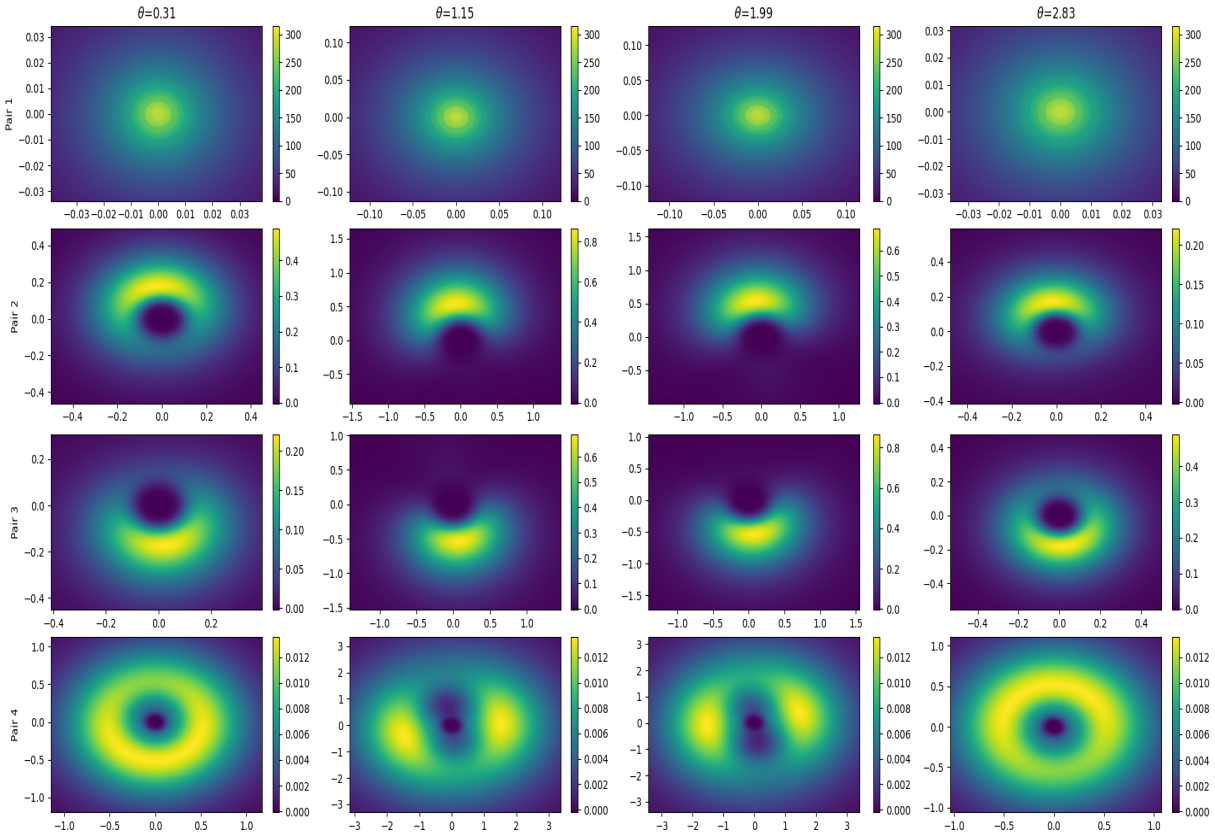

Figure 4.18: Oxygen angular electron pair density contour plots for fixed values of θ. The axes correspond to the y and x Cartesian coordinates respectively, and the colour bar indicates the magnitude of the density.

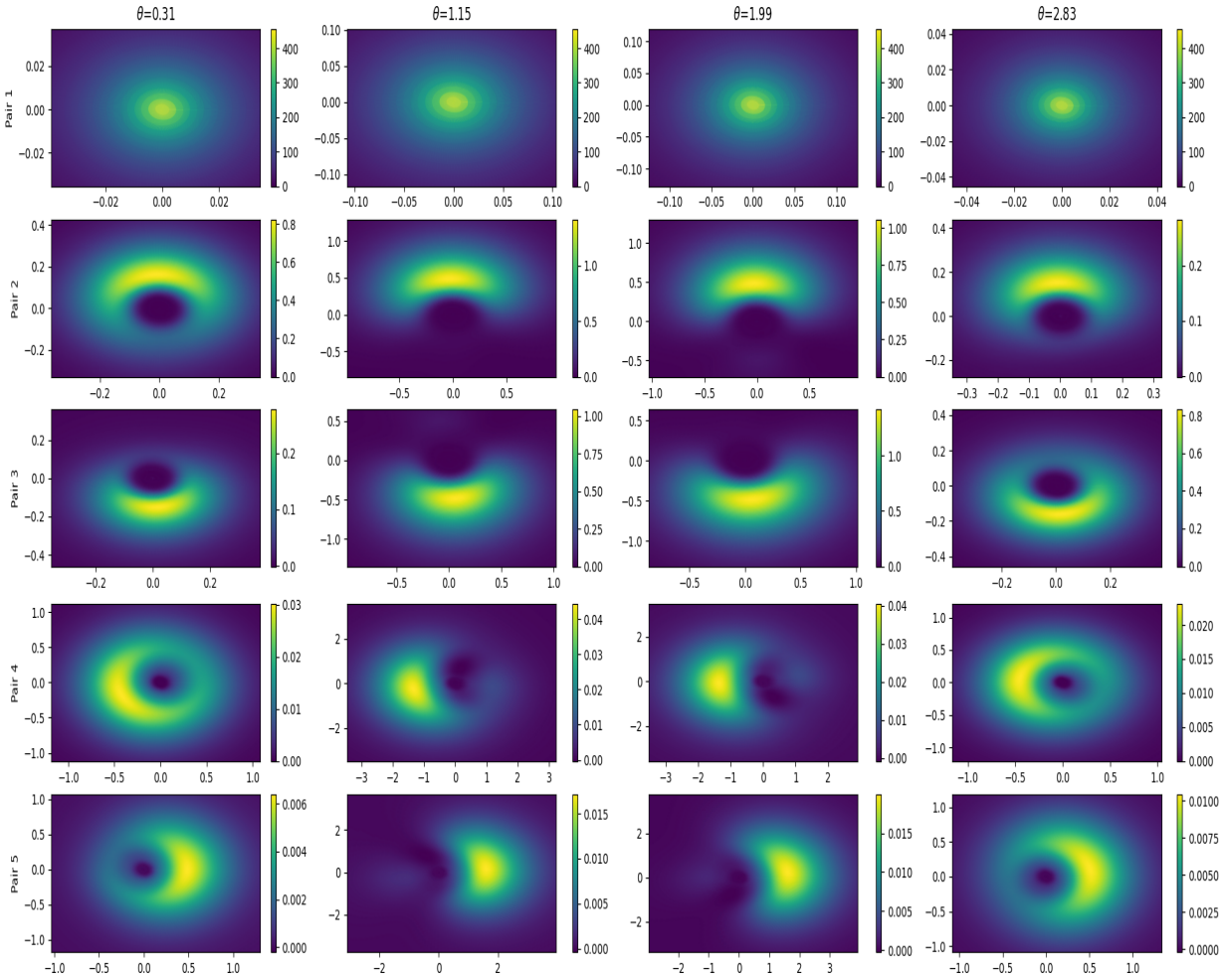

Figure 4.19: Fluorine angular electron pair density contour plots for fixed values of θ. The axes correspond to the y and x Cartesian coordinates respectively, and the colour bar indicates the magnitude of the density.

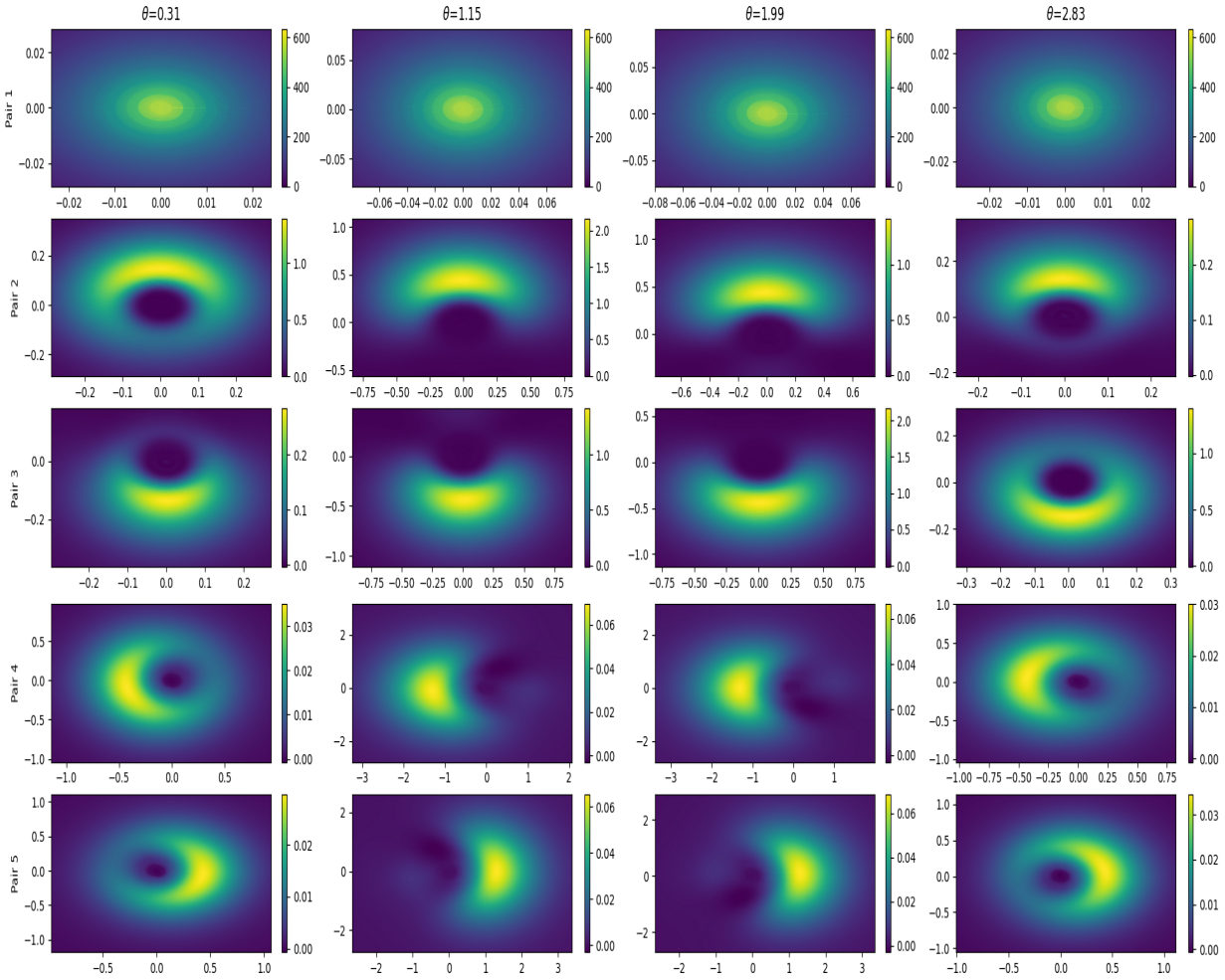

Figure 4.20: Neon angular electron pair density contour plots for fixed values of θ. The axes correspond to the y and x Cartesian coordinates respectively, and the colour bar indicates the magnitude of the density.

$$= -\sum_{ij} \left[q_\mu(s)\right]_{ij} \left(H_\mu^{\text{eff}} \phi_{\mu i}(\boldsymbol{r})\right) \phi_{\mu j}(\boldsymbol{r}') = -\sum_{ij} \left[q_\mu(s)\right]_{ij} \left[\varepsilon_\mu\right]_i \phi_{\mu i}(\boldsymbol{r}) \phi_{\mu j}(\boldsymbol{r}') \,. \tag{4.5}$$

Multiplying both sides with $\phi_{\mu k}(\boldsymbol{r})\phi_{\mu l}(\boldsymbol{r}')$, integrating over $\boldsymbol{r}$ and $\boldsymbol{r}'$, and using the orthogonality relation eqn. 4.3 then gives

$$\frac{\partial \left[q_\mu(s)\right]_{kl}}{\partial s} = -\left[q_\mu(s)\right]_{kl} \left[\varepsilon_\mu\right]_k \quad \rightarrow \quad \left[q_\mu(s)\right]_{kl} = \delta_{kl} e^{-\left[\varepsilon_\mu\right]_k s} \,, \tag{4.6}$$

so

$$q_\mu(\boldsymbol{r}, \boldsymbol{r}', s) = \sum_i e^{-\left[\varepsilon_\mu\right]_i s} \phi_{\mu i}(\boldsymbol{r}) \phi_{\mu i}(\boldsymbol{r}') \,. \tag{4.7}$$

The pair densities are then given by

$$n_\mu(\boldsymbol{r}, \beta) = \frac{N_\mu}{Q_\mu[w](\beta)} q_\mu(\boldsymbol{r}, \boldsymbol{r}, \beta) = \frac{N_\mu}{Q_\mu[w](\beta)} \sum_i e^{-\left[\varepsilon_\mu\right]_i s} |\phi_{\mu i}(\boldsymbol{r})|^2 \,. \tag{4.8}$$

Clearly eqn. 4.8 does not have 1-to-1 correspondence with the squared modulus of Kohn-Sham orbitals, therefore we should not necessarily expect the pair densities to reproduce the profiles of individual squared moduli of orbitals. In fact, the pair density profiles corresponding to non-spherical pairs vaguely resembles polymer macro-phase separation [52], where one pair occupies one of the lobes in one region and the other occupies the partner lobe across from it. Seeing as how the system is being modelled as a classical polymeric system, this behaviour is perhaps not unexpected (although certainly surprising to us initially). Those that are disturbed by the macro-phase-like behaviour of the pair densities can at least take comfort in the fact that the total densities of the atoms seen in figures 4.15-4.20 have approximately the same profiles as the densities predicted by quantum mechanics in the wavefunction picture.

Element	N_1	N_2	N_3	N_4	N_5	N
H	0.99985	-	-	-	-	0.99985
He	1.99967	-	-	-	-	1.99967
Li	1.99953	0.99975	-	-	-	2.99928
Be	1.99912	1.99970	-	-	-	3.99882
B	1.99824	1.99970	0.99974	-	-	4.99768
C	1.99663	1.99975	1.99975	-	-	5.99613
N	1.99398	1.99977	1.99977	0.99883	-	6.99236
O	1.98995	1.99979	1.99979	1.99951	-	7.98903

F	1.98421	1.99978	1.99978	1.99968	0.99988	8.98333
Ne	1.97641	1.99975	1.99975	1.99976	1.99976	9.97545

Table 4.6: Total and pair electron numbers for hydrogen to neon using full angular basis sets and populating the pairs according to their original definition. The dashes indicate null entries where the given element does not possess that specific pair number.

There are a number of constraints that the true electron density must satisfy in order to be considered physically acceptable, which we can use as benchmarks to assess the density profiles predicted by the model used in this work (figures 4.15-4.20), in light of the macro-phase results previously discussed. The two main constraints on the electron density are that it must be positive for all positions $\boldsymbol{r}$ and that its integral over all space must yield the electron number N (or the pair electron number if we are dealing with an individual pair density). Further constraints have been discovered over the course of the DFT research programme that have helped narrow down the search space of permissible densities that give the correct free energy. Two constraints in particular, are

$$1 \geq \frac{3\pi}{4K}\left[\frac{\pi}{2}\int \mathrm{d}\boldsymbol{r}\, n^3(\boldsymbol{r},\beta)\right]^{\frac{1}{3}} \quad \text{and} \quad 1 \geq \frac{1}{2K}\int \mathrm{d}\boldsymbol{r}\, \left(\nabla\sqrt{n(\boldsymbol{r},\beta)}\right)^2 , \tag{4.9}$$

where K represents the kinetic energy of the system [48], which is given by eqn. 3.72 in the model. The above constraints significantly reduce the size of the set of physically acceptable density distributions down to the intersection between the L^1 and L^3 function spaces [48]. Notice also that the right-hand side of the second inequality in eqns. 4.9 is the von Weizsacker kinetic energy functional, which is exact for one and two electron systems.

Element	Constraint 1	Constraint 2
H	0.85127	0.99985
He	0.87446	0.99983
Li	0.85268	0.95681
Be	0.83296	0.92839
B	0.82156	0.91465
C	0.80450	0.90473
N	0.79150	0.89245
O	0.78058	0.88252
F	0.77055	0.87353
Ne	0.76157	0.86472

Table 4.7: The values for the right-hand side of eqns. 4.9 for hydrogen to neon using full angular basis sets and populating the pairs according to their original definition.

The pair density profiles corresponding to figures 4.15-4.20 clearly demonstrate that the pair densities (and thus the total density) are non-negative for all positions $\boldsymbol{r}$, and the pair density integrals listed in table 4.6 show that the electron number constraint for each pair is mostly well satisfied. The accuracy of the values in table 4.6 is limited by the number of grid points used for the trapezoid rule numerical integration, for which larger numbers of grid points become very computationally expensive in three dimensions. The result of this is that the more sharply-peaked pair densities corresponding to the first couple pairs will decrease in accuracy as we go higher in atomic number if we do not increase the grid point density, which is why the accuracy increases with increasing pair number. Table 4.7 displays the right-hand side values of eqns. 4.9 for the elements hydrogen to neon, where we can clearly see that the density predicted by the model always satisfies these two inequalities. In particular, notice the right-hand side values of the second inequality in eqns. 4.9 for hydrogen and helium are almost exactly 1, which is the statement that the von Weizsacker kinetic energy functional is exact for one and two electron systems.

Despite the failure of the Pauli-exclusion field to satisfy the coordinate scaling relation eqn. 3.62, the above analysis demonstrates that the pair densities making up the total density satisfy all constraints necessary to guarantee a physically acceptable electron density. Together with the proof that pair densities do not necessarily correspond to individual squared moduli of orbitals, the macro-phase-like behaviour exhibited in figures 4.16-4.20 should then be taken seriously as a legitimate physical prediction of the model, and a detailed investigation in a future work could be undertaken to understand more about these structures.

4.4 Limitations

The Gaussian basis functions represent a major upgrade to the computational side of the present theory, providing the opportunity to explore more complicated atomic systems and also to realize the full angular density distribution. However, they are not without their own drawbacks. As was mentioned throughout chapter 3 and 4, the Gaussians are unfortunately a non-orthogonal basis set, which entails a number of modifications to the spectral equations from the previous work; including the addition of extra matrix multiplications from the overlap and Laplace matrices.

Even worse, linear dependence among basis elements can pop-up if the Gaussians do not suitably span the space, which means we cannot keep blindly adding more basis functions to increase the resolution and can have the completeness property nullified in the infinite basis set limit [68, 27]. What this effectively amounts to, is to introduce an auxiliary problem of generating appropriate exponents for the basis functions, one that adds a bit of arbitrariness to the computational implementation of the model.

The limitations introduced by the Gaussians are not that important in the context of a proof-of-concept proposal such as the present one, which is why no effort was expended in this work trying to remedy them. If one were motivated to tackle these issues, then switching to contracted Gaussian basis sets [27, 30, 26] would most likely be the solution, since they allow for many fewer basis functions to be used while still maintaining roughly the same level of precision and resolution; the price tag associated to the contracted sets comes in the form of additional minimization routines that either minimize the spectral representation of the free energy eqn. 3.70 with respect to even-tempered parameters [68, 27] or fit the Gaussians to a Slater-type function [26, 27]. Both of the previous methods typically require derivative information to perform the minimization, which is undesirable because the derivatives may not be well-defined or could possibly lead to numerical instabilities yielding false minima. A method that uses only the Nelder-Mead algorithm was originally developed for this work in anticipation of investigating molecular systems, which uses the spectral coefficients of the density and the Gaussian exponents from the uncontracted result to solve for the contraction coefficients, and then minimizes the sum of squared deviations between the two to solve for the exponents of the contracted set. Ultimately it was decided that investigating symmetry-breaking in atomic systems was more interesting and so the molecular direction was abandoned, but the algorithm remains for any future work.

The approximation to the Pauli-exclusion field is another issue that prevents the model from showing good agreement with the results from Hartree-Fock theory. Whether the exact expression for the Pauli-exclusion field will account for the binding energy discrepancies seen in tables 4.3 and 4.5 is one of the biggest open questions raised by this work. If the exact expression (to within numerical accuracy) does account for the deviations, then the idea of higher-dimensional excluded-volume being a classical manifestation of the Pauli-exclusion principle will have acquired strong evidence in favour of it. Otherwise, either the model will have to be modified by adding higher-order excluded-volume interactions or a new mechanism will have to be sought out. Further discussion of this point and other future work will be conducted in chapter 5.

Chapter 5

Conclusions and Future Work

The present alternative approach to OF-DFT based on ring polymer SCFT has been shown to faithfully reproduce quantitatively accurate atomic binding energies and electronic density profiles for isolated atomic systems based on the Hartree-Fock model. The agreement with the binding energies predicted by Hartree-Fock theory is within 10% for the first 86 elements, and within 3% for the first 34 elements. The comparison of electronic density profiles with Hartree-Fock theory made visible the overestimation of the Pauli-exclusion repulsion by the approximation in the form of larger than normal peak-to-peak separation, revealing some characteristics that the exact Pauli-exclusion field should have. The plots, especially helium and lithium, also provide some legitimacy for the novel electron self-interaction correction introduced in this work. The emergence of atomic shell structure from the postulated pair structure of the model and the spontaneous emergence of spherical symmetry-breaking are also predicted by the model. However, due to the approximation made on the Pauli-exclusion field, the predicted shell structure starts to deviate significantly past the element neon and the symmetry-breaking is first predicted to occur at carbon instead of boron. In accordance with reference [15], the symmetry-breaking effect is also found to have minimal impact on the binding energies, which suggests that the spherical-averaging approximation is physically reasonable when investigating bulk properties of atomic systems. The pair density contour plots also display behaviour similar to polymer macro-phase separation, but still produce the same total electronic density profile that is predicted by quantum mechanics.

The Gaussian basis sets are tested extensively and found to be more robust than previous iterations using eigenfunctions of the Laplacian. In particular, it is shown that Gaussians can achieve better resolution with significantly less numbers of basis functions, using suitably chosen basis

exponents, and do not suffer from finite-size effects. The Gaussians do however introduce an auxiliary problem of choosing the proper basis set exponents to span the space, which can prevent convergence to the infinite basis set limit. As well, the framework for general non-orthogonal basis sets within the model is derived in its entirety.

There are a number of interesting future directions one could take this research project in, now that the basic engine has been constructed. As was alluded to in section 4.4, one possible direction could be to extend the work of Sillaste and Thompson [72] in modelling systems of diatomic molecules to arbitrary formations of molecules or even solid-state lattices, since the present Gaussian infrastructure is easily adapted to any number of complex geometries. The work involved in this direction would include implementing the contracted sets discussed in section 4.4 and updating the computer program, generalizing the centres of the Gaussian basis sets to arbitrary positions, and modifying the structure of the computer program to accommodate multiple atoms. The shifting of the centres of the Gaussians from the origin to arbitrary positions is not so easily done with the spherical harmonic representation used in this work and is better facilitated using a Cartesian representation of the Gaussians [27], which only entails re-deriving the basis specific matrices and the spectral components of the electron-nucleus field. Fortunately, the expressions for these quantities have already been derived, although the expressions are much more complicated. In the case of solid-state lattices, pseudo-potentials and other modifications would need to be introduced as well [35, 84]. The rest of the work in this direction is merely a matter of getting the computational implementation right. Further increases in accuracy could also be achieved by combining the molecular dynamics framework of reference [10] with the model, to better account for the nuclear degrees of freedom.

Another possible direction mentioned in section 4.4 is to try and implement the exact Pauli-exclusion field, so that the comparison of the present model with Hartree-Fock theory can be completed, and the question of whether higher-dimensional excluded-volume is equivalent with the Pauli-exclusion principle can finally be settled. This direction is arguably the most important because it aims to test a foundational aspect of the theory that has implications on all other future work associated with the model. One possible consequence of answering the question posed in this paragraph would be modifying the Pauli-exclusion field to include higher-order excluded-volume interactions; this would be the case if the results didn't agree with Hartree-Fock theory after implementing the exact expression for the Pauli-exclusion field. The work involved with this direction is quite substantial, as the field now carries s-parameter dependence, meaning the diffusion equation eqn. 3.16 can no longer be solved as straightforwardly as it was in this work. In fact, the diffusion equation does not even admit a closed-form expression in the case that the field is s-dependent in general. This leaves two proposed possibilities to overcome this problem: 1) The solution to the diffusion equation is evaluated recursively using a Magnus expansion to

some specified order [8], or 2) the field is partitioned along the s parameter space and each value of the field in the partition is designated as a separate field, then a multi-block SCFT calculation is performed [54]. Out of the two proposed solutions, the second one is probably easier to implement, but it would require new derivations for most of the model equations.

Even more possible directions could be to include correlation terms and relativistic corrections to the atomic systems already considered here, or to elucidate the mechanism for electron spin in the model. Correlation fields are stipulated to be the only thing missing from this model that prevents it from completely agreeing with the predictions of non-relativistic quantum mechanics for neutral atoms not in the presence of any other fundamental fields. Therefore, finding a mechanism for correlations within the polymer picture would also be of foundational importance to the model. Not only that, but the picture painted by the model could reveal the nature of correlations in many-body systems, which would be of immense importance to the DFT community and the atomic physics community at large. The topic of quantum entanglement would also naturally be opened up in an investigation of correlations, and I would personally be curious to see what the mechanism is in the present model that gives rise to it. The introduction of quantum entanglement also connects nicely with information-theoretic approaches to DFT [59, 1], which could be useful in learning more about properties of correlations in many-body systems from the perspective of DFT. Investigating the mechanism that represents electron spin in the model would also be an interesting exercise to understand how spin would manifest itself in the polymer picture, and would nicely complement the investigation of correlations. Lastly, relativistic corrections including the fine structure [49, 3] and finite-size nuclear centres [81] could be added to the model and the heavier elements investigated, which may yield useful information on how relativistic effects manifest themselves in the polymer picture.

References

[1] M. Alipour. Making a happy match between orbital-free density-functional theory and information energy density. *Chem. Phys. Lett.*, 635:210–212, (2015).

[2] P. W. Atkins. *Atkins' Molecules*. Cambridge University Press, (2003).

[3] J. Autschbach. Perspective: Relativistic effects. *J. Chem. Phys.*, 136(15):150902, (2012).

[4] P. W. Ayers and M. Levy. Perspective on "density-functional approach to the frontier-electron theory of chemical reactivity". *Theoretical Chemistry Accounts*, 104:353–360, (2000).

[5] P. W. Ayers and M. Levy. Sum rules for exchange and correlation potentials. *J. Chem. Phys.*, 115(10):4438–4443, (2001).

[6] P. W. Ayers, R. C. Morrison, and R. G. Parr. Fermi-Amaldi model for exchange-correlation: Atomic excitation energies from orbital energy differences. *Mol. Phys.*, 103(15):2061–2072, (2005).

[7] E. G. Beltrametti and S. Bugajski. A classical extension of quantum mechanics. *J. Phys. A: Math. Gen.*, 28(12):3329–3343, (1995).

[8] S. Blanes, F. Casas, J. A. Oteo, and J. Ros. The Magnus expansion and some of its applications. *Phys. Rep.*, 470(5-6):151–238, (2009).

[9] S. F. Boys. Electronic wave functions I. a general method of calculation for the stationary states of any molecular system. *Proc. Roy. Soc.*, A200:542, (1950).

[10] R. Car and M. Parrinello. Unified approach for molecular dynamics and density-functional theory. *Phys. Rev. Lett.*, 55(22):2471, (1985).

[11] D. M. Ceperley. Path integrals in the theory of condensed helium. *Rev. Mod. Phys.*, 67:279–355, (1995).

[12] D. Chandler and P. G. Wolynes. Exploiting the isomorphism between quantum theory and classical statistical mechanics of polyatomic fluids. *J. Chem. Phys.*, 74(7):4078–4095, (1981).

[13] H. Chen and A. Zhou. Orbital-free density-functional theory for molecular structure calculations. *Numerical Mathematics: Theory, Methods and Applications*, 1(1):1–28, (2008).

[14] I. Cherkes, S. Klaiman, and N. Moiseyev. Spanning the Hilbert space with an even-tempered Gaussian basis set. *Int. J. Quantum Chem.*, 109(13):2996–3002, (2009).

[15] S. T. R. Chowdhury and J. P. Perdew. Spherical vs. non-spherical and symmetry-preserving vs. symmetry-breaking densities of open-shell atoms in density-functional theory. *J. Chem. Phys.*, 155(23):234110, (2021).

[16] A. Das. *Field Theory: A Path Integral Approach*. World Scientific, (1993).

[17] R. P. Feynman. Atomic theory of the λ transition in helium. *Phys. Rev.*, 91:1291–1301, (1953).

[18] R. P. Feynman, A. R. Hibbs, and D. F. Styer. *Quantum Mechanics and Path Integrals*. Dover Publications, (2010).

[19] G. H. Fredrickson, V. Ganesan, and F. Drolet. Field-theoretic computer simulation methods for polymers and complex fluids. *Macromolecules*, 35:16–39, (2002).

[20] Y. Jiang J. Li S. Li J. Ren G. Su, S. Yang and W. Liu. Modelling chemical reactions on surfaces: The roles of chemical bonding and van der Waals interactions. *Progress in Surface Science*, 94(4):100561, (2019).

[21] I. M. Gelfand, S. V. Fomin, and R. A. Silverman. *Calculus of Variations*. Prentice-Hall, (1963).

[22] B. Ghojogh, F. Karray, and M. Crowley. Eigenvalue and generalized eigenvalue problems: Tutorial, (2019).

[23] P. Gori-Giorgi and A. Savin. Study of the discontinuity of the exchange-correlation potential in an exactly soluble case. *Int. J. Quantum Chem.*, 109(11):2410–2415, (2009).

[24] R. Haag, N. M. Hugenholtz, and M. Winnink. On the equilibrium states in quantum statistical mechanics. *Commun. Math. Phys.*, 5(3):215–236, (1967).

[25] G. G. Hall. The molecular orbital theory of chemical valency VIII. a method of calculating ionization potentials. *Proc. R. Soc. Lond. A*, 205:541–552, (1951).

[26] W. J. Hehre, R. F. Stewart, and J. A. Pople. Self-consistent molecular-orbital methods I: Use of Gaussian expansions of Slater-type atomic orbitals. *J. Chem. Phys.*, 51(6):2657–2664, (1969).

[27] T. Helgaker and P. R. Taylor. *Gaussian Basis Sets and Molecular Integrals*, chapter 12, pages 725–856. (1995).

[28] P. Hohenberg and W. Kohn. Inhomogeneous electron gas. *Phys. Rev.*, 136:B864–B871, (1964).

[29] H. H. H. Homeier and E. O. Steinborn. Some properties of the coupling coefficients of real spherical harmonics and their relation to Gaunt coefficients. *J. Mol. Struct.*, 368:31–37, (1996). Proceedings of the Second Electronic Computational Chemistry Conference.

[30] S. Huzinaga, J. Andzelm, E. Radzio-Andzelm, Y. Sakai, H. Tatewaki, and M. Klobukowski. *Gaussian Basis Sets for Molecular Calculations*. Elsevier Science, (2012).

[31] Y. Yang J. U. Kim and W. B. Lee. Self-consistent field theory of Gaussian ring polymers. *Macromolecules*, 45(7):3263–3269, (2012).

[32] J. D. Jackson. *Classical Electrodynamics*. Wiley, (2012).

[33] R. O. Jones. Density-functional theory: Its origins, rise to prominence, and future. *Rev. Mod. Phys.*, 87:897–923, (2015).

[34] Y. Kalambet, Y. Kozmin, and A. Samokhin. Comparison of integration rules in the case of very narrow chromatographic peaks. *Chemometrics and Intelligent Laboratory Systems*, 179:22–30, (2018).

[35] V. V. Karasiev and S. B. Trickey. Issues and challenges in orbital-free density functional calculations. *Computer Physics Communications*, 183(12):2519–2527, (2012).

[36] M. Kardar. *Statistical Physics of Particles*. Cambridge University Press, (2007).

[37] T. Kato. On the eigenfunctions of many-particle systems in quantum mechanics. *Comm. Pure Appl. Math.*, 10:151–177, (1957).

[38] V. K. Khersonskii, A. N. Moskalev, and D. A. Varshalovich. *Quantum Theory Of Angular Momentum*. World Scientific Publishing Company, (1988).

[39] J. G. Kirkwood. Quantum statistics of almost classical assemblies. *Phys. Rev.*, 44:31–37, (1933).

[40] T. Koga and A. J. Thakker. Moments and expansion coefficients of atomic electron momentum densities: Numerical Hartree-Fock calculations for hydrogen to lawrencium. *J. Phys. B: At. Mol. Opt. Phys.*, 29:2973, (1996).

[41] W. Kohn and L. J. Sham. Self-consistent equations including exchange and correlation effects. *Phys. Rev.*, 140:A1133–A1138, (1965).

[42] E. Kreyszig. *Introductory Functional Analysis with Applications*. Wiley, (1991).

[43] W. Kutzelnigg. Theory of the expansion of wave functions in a Gaussian basis. *Int. J. Quantum Chem.*, 51(6):447–463, (1994).

[44] T. Lancaster and S. J. Blundell. *Quantum field theory for the gifted amateur*. Oxford University Press, (2014).

[45] J. E. Lennard-Jones. The electronic structure of some diatomic molecules. *Trans. Faraday Soc.*, 25:668–686, (1929).

[46] M. Levy. Universal variational functionals of electron densities, first-order density matrices, and natural spin-orbitals and solution of the *v*-representability problem. *Proc. Natl. Acad. Sci.*, 76(12):6062–6065, (1979).

[47] M. Levy and H. Ou-Yang. Exact properties of the Pauli potential for the square root of the electron density and the kinetic energy functional. *Phys. Rev. A*, 38:625–629, (1988).

[48] E. H. Lieb. Density functionals for Coulomb systems. In *Inequalities*, pages 269–303. Springer, (2002).

[49] W. Liu. Essentials of relativistic quantum chemistry. *J. Chem. Phys.*, 152(18):180901, (2020).

[50] J. P. Perdew M. Levy and V. Sahni. Exact differential equation for the density and ionization energy of a many-particle system. *Phys. Rev. A*, 30(5):2745–2748, (1984).

[51] M. W. Matsen. The standard Gaussian model for block copolymer melts. *J. Phys. Condens. Matter*, 14:R21–R47, (2002).

[52] M. W. Matsen. Self-consistent field theory and its applications. In *Soft Matter, Volume 1: Polymer Melts and Mixtures*, pages 3–83. Wiley-VCH, (2006).

[53] M. W. Matsen. Fast and accurate scft calculations for periodic block-copolymer morphologies using the spectral method with Anderson mixing. *Eur. Phys. J. E Soft Matter*, 30(4):361–369, (2009).

[54] M. W. Matsen and M. Schick. Stable and unstable phases of a diblock copolymer melt. *Phys. Rev. Lett.*, 72:2660–2663, (1994).

[55] D. A. McQuarrie. *Statistical Mechanics*. University Science Books, (2000).

[56] N. D. Mermin. Thermal properties of the inhomogeneous electron gas. *Phys. Rev.*, 137:A1441–A1443, (1965).

[57] A. Meurer, C. P. Smith, M. Paprocki, O. Čertík, S. B. Kirpichev, M. Rocklin, A. Kumar, S. Ivanov, J. K. Moore, S. Singh, T. Rathnayake, S. Vig, B. E. Granger, R. P. Muller, F. Bonazzi, H. Gupta, S. Vats, F. Johansson, F. Pedregosa, M. J. Curry, A. R. Terrel, Š. Roučka, A. Saboo, I. Fernando, S. Kulal, R. Cimrman, and A. Scopatz. SymPy: symbolic computing in Python. *PeerJ Computer Science*, 3:e103, (2017).

[58] R. S. Mulliken. Electronic structures of polyatomic molecules and valence VI. on the method of molecular orbitals. *J. Chem. Phys.*, 3(7):375–378, (1935).

[59] Á. Nagy. Fisher and Shannon information in orbital-free density-functional theory. *Int. J. Quantum Chem.*, 115(19):1392–1395, (2015).

[60] M. H. Cohen P. Elliott, K. Burke and A. Wasserman. Partition density functional theory. *Phys. Rev. A*, 82:024501, (2010).

[61] R. Parr and W. Yang. *Density-Functional Theory of Atoms and Molecules*. Oxford University Press, (1989).

[62] J. P. Perdew and A. Zunger. Self-interaction correction to density-functional approximations for many-electron systems. *Phys. Rev. B*, 23:5048–5079, (1981).

[63] D. Rohrlich and A. Budiyono. Quantum mechanics as classical statistical mechanics with an ontic extension and an epistemic restriction. *Nat. Commun.*, 8:1306, (2017).

[64] C. C. J. Roothaan. New developments in molecular orbital theory. *Rev. Mod. Phys.*, 23(2):69, (1951).

[65] P. Roy, S. Jang, and G. A. Voth. Feynman path centroid dynamics for Fermi–Dirac statistics. *J. Chem. Phys.*, 111(12):5303–5305, (1999).

[66] E. Runge and E. K. U. Gross. Density-functional theory for time-dependent systems. *Phys. Rev. Lett.*, 52(12):997, (1984).

[67] T. E. Markland S. Habershon, D. E. Manolopoulos and T. F. Miller III. Ring-polymer molecular dynamics: Quantum effects in chemical dynamics from classical trajectories in an extended phase space. *Annu. Rev. Phys. Chem.*, 64(1):387–413, (2013).

[68] M. W. Schmidt and K. Ruedenberg. Effective convergence to complete orbital bases and to the atomic Hartree–Fock limit through systematic sequences of Gaussian primitives. *J. Chem. Phys.*, 71(10):3951–3962, (1979).

[69] D. Sébilleau. On the computation of the integrated products of three spherical harmonics. *J. Phys. A Math. Gen.*, 31(34):7157–7168, (1998).

[70] R. Shankar. *Principles of Quantum Mechanics*. Springer US, (2012).

[71] R. A. Shaw. The completeness properties of Gaussian-type orbitals in quantum chemistry. *Int. J. Quantum Chem.*, 120(17):e26264, (2020).

[72] S. Sillaste and R. B. Thompson. Molecular bonding in an orbital-free-related density functional theory. *J. Phys. Chem. A*, 126:325–332, (2022).

[73] T. G. Strand and R. A. Bonham. Analytical expressions for the Hartree—Fock potential of neutral atoms and for the corresponding scattering factors for X-rays and electrons. *J. Chem. Phys.*, 40(6):1686–1691, (1964).

[74] A. Szabo and N. S. Ostlund. *Modern Quantum Chemistry: Introduction to Advanced Electronic Structure Theory*. Dover Publications, (2012).

[75] E. Teller. On the stability of molecules in the Thomas-Fermi theory. *Rev. Mod. Phys.*, 34:627–631, (1962).

[76] C. R. Harris *et al.* Array programming with NumPy. *Nature*, 585(7825):357–362, (2020).

[77] P. Virtanen *et al.* SciPy 1.0: Fundamental Algorithms for Scientific Computing in Python. *Nature Methods*, 17:261–272, (2020).

[78] R. B. Thompson. An alternative derivation of orbital-free density functional theory. *J. Chem. Phys.*, 150(20):204109, (2019).

[79] R. B. Thompson. Atomic shell structure from an orbital-free-related density- functional-theory Pauli potential. *Phys. Rev. A*, 102(1):1–10, (2020).

[80] R. B. Thompson, K. O. Rasmussen, and T. Lookman. Improved convergence in block copolymer self-consistent field theory by Anderson mixing. *J. Chem. Phys.*, 120(1):31–34, (2004).

[81] L. Visscher and K. G. Dyall. Dirac–fock atomic electronic structure calculations using different nuclear charge distributions. *Atomic Data and Nuclear Data Tables*, 67(2):207–224, (1997).

[82] U. von Barth and L. Hedin. A local exchange-correlation potential for the spin polarized case. *J. Phys. C: Solid State Phys.*, 5(13):1629, (1972).

[83] F. W. Wiegel. *Introduction to Path-integral Methods in Physics and Polymer Science*. World Scientific Publishing Company, (1986).

[84] W. C. Witt, B. G. del Rio, J. M. Dieterich, and E. A. Carter. Orbital-free density-functional theory for materials research. *J. Mater. Res.*, 33(7):777–795, (2018).

[85] J. Xia, C. Huang, I. Shin, and E. A. Carter. Can orbital-free density-functional theory simulate molecules? *J. Chem. Phys.*, 136(8):084102, (2012).

[86] T. Zeng and P. Roy. Microscopic molecular superfluid response: theory and simulations. *Rep. Prog. Phys.*, 77(4):046601, (2014).

APPENDICES

Appendix A

Basis Function-Specific Quantities

In the following derivations we consider single atomic systems centred at the origin of a spherical coordinate system with coordinates (r, θ, ϕ) where $\{0 \leq r, 0 \leq \theta \leq \pi, 0 \leq \phi < 2\pi\}$. For ease of notation, we will take Latin indices to represent the tuple of indices (p, l, m); indicating the basis function expansion coefficient, angular momentum number, and corresponding m values, respectively. Greek indices will represent the Pauli pairs.

As a reminder, the Gaussian basis functions used in this work are given by the expression

$$f_i(\boldsymbol{r}) = \mathcal{N}_{pl} Z_l^m(\theta, \phi) r^l e^{-c_{pl} r^2} ,$$

where $\mathcal{N}_{pl}$ are the components of the normalization matrix, c_{pl} are the Gaussian basis exponents, and $Z_l^m(\theta, \phi)$ are the real spherical harmonics. Before proceeding with the derivations, we will first define the real spherical harmonics and introduce a few important properties. The standard spherical harmonics are defined as

$$Y_l^m(\theta, \phi) = \sqrt{\frac{(2l+1)}{4\pi} \frac{(l-m)!}{(l+m)!}} P_l^m(\cos\theta) e^{im\phi} , \tag{A.1}$$

where $\{0 \leq l, -l \leq m \leq l\}$ and $P_l^m(\cos\theta)$ are the associated Legendre polynomials given by

$$P_l^m(\cos\theta) = \frac{(-1)^m}{2^l l!} \sin^m\theta \frac{\mathrm{d}^{l+m}}{\mathrm{d}(\cos\theta)^{l+m}} (\cos^2\theta - 1)^l . \tag{A.2}$$

The spherical harmonics arise as a solution to the angular part of Laplace's equation $\nabla^2 u(\boldsymbol{r}) = 0$ in spherical coordinates and form an orthonormal basis on the sphere S^2, meaning they satisfy

the relationship

$$\int \int \mathrm{d}\theta \, \mathrm{d}\phi \, Y_l^m(\theta, \phi) Y_{l'}^{m'}(\theta, \phi) = \delta_{mm'} \delta_{ll'} \, . \tag{A.3}$$

They also obey the parity relation $Y_l^m(\pi - \theta, \pi + \phi) = (-1)^l Y_l^m(\theta, \phi)$ and are related to their complex conjugate through the relation $Y_l^{m\,*}(\theta, \phi) = (-1)^m Y_l^{-m}(\theta, \phi)$. Now the real spherical harmonics are then defined in terms of the standard spherical harmonics by the piecewise expression

$$Z_l^m(\theta, \phi) = \begin{cases} \sqrt{2}\,\mathrm{Re}\left(Y_l^m(\theta, \phi)\right) & , \; m > 0 \\ Y_l^m(\theta, \phi) & , \; m = 0 \\ \sqrt{2}(-1)^{|m|}\,\mathrm{Im}\left(Y_l^{|m|}(\theta, \phi)\right) & , \; m < 0 \end{cases} \tag{A.4}$$

where $\mathrm{Re}(z)$ and $\mathrm{Im}(z)$ denote the real and imaginary parts of the argument z, respectively. The real spherical harmonics are clearly just linear combinations of the standard spherical harmonics that satisfy Laplace's equation, therefore they also satisfy it and preserve many of the same properties that the standard spherical harmonics possess (i.e. orthonormality, parity). One of the crucial differences lies in their image, which only includes the real numbers as opposed to the complex numbers for the standard spherical harmonics [29]. This will prove advantageous when it comes to numerical calculations and plotting of the density profiles, since the extra computer memory required to store complex numbers wont be needed and the basis set will already be defined in $\mathbb{R}^3$ as opposed to $\mathbb{R} \otimes \mathbb{C}$ [29]. The downside to using the real spherical harmonics comes from their piecewise definition, meaning some extra scaffolding will need to be introduced to compute the integral of the product of three real spherical harmonics that appears in the gamma tensor, which will be dealt with in subsection A.3.1.

A.1 Overlap Matrix

In order to compute the overlap integral eqn. 3.31, the coefficients of the normalization matrix $\mathcal{N}_{pl}$ for the Gaussian basis functions must first be computed, which means we must compute the integral:

$$S_{ij} = \mathcal{N}_{pl} \mathcal{N}_{p'l'} \int_0^{2\pi} \int_0^{\pi} \int_0^{\infty} f_{plm}(\boldsymbol{r}) f_{p'l'm'}(\boldsymbol{r}) r^2 \sin(\theta) \mathrm{d}r \mathrm{d}\theta \mathrm{d}\phi$$

$$= \mathcal{N}_{pl}\mathcal{N}_{p'l'} \int_0^{2\pi} \int_0^{\pi} Z_l^m(\theta,\phi) Z_{l'}^{m'}(\theta,\phi) \sin(\theta) \mathrm{d}\theta \mathrm{d}\phi \int_0^{\infty} r^{l+l'+2} e^{-(c_{pl}+c_{p'l'})r^2} \mathrm{d}r$$

$$= \mathcal{N}_{pl}\mathcal{N}_{p'l'}\delta_{ll'}\delta_{mm'} \frac{1}{2} \left(\frac{1}{c_{\mu il} + c_{\mu' jl'}} \right)^{\frac{1}{2}(l+l'+3)} \Gamma\left(\frac{l+l'+3}{2} \right)$$

$$= \mathcal{N}_{pl}^2 \frac{1}{2} (2c_{\mu il})^{-l-\frac{3}{2}} \Gamma\left(l+\frac{3}{2}\right) \quad (\text{when } p=p', l=l', m=m'), \tag{A.5}$$

so

$$\mathcal{N}_{pl} = \left(\frac{2(2c_{\mu il})^{l+\frac{3}{2}}}{\Gamma\left(l+\frac{3}{2}\right)} \right)^{\frac{1}{2}}. \tag{A.6}$$

The definition of the normalized Gaussian basis functions then becomes

$$f_{plm}(\boldsymbol{r}) = Z_l^m(\theta,\phi) \left(\frac{2(2c_{\mu il})^{l+\frac{3}{2}}}{\Gamma\left(l+\frac{3}{2}\right)} \right)^{\frac{1}{2}} r^l e^{-c_{pl}r^2}. \tag{A.7}$$

Now the overlap integral yields

$$S_{ij} = \left[\frac{2(2c_{p'l'})^{l'+\frac{3}{2}} 2(2c_{pl})^{l+\frac{3}{2}}}{\Gamma\left(l+\frac{3}{2}\right)\Gamma\left(l'+\frac{3}{2}\right)} \right]^{\frac{1}{2}} \left(\frac{1}{c_{pl}+c_{p'l'}} \right)^{\frac{1}{2}(l+l'+3)} \frac{\delta_{ll'}\delta_{mm'}}{2} \Gamma\left(\frac{l+l'+3}{2} \right) \tag{A.8}$$

$$= \left(\frac{2\sqrt{c_{pl}c_{p'l}}}{c_{pl}+c_{p'l}} \right)^{l+\frac{3}{2}} (\text{when } l=l' \text{ and } m=m'). \tag{A.9}$$

A.2 Laplace Matrix

Computing the components of the Laplace matrix (eqn. 3.32) in a Gaussian basis involves computing the Laplacian of a Gaussian, which we will first detail before performing the full computation.

A.2.1 Laplacian of the Gaussian Basis Functions

The Laplacian applied to $f_{plm}(\boldsymbol{r})$ yields

$$\boldsymbol{\nabla}^2 f_{plm}(\boldsymbol{r}) = \frac{1}{r^2}\frac{\partial}{\partial r}\left(r^2\frac{\partial f_{plm}(\boldsymbol{r})}{\partial r}\right) + \frac{1}{r^2\sin(\theta)}\frac{\partial}{\partial\theta}\left(\sin(\theta)\frac{\partial f_{plm}(\boldsymbol{r})}{\partial\theta}\right) + \frac{1}{r^2\sin^2(\theta)}\frac{\partial^2 f_{plm}(\boldsymbol{r})}{\partial\phi^2}$$

$$= \frac{Z_l^m(\theta,\phi)}{r^2}\frac{\partial}{\partial r}\left(r^2\frac{\partial g_{pl}(r)}{\partial r}\right) + \frac{g_{pl}(r)}{r^2\sin(\theta)}\frac{\partial}{\partial\theta}\left(\sin(\theta)\frac{\partial Z_l^m(\theta,\phi)}{\partial\theta}\right) + \frac{g_{pl}(r)}{r^2\sin^2(\theta)}\frac{\partial^2 Z_l^m(\theta,\phi)}{\partial\phi^2}\,.$$

The real spherical harmonics satisfy the angular part of Laplace's equation so

$$\frac{1}{r^2\sin(\theta)}\frac{\partial}{\partial\theta}\left(\sin(\theta)\frac{\partial Z_l^m(\theta,\phi)}{\partial\theta}\right) + \frac{1}{r^2\sin^2(\theta)}\frac{\partial^2 Z_l^m(\theta,\phi)}{\partial\phi^2} = -l(l+1)Z_l^m(\theta,\phi)$$

$$\rightarrow\quad \boldsymbol{\nabla}^2 f_{plm}(\boldsymbol{r}) = \frac{Z_l^m(\theta,\phi)}{r^2}\left[\frac{\partial}{\partial r}\left(r^2\frac{\partial g_{pl}(r)}{\partial r}\right) - g_{pl}(r)l(l+1)\right]$$

$$= \frac{Z_l^m(\theta,\phi)}{r^2}\left[4c_{pl}^2 r^4 g_{pl}(r) + g_{pl}(r)l(l+1) - 2c_{pl}(2l+3)g_{pl}(r) - g_{pl}(r)l(l+1)\right]$$

$$= 2c_{pl}f_{plm}(\boldsymbol{r})\left[2c_{pl}r^2 - (2l+3)\right]\,,$$

and after some simplification we get

$$\boldsymbol{\nabla}^2 f_{plm}(\boldsymbol{r}) = c_{pl}\left[4c_{pl}r^2 - (4l+6)\right]f_{plm}(\boldsymbol{r})\,, \tag{A.10}$$

which can be viewed as a generalized eigenvalue problem for the Laplacian and the operator $4c_{pl}r^2 - (4l+6)$, with generalized eigenvalues c_{pl}.

A.2.2 Components of the Laplace Matrix

The components of the Laplace matrix in a Gaussian basis are given by

$$L_{ij} = \int \mathrm{d}\boldsymbol{r}\, f_{p'l'm'}(\boldsymbol{r})\boldsymbol{\nabla}^2 f_{plm}(\boldsymbol{r}) = \int \mathrm{d}\boldsymbol{r}\, f_{p'l'm'}(\boldsymbol{r}) f_{plm}(\boldsymbol{r}) 2c_{il}\left(2c_{il}r^2 - 2l - 3\right)$$

$$= \mathcal{N}_{pl}\mathcal{N}_{p'l'}2c_{pl}\int_0^\pi\int_0^{2\pi}\mathrm{d}\theta\mathrm{d}\phi Z_{l'}^{m'}(\theta,\phi)Z_l^m(\theta,\phi)\int_0^\infty \mathrm{d}r\, r^{2+l+l'}\left(2c_{pl}r^2 - 2l - 3\right)e^{-(c_{pl}+c_{p'l'})r^2}$$

$$= \frac{2c_{pl}^2 \mathcal{N}_{pl}\mathcal{N}_{p'l'}\delta_{mm'}\delta_{ll'}}{(c_{pl}+c_{p'l'})^{\frac{1}{2}(l+l'+5)}}\Gamma\left(\frac{l+l'+5}{2}\right) - \frac{2c_{pl}(2l+3)\mathcal{N}_{pl}\mathcal{N}_{p'l'}\delta_{mm'}\delta_{ll'}}{2(c_{pl}+c_{p'l'})^{\frac{1}{2}(l+l'+3)}}\Gamma\left(\frac{l+l'+3}{2}\right)$$

$$= \frac{2c_{pl}}{c_{pl}+c_{p'l'}}\left[c_{pl}(l-l') - c_{p'l'}(2l+3)\right] S_{ji} \tag{A.11}$$

$$= -\frac{2c_{pl}c_{p'l}(2l+3)}{c_{pl}+c_{p'l}} S_{ji} \quad (\text{when } l = l^{'} \text{ and } m = m^{'}) \,. \tag{A.12}$$

A.3 Gamma Tensor

The components of the Gamma tensor (eqn. 3.33) in a Gaussian basis are given by

$$\Gamma_{ijk} = \int \mathrm{d}\boldsymbol{r} f_{plm}(\boldsymbol{r}) f_{p'l'm'}(\boldsymbol{r}) f_{p''l''m''}(\boldsymbol{r}) = \mathcal{N}_{pl}\mathcal{N}_{p'l'}\mathcal{N}_{p''l''}\int_0^{\pi}\int_0^{2\pi} \mathrm{d}\theta\mathrm{d}\phi Z_l^m(\theta,\phi)$$

$$\times Z_{l'}^{m^{'}}(\theta,\phi) Z_{l''}^{m^{''}}(\theta,\phi)\sin(\theta)\int_0^{\infty}\mathrm{d}r\, r^{l+l^{'}+l^{''}+2} e^{-(c_{pl}+c_{p'l'}+c_{p''l''})r^2}$$

$$= \alpha_{ll'l''}^{mm'm''}\mathcal{N}_{pl}\mathcal{N}_{p'l'}\mathcal{N}_{p''l''}\int_0^{\infty}\mathrm{d}r\, r^{l+l^{'}+l^{''}+2} e^{-(c_{pl}+c_{p'l'}+c_{p''l''})r^2}$$

$$= \frac{\alpha_{ll'l''}^{mm'm''}\mathcal{N}_{pl}\mathcal{N}_{p'l'}\mathcal{N}_{p''l''}}{2\left(c_{pl}+c_{p'l'}+c_{p''l''}\right)^{\frac{1}{2}(l+l'+l''+3)}}\Gamma\left(\frac{l+l^{'}+l^{''}+3}{2}\right), \tag{A.13}$$

where the symbol α represents the integral of three real spherical harmonics. The computation of α is quite involved, so the computation of its components is left to the following section.

A.3.1 Integral of Three Real Spherical Harmonics

The integral of three spherical harmonics was first worked out by Gaunt [38], but is expressed most concisely in terms of the Wigner $3-j$ symbols as

$$G_{l_1l_2l_3}^{m_1m_2m_3} \equiv \int\int \mathrm{d}\theta\,\mathrm{d}\phi\, Y_{l_1}^{m_1}(\theta,\phi) Y_{l_2}^{m_2}(\theta,\phi) Y_{l_3}^{m_3}(\theta,\phi)\sin\theta$$

$$= \sqrt{\frac{(2l_1+1)(2l_2+1)(2l_3+1)}{4\pi}} \begin{pmatrix} l_1 & l_2 & l_3 \\ 0 & 0 & 0 \end{pmatrix} \begin{pmatrix} l_1 & l_2 & l_3 \\ m_1 & m_2 & m_3 \end{pmatrix} . \tag{A.14}$$

The Wigner $3-j$ symbols arise naturally when adding angular momentum values in a multi-electron system, possessing the angular momentum selection rules from atomic and molecular physics as part of their mathematical structure. For reference, the selection rules are $-l_i \leq m_i \leq l_i$, $m_1 + m_2 + m_3 = 0$, $l_1 + l_2 + l_3$ even, and $|l_1 - l_2| \leq l_3 \leq l_1 + l_2$ [38]. The $3-j$ symbols have many known symmetries and recurrence relations but we will not state them here as they are not relevant for this section, however, reference [38] contains the details for those interested.

The usual approach to calculating the Gaunt coefficients relies on using the recurrence relations of the Wigner $3-j$ symbols to compute them recursively, which is what has been done in this work. The algorithm that is used is called the Schulten-Gordon-Cruzan algorithm [69] and it relies on the recurrence relation

$$\begin{pmatrix} l_1 & l_2 & l_3-1 \\ m_1 & m_2 & m_3 \end{pmatrix} = -\frac{l_3 A(l_3+1)}{(l_3+1)A(l_3)} \begin{pmatrix} l_1 & l_2 & l_3+1 \\ m_1 & m_2 & m_3 \end{pmatrix} - \frac{B(l_3)}{(l_3+1)A(l_3)} \begin{pmatrix} l_1 & l_2 & l_3 \\ m_1 & m_2 & m_3 \end{pmatrix} , \tag{A.15}$$

where

$$A(l_3) = \sqrt{l_3^2 - (l_1-l_2)^2}\sqrt{(l_1+l_2+1)^2 - l_3^2}\sqrt{l_3^2 - m_3^2}$$

$$B(l_3) = -(2l_3+1)[l_1(l_1+1)m_3 - l_2(l_2+1)m_3 - l_3(l_3+1)(m_2-m_1)] . \tag{A.16}$$

When $m_1 = m_2 = m_3 = 0$, the $3-j$ symbols are only non-zero for even $l_1+l_2+l_3$ (third selection rule) and $B(l_3) = 0$, so the second term on the right hand side of eqn. A.15 vanishes and we shift l_3 down by 1 to arrive at the expression

$$\begin{pmatrix} l_1 & l_2 & l_3-2 \\ 0 & 0 & 0 \end{pmatrix} = \frac{K(l_3)}{K(l_3-1)} \begin{pmatrix} l_1 & l_2 & l_3 \\ 0 & 0 & 0 \end{pmatrix} , \tag{A.17}$$

where

$$K(l_3) = \sqrt{l_3^2 - (l_1-l_2)^2}\sqrt{(l_1+l_2+1)^2 - l_3^2} . \tag{A.18}$$

The algorithm then works as follows. A particular l_3 value is chosen and the recurrences eqn. A.15 and eqn. A.17 work their way downward starting at $l_3 = l_1 + l_2$, which has a known form given by

$$\begin{pmatrix} l_1 & l_2 & l_1+l_2 \\ m_1 & m_2 & m_3 \end{pmatrix} = (-1)^{l_1-l_2-m_3} \times$$

$$\times \sqrt{\frac{(2l_1)!(2l_2)!(l_1+l_2+m_3)!(l_1+l_2-m_3)!}{(2l_1+2l_2+1)!(l_1+m_1)!(l_1-m_1)!(l_2+m_2)!(l_2-m_2)!}}, \tag{A.19}$$

until they reach the given l_3.

Now that the computation of the Gaunt coefficients has been illustrated, it must be adapted for the real spherical harmonics. A brute force approach would be to calculate all $3^3 = 27$ separate cases, which is mentally draining and is easily error-prone. A more elegant method, using ideas from [29], expresses the real spherical harmonics as the unitary transformation of the standard spherical harmonics

$$Z_l^m(\theta,\phi) = \sum_{m'} U_{m'}^m Y_l^{m'}(\theta,\phi)\,; \tag{A.20}$$

then using the property that $Z_l^{m\,*}(\theta,\phi) = Z_l^m(\theta,\phi)$, the following condition on the unitary matrix elements must hold $U_{m'}^{m\,*} = (-1)^{m'} U_{-m'}^m$, from which reference [29] derives the unitary matrix elements to be

$$U_{m'}^m = \delta_{m0}\delta_{m'0} + \frac{1}{\sqrt{2}}\left(\Theta(m)\delta_{mm'} + i\Theta(-m)(-1)^{m'}\delta_{mm'} - i\Theta(-m)\delta_{-mm'} + \Theta(m)(-1)^{m'}\delta_{-mm'}\right), \tag{A.21}$$

where $\Theta(x)$ is the Heaviside step function. The Gaunt coefficients for the real spherical harmonics are then expressed as

$$\alpha_{ll'l''}^{mm'm''} = \sum_{m_1 m_2 m_3} U_{m_1}^m U_{m_2}^{m'} U_{m_3}^{m''} G_{ll'l''}^{m_1 m_2 m_3}\,. \tag{A.22}$$

The full algorithm to compute the Gaunt coefficients for the real spherical harmonics then consists of first finding the standard Gaunt coefficients using the Schulten-Gordon-Cruzan algorithm, then computing the unitary matrix U, and finally computing the matrix product eqn. A.22.

Appendix B

Path Integral Solution to the Modified Diffusion Equation

The path integral eqn. 3.15 was used to great utility in the derivation of the SCFT equations, providing analytic expressions for the propagators and allowing for a more intuitive understanding of the physics, but deriving the expression for the path integral was taken for granted. A derivation of the path integral for the single-particle propagator eqn. 3.15 will be presented here to close that gap, and this will hopefully be sufficient to understand how the expression for the N-body propagator comes about. This section follows the presentation in Shankar [70], but Feynman and Hibbs [18] can also be consulted for more information.

Starting from the diffusion equation

$$\frac{\partial q(\boldsymbol{r}, \boldsymbol{r}', s)}{\partial s} = -H_{\text{eff}} q(\boldsymbol{r}, \boldsymbol{r}', s) = \frac{\hbar^2}{2m} \nabla^2 q(\boldsymbol{r}, \boldsymbol{r}', s) - W(\boldsymbol{r}) q(\boldsymbol{r}, \boldsymbol{r}', s) \,, \tag{B.1}$$

we notice that the Hamiltonian H_{eff} is s-independent and we can therefore obtain a solution to eqn. B.1 as

$$q(\boldsymbol{r}, \boldsymbol{r}', s) = e^{-\int_0^s \mathrm{d}t H_{\text{eff}}} q(\boldsymbol{r}, \boldsymbol{r}', 0) = e^{-sH_{\text{eff}}} q(\boldsymbol{r}, \boldsymbol{r}', 0) \,. \tag{B.2}$$

The above solution is not very useful because the expression contains the exponential of an operator, which is highly non-trivial to evaluate. Instead, let us express eqn. B.2 in the position basis as

$$q(\boldsymbol{r}, \boldsymbol{r}', s) = \langle \boldsymbol{r} | e^{-sH_{\text{eff}}} | \boldsymbol{r}' \rangle = \langle \boldsymbol{r} | e^{-s(T+W)} | \boldsymbol{r}' \rangle \,, \tag{B.3}$$

where T is the kinetic energy operator and W is the single-particle potential operator. Now introduce the discretization $s = \varepsilon n$ and consider the limit as $\varepsilon \to 0$ and $n \to \infty$. Using the Lie product formula

$$e^{A+B} = \lim_{n\to\infty} (e^{A/n} e^{B/n})^n \tag{B.4}$$

for arbitrary $m \times m$ matrices A and B, eqn. B.3 can clearly be rewritten as

$$\begin{aligned} q(\boldsymbol{r}, \boldsymbol{r}', s) &= \lim_{\varepsilon\to 0} \langle \boldsymbol{r}| e^{-s(T+W)} |\boldsymbol{r}'\rangle = \lim_{\varepsilon\to 0} \lim_{n\to\infty} \langle \boldsymbol{r}| \left[e^{-\frac{s}{n}T} e^{-\frac{s}{n}W} \right]^n |\boldsymbol{r}'\rangle \\ &= \lim_{\varepsilon\to 0} \lim_{n\to\infty} \langle \boldsymbol{r}| \left[e^{-\varepsilon T} e^{-\varepsilon W} \right]^n |\boldsymbol{r}'\rangle = \lim_{\varepsilon\to 0} \lim_{n\to\infty} \langle \boldsymbol{r}| \underbrace{e^{-\varepsilon T} e^{-\varepsilon W} e^{-\varepsilon T} e^{-\varepsilon W} \cdots}_{\text{n times}} |\boldsymbol{r}'\rangle \,. \end{aligned} \tag{B.5}$$

If we introduce $n-1$ copies of the resolution of the identity eqn. 3.2 and insert each one between each $e^{-\varepsilon T} e^{-\varepsilon W}$ of eqn. B.5, then we get

$$\begin{aligned} q(\boldsymbol{r}, \boldsymbol{r}', s) = \lim_{\varepsilon\to 0} \lim_{n\to\infty} \int \mathrm{d}\boldsymbol{r}_1 \cdots \int \mathrm{d}\boldsymbol{r}_{n-1} \int \mathrm{d}\boldsymbol{r}_n \langle \boldsymbol{r}| e^{-\varepsilon T} e^{-\varepsilon W} |\boldsymbol{r}_n\rangle \langle \boldsymbol{r}_n| e^{-\varepsilon T} e^{-\varepsilon W} |\boldsymbol{r}_{n-1}\rangle \langle \boldsymbol{r}_{n-1}| \\ \times \cdots |\boldsymbol{r}_1\rangle \langle \boldsymbol{r}_1| e^{-\varepsilon T} e^{-\varepsilon W} |\boldsymbol{r}'\rangle \,. \end{aligned} \tag{B.6}$$

Since W is just a function of the position operator, the action of $e^{-\varepsilon W}$ on an individual position ket will simply replace its argument with a position $\boldsymbol{r}_i$, so the nth expectation value in eqn. B.6 will evaluate to

$$\langle \boldsymbol{r}_n| e^{-\varepsilon T} e^{-\varepsilon W} |\boldsymbol{r}_{n-1}\rangle = \langle \boldsymbol{r}_n| e^{-\varepsilon T} |\boldsymbol{r}_{n-1}\rangle e^{-\varepsilon W(\boldsymbol{r}_{n-1})} \,. \tag{B.7}$$

The expectation value left over in eqn. B.7 can be solved for by inserting the resolution of the identity operator in the momentum basis $I = \int \frac{\mathrm{d}\boldsymbol{p}}{2\pi\hbar} |\boldsymbol{p}\rangle\langle\boldsymbol{p}|$ and substituting the inner product $\langle \boldsymbol{r}|\boldsymbol{p}\rangle = \exp\left(\frac{i}{\hbar}\boldsymbol{p}\cdot\boldsymbol{r}\right)$:

$$\begin{aligned} \langle \boldsymbol{r}_n| e^{-\varepsilon T} |\boldsymbol{r}_{n-1}\rangle &= \frac{1}{2\pi\hbar} \int \mathrm{d}\boldsymbol{p}\, \langle \boldsymbol{r}_n| e^{-\varepsilon \frac{P^2}{2m}} |\boldsymbol{p}\rangle \langle \boldsymbol{p}|\boldsymbol{r}_{n-1}\rangle = \frac{1}{2\pi\hbar} \int \mathrm{d}\boldsymbol{p}\, \langle \boldsymbol{r}_n| \underbrace{e^{-\varepsilon \frac{P^2}{2m}} |\boldsymbol{p}\rangle}_{|\boldsymbol{p}\rangle e^{-\varepsilon \frac{\boldsymbol{p}^2}{2m}}} e^{\frac{i}{\hbar}\boldsymbol{p}\cdot\boldsymbol{r}_{n-1}} \\ &= \frac{1}{2\pi\hbar} \int \mathrm{d}\boldsymbol{p}\, e^{-\frac{i}{\hbar}\boldsymbol{p}\cdot\boldsymbol{r}_n} e^{-\varepsilon\frac{\boldsymbol{p}^2}{2m}} e^{\frac{i}{\hbar}\boldsymbol{p}\cdot\boldsymbol{r}_{n-1}} = \frac{1}{2\pi\hbar} \int \mathrm{d}\boldsymbol{p}\, e^{-\varepsilon\frac{\boldsymbol{p}^2}{2m} + \frac{i}{\hbar}\boldsymbol{p}\cdot(\boldsymbol{r}_{n-1}-\boldsymbol{r}_n)} \\ &= \frac{1}{2\pi\hbar} e^{-\frac{m}{2\varepsilon\hbar^2}(\boldsymbol{r}_n-\boldsymbol{r}_{n-1})^2} \int \mathrm{d}\boldsymbol{p}\, e^{-\left(\sqrt{\frac{\varepsilon}{2m}}\boldsymbol{p} + i\sqrt{\frac{m}{2\varepsilon\hbar^2}}(\boldsymbol{r}_n-\boldsymbol{r}_{n-1})\right)^2} \end{aligned}$$

$$= \left[\frac{m}{2\pi\varepsilon\hbar^2}\right]^{\frac{1}{2}} e^{-\frac{m(\boldsymbol{r}_n-\boldsymbol{r}_{n-1})^2}{2\hbar^2\varepsilon}} . \tag{B.8}$$

after making the substitution $u = \sqrt{\frac{\varepsilon}{2m}}\boldsymbol{p} + i\sqrt{\frac{m}{2\varepsilon\hbar^2}}(\boldsymbol{r}_n - \boldsymbol{r}_{n-1}), \mathrm{d}u = \mathrm{d}\boldsymbol{p}\sqrt{\frac{\varepsilon}{2m}}$. Equation B.7 then becomes

$$\langle \boldsymbol{r}_n | e^{-\varepsilon T} e^{-\varepsilon W} | \boldsymbol{r}_{n-1} \rangle = \left[\frac{m}{2\pi\varepsilon\hbar^2}\right]^{\frac{1}{2}} e^{-\frac{m(\boldsymbol{r}_n-\boldsymbol{r}_{n-1})^2}{2\hbar^2\varepsilon} - \varepsilon W(\boldsymbol{r}_{n-1})} , \tag{B.9}$$

and after substituting eqn. B.9 into eqn. B.6 for each expectation value we arrive at the expression

$$q(\boldsymbol{r}, \boldsymbol{r}', s) = \lim_{\varepsilon\to 0} \lim_{n\to\infty} \left[\frac{m}{2\pi\varepsilon\hbar^2}\right]^{\frac{n}{2}} \prod_i^n \int \mathrm{d}\boldsymbol{r}_i e^{-\sum_j^n \left(\frac{m(\boldsymbol{r}_j-\boldsymbol{r}_{j-1})^2}{2\hbar^2\varepsilon} + \varepsilon W(\boldsymbol{r}_j)\right)} , \tag{B.10}$$

which becomes eqn. 3.15

$$q(\boldsymbol{r}, \boldsymbol{r}', s) = \mathcal{A} \int_{\boldsymbol{r}'}^{\boldsymbol{r}} \mathcal{D}[\boldsymbol{r}(\tau)] e^{-\int_0^s \mathrm{d}\tau \left[\frac{m}{2\hbar^2}\left|\frac{\mathrm{d}\boldsymbol{r}(\tau)}{\mathrm{d}\tau}\right|^2 + W(\boldsymbol{r}(\tau))\right]} \tag{B.11}$$

upon evaluation of the limits.